ARL 65-59

# INITIAL STUDIES OF CONDENSING METAL VAPORS CARRIED BY EXPANDING INERT GASES

KENNETH R. SIVIER
PAI-LIEN LU
DONALD D. McBRIDE
EROL OKTAY

JNIVERSITY OF MICHIGAN
ANN ARBOR, MICHIGAN

MARCH 1965

Contract AF 33(657)-8867
Project 7116
Task 7116-01

AEROSPACE RESEARCH LABORATORIES
OFFICE OF AEROSPACE RESEARCH
UNITED STATES AIR FORCE
WRIGHT-PATTERSON AIR FORCE BASE, OHIO

## FOREWORD

This is the final report on Contract AF 33(657)-8867, entitled "Research Study of Condensation Phenomena Related to Vapors in Expanding Gases", between the Aerospace Research Laboratories, Office of Aerospace Research, United States Air Force, and The University of Michigan. This contract covered the two year period from 1 June 1962 through 31 May 1964. The objective of the contract was to study condensation phenomena, that occur in expanding gases, with special emphasis on condensable metal vapors flowing with inert carrier gases. The research was accomplished on Task 7116-01, "Internal Flow Research," of Project 7116, "Energy Conversion Research," under the technical cognizance of Everett D. Stephens of the Thermo-Mechanics Research Laboratory of the Aerospace Research Laboratories.

The project was under the direction of Professor P. M. Sherman, Aeronautical and Astronautical Engineering Department of The University of Michigan, as principal investigator and, during the contract year from 1 June 1963 through 31 May 1964, K. R. Sivier as co-principal investigator. Professor Sherman was on academic leave during the 1964 calendar year; therefore, this report has been prepared under the direction of Mr. Sivier. Since much of the work is still "in progress", a major portion of this report deals with this progress, without a statement of final results.

The technical sections of the report were prepared by the following persons:

| | |
|---|---|
| P. L. Lu | Secs 2. 4 and 4, Appendices A, F, and G |
| E. Oktay | Appendices D and H |
| D. McBride | Secs. 2. 1, 2. 2, 2. 3, and 3. 2 |
| K. R. Sivier | Secs. 1. and 3. 1, Appendices B and C |

The authors wish to thank Mr. Stanley Goddard for his assistance during the initial phases of the photomicrography and underexpanded jet studies and for his preparation of Appendix E.

## ABSTRACT

A report is presented on the progress of an experimental investigation of the condensation of metal vapors carried by an expanding inert gas initially at high pressure. This investigation has emphasized some initial experiments in The University of Michigan's Hotshot Wind Tunnel and a study of instrumentation techniques.

Three zinc-in-helium tests in the Hotshot tunnel have indicated that the metallic condensate occurs in the form of very small particles; most particles were found to have diameters of from 0.01 to 0.1 microns. These particles were collected on impact probes from the hypersonic nozzle flow and analysed by electronmicroscopy. A spectrographic analysis of the particle samples showed that roughly one percent by mass of contaminants (principally copper, iron, and silicon) were added to the zinc in the hotshot arc chamber.

In addition to direct particle sampling, the techniques of light scattering and photomicrography (direct photography of the condensed particles) have been investigated. The study of light scattering has progressed to a bench set-up for evaluation and calibration of a system that measures light attenuation by the scattering medium. Although indicating the possibility of the photography of one micron diameter particles traveling at high speed, the study of the photomicrography technique has been discontinued in view of the very small particle sizes indicated by the direct samples from the zinc-in-helium tests.

TABLE OF CONTENTS

## LIST OF ILLUSTRATIONS

LIST OF ILLUSTRATIONS continued.

LIST OF ILLUSTRATIONS continued.

Figure

Figure

# 1. INTRODUCTION

Condensation in rapidly expanding flows was observed in the last century in the fogs that occur in steam nozzles. The dynamics of the condensation phenomena were indicated by the shift of the condensation line (Wilson line) away from the saturation line in the direction of adiabatic supersaturation (i. e., expansion along an isentrope to a temperature below that of equilibrium saturation). Stodola's discussion (Ref. 1), of condensation in steam nozzles, stands as one of the earliest definitive treatments of condensation phenomena.

During the second quarter of the present century, the effects of the condensation of water vapor in supersonic wind tunnels and of air (or nitrogen) in hypersonic wind tunnels have been observed and have been studied widely. These condensation effects are of significant practical importance since they establish the air dryer requirements for supersonic wind tunnels and the minimum heater requirements for hypersonic wind tunnels. Although condensation dynamics (leading again to supersaturated flows) remain important in the wind tunnel problem, the influence of "contaminants", that provide nuclei for the condensation process, becomes significant (e. g., Ref. 2) and may completely overshadow the homogeneous condensation process. Stever (Ref. 3) and Wegener and Mack (Ref. 4) present contemporary reviews of the work that has been done in the field of condensation in wind tunnel flows. Daum's recent paper (Ref. 5) is evidence that interest, in the problems of condensation in wind tunnel flows, still exists.

More recently, the effect of condensation phenomena, on the performance of advanced power plants, has become of interest. For example, condensation produces important effects (e. g., turbine efficiency, blade erosion, etc.) on the

The manuscript was released originally by the authors in September 1964 for publication as an ARL Technical Documentary Report. The revised manuscript was released for publication in February 1965.

performance of turbines using metal vapors as the working fluid. In the case of rocket motors that burn fuels with metallic additives, the combustion rate can be influenced by the rate at which the metallic oxides can be condensed out of the products of combustion. Also, the energy released during condensation of combustion products represents one factor influencing the thrust performance of a rocket system. Finally, the condensation process is fundamental to the operation of the colloidal EHD energy converter (Ref. 6) and has applications to the generation of colloidal particles for the electrostatic engine, Ref. 7.

It is evident, therefore, that both the scope and importance of condensation phenomena are growing. The work, covered by this report, was directed toward a part of the field of condensation phenomena about which very little is known; i. e., the condensation of metal vapors that are initially at very high temperatures and pressures and that are being carried through an expansion process by inert gases. The experimental investigation of such phenomena involves two fundamental problems: (1) the design of an experiment suitable for producing the metal vapor/inert carrier mixture and expanding this mixture in such a way that condensation is achieved; and (2) the development and application of instrumentation techniques which permit the extraction of meaningful information from the experiment. This project has been concerned mainly with these two problems. The progress in solving these problems is the principal subject of this report.

## 2. METAL VAPOR CONDENSATION EXPERIMENTS

The metal vapor condensation experiments were conducted in the University of Michigan's Hotshot Wind Tunnel facility. This facility operates at the high temperatures and pressures necessary for metal condensation experiments. In addition the arcing process, that is normally used to energize the facility's working fluid, was available for producing the metal vapor for the experiment.

The experiments reported below were essentially feasibility studies. The primary objective was an evaluation of the effectiveness of the hotshot (and the problems associated with its use) in performing the metal condensation experiments. In addition, the experiments permitted an initial study of the techniques required to obtain samples of the condensate from the expanding flow. To increase the effectiveness of these preliminary studies, the following requirements for the experiments were established:

1. Moderate arc chamber pressures and temperatures to minimize the hotshot operation problems.
2. Use of the test metal for part of the arc chamber electrode assembly to simplify the vaporization problem. This requires that the test metal have certain structual properties and be convenient to handle and machine.
3. The test metal should have a sufficiently high vapor pressure, so that a substantial amount vaporizes at the moderate arc chamber temperatures, and a low surface tension, so that homogeneous condensation occurs more readily.
4. A chemically inert carrier gas.

The vapor pressure curves for several metals are presented in Fig. 1. Zinc appears to best satisfy the requirement of a high vapor pressure while having reasonable handling properties and structural strength. In addition, zinc has a moderate value of surface tension; i. e., about 700 dynes/cm compared to about 1100 for copper and 450 for lead.

Helium was selected as the carrier gas mainly because of its chemical inertness. In addition, when comparing helium with argon, the metal-helium mixture results in a larger mass fraction of metal vapor, for a fixed mass of vaporized metal.

## 2.1 THE HOTSHOT WIND TUNNEL

The Hotshot Wind Tunnel (see Fig. 2 and Ref. 9) is an impulse-type, blowdown wind tunnel utilizing energy that is first stored as rotational kinetic energy in a heavy flywheel. This energy is transferred first, by means of a unipolar generator, to the magnetic field of a large coil, and finally, by means of an arc discharge, to the gas in the arc chamber, Fig. 3. The resulting constant volume energy addition causes the pressure and temperature of the gas to rise until a diaphragm, just upstream of the nozzle throat, ruptures. This allows the gas to exhaust through the nozzle into an evacuated receiver tank. The conical nozzle has a throat diameter of 0.100 inches, a total included angle of the diverging section of $15^{o}$, and an exit diameter of 3.25 inches. A baffle in the arc chamber shields the throat from the arc column and prevents large particles from entering the nozzle. For the metal condensation experiments, the sampling devices are placed in the receiver tank just downstream of the nozzle exit plane.

A schematic diagram of the energy supply system is shown in Fig. 4. This schematic shows that, with both the main transfer switch, $S_2$, and the arc chamber fuse switch, $S_3$, closed, the higher resistance of the path through $S_3$ will cause the majority of the current to pass through $S_2$. However, when $S_2$ is opened, all the current is forced to pass through $S_3$. This current causes the temperature of fuse-switch $S_3$, connecting the two coaxial copper electrodes within the arc chamber, to rise until the fuse's ultimate strength, which decreases with temperature, is less than the electromagnetic force on the fuse. At this time the

fuse breaks and an arc is initiated at the breakage point. In normal operation the fuse bends toward the outer electrode and the arc is transferred from across the broken fuse ends and establishes itself between the center and outer electrodes.

The delay time between the opening of $S_2$ and the fuse breakage is critical. If the time is too short, $S_2$ may not be completely open and an arc may strike there. If the time is too long, a large amount of the energy may be dissipated through circuit resistance. On the basis of operating experience, a fuse delay time of approximately 30 milliseconds is considered optimum.

## 2. 2 DESIGN AND TESTING OF THE ZINC FUSE

In designing the zinc-helium experiments for the hotshot, the most direct approach appeared to be the use of a zinc fuse and center electrode in place of the usual copper ones. In addition, if the arc could be encouraged to remain between the broken fuse ends, it appeared that a maximum amount of zinc would be vaporized and copper vapor contamination (from the outer electrode that, due to practical considerations, remained copper) could be held to a minimum. Since the fuse was designed to fail at a point adjacent to the center electrode, the zinc fuse was designed with a thick root, Fig. 5. This tended to keep the broken fuse tip close to the center electrode. It was hoped that this, in turn, would keep the arc burning between the zinc fuse tip and the zinc center electrode.

The zinc fuses and center electrodes were machined from commercially pure zinc castings. In the case of the fuse, a "flattened" shape was machined. This piece was bent to the required shape and then annealed at $300^{o}$F for one hour.

The fuse, shown in Fig. 5, was designed using the method described in Appendix A of Ref. 9. Figure 6 shows the calculated variation of the fuse cross-sectional area with buss bar current for several different fuse delay times. Although the zinc fuse was of the same general configuration as the experimentally proven copper fuse, its performance was evaluated by simple tests outside the arc chamber. These tests were made for two major purposes: (1) to determine

the reliability of the delay time prediction and (2) to ascertain, if possible, the mode of fuse breakage; i. e., determine whether a substantial amount melted before breakage or whether the fuse broke while still essentially solid.

Two tests were made with the sample fuses connected between the two external electrodes shown in Fig. 7. The external electrodes were used because they are much simpler to use than the arc chamber. Although the electrode shape is not the same as that in the arc chamber, the current path is quite similar and therefore the electromagnetic force on the fuse is representative of that occurring in the arc chamber. Because of the "rail" configuration of these test electrodes, as soon as the fuse breaks the arc transfers to the electrodes and is rapidly swept away from the fuse by the electromagnetic force on the arc column. This action tends to preserve the breaking configuration of the fuse permitting a meaningful evaluation of its breaking condition after the test.

A Fastax high speed motion picture camera (operating at a speed of approximately 1400 frames per second) was used to photograph, simultaneously, the fuse and the main transfer switch. The fuse delay time was determined by studying these pictures.

During the first fuse test, the buss bar current was 47,000 amperes and the measured delay time was 15 milliseconds. This compared favorably with the 11 millisecond value predicted by the calculations. Since a longer delay time was desired to reduce the possibility of arcing at the main switch, a second test was made with a fuse designed to delay 40 milliseconds at 40,000 amperes. The measured delay time was 48 milliseconds, again agreeing well with the predicted value.

The pictures from the first test revealed nothing about the manner in which the fuse broke. An improved camera placement for the second test resulted in the sequence of pictures shown in Fig. 8. The fuse appeared to melt at the edges and around the center hole before breaking. Subsequent examination of the fuse

breakage point revealed a smooth, melted appearance at these locations. However, a crystalline structure elsewhere along the break indicated a mechanical break due to the reduced tensile strength of the zinc at the elevated temperatures.

A third, and final, test was made with the fuse in its normal location inside the arc chamber, but with the downstream end of the arc chamber left open. A delay time of 37 milliseconds, at a buss bar current of 39,000 amperes, was achieved. This agreed well with the calculated value of 43 milliseconds. On the basis of this final test, the zinc fuse was considered satisfactory for use in regular hotshot operations.

## 2.3 DESCRIPTION OF THE CONDENSATION TESTS

Three zinc-in-helium runs were made. The operating and test conditions for these runs are given in Table I. The desired value of energy system current (which determines the energy available for transfer by the arc) was 40,000 amperes. This selection was based on desired maximum arc chamber conditions of 5000 psia and 5000$^{o}$K and on an estimated energy transfer efficiency of 60%. The indicated scatter in measured current resulted from difficulties in controlling and measuring the maximum current. These results show that the apparent transfer efficiency was about 35%; this is in approximate agreement with more recent operating experience at low charging pressures.

For Run No. 1, the sampler rake, shown in Fig. 9, was installed in a vertical position, 6 inches downstream of the nozzle exit plane. The platinum foil slides were installed to collect particle samples from the flow for spectrographic analysis. Nickel grids, coated with collodion, were attached to each sampler to collect particle samples for electronmicroscope studies. After the run, the inside surfaces of the arc chamber and nozzle were found to be coated with a fine grey dust. Samples of this dust were collected from the baffle plate for analysis to give an indication of the composition of particles formed in the arc chamber and upstream of the nozzle throat.

For Run No. 2, the sampler rake was installed in the same axial location but in a horizontal position. Platinum collector slides and nickel grids were used again. In addition, the sampling can, shown in Fig. 10, was installed above the rake. It was assumed that expansion of the flow entering the can would result in a diffuse deposit of solid material over the inside. However, the resulting pattern on the rear of the can indicated that the direction of the solid material in the flow remained unchanged after entering the can; no detectable diffusion occurred.

The particle samples collected from the nozzle flow on Runs 1 and 2 were typically too dense for satisfactory electronmicroscope photography. To alleviate this situation, the sampling drum, shown in Fig. 11, was used on Run No. 3. The face of the drum was located about 12 inches downstream of the nozzle exit plane. The height of the drum was 6 inches; it completely spanned the flow. The drum was coated with collodion and Biodine; convenient materials for preparing specimens for the electronmicroscope. During the run the drum was rotated at 900 rpm. This gave both a time-resolved sample of the solid material in the flow and the less dense deposit required for the electronmicroscope studies.

The rotational speed of 900 rpm resulted in one revolution in 67 milliseconds. The data from Run No. 3 showed that the arc chamber pressure had dropped to about 1/4 of its original value in that time. Thus, there was flow out of the arc chamber after one revolution of the drum and some overlap of the sample occurred.

To keep the time resolution of the sample as well defined as possible, it was desirable that the flow entering the drum housing remain in a beam prior to impinging on the drum. As a check of the flow field inside the drum housing, a trial run was made with the top and bottom of the drum housing removed and the housing in a horizontal orientation. Room temperature nitrogen was used at a

supply pressure of 2400 psia; the receiver pressure was about 1.0 mm. Hg. Schlieren Fastax pictures were taken of the flow and shock configuration; a sample frame is shown in Fig. 12. These pictures indicate that the flow actually remains in a beam until it impinges on the cylinder.

Four samplers with gold foil slides were installed in the holders shown in Fig. 13. They were located 6 inches downstream of the nozzle exit plane, at distances of 3/4 and 1-1/2 inches from the tunnel centerline on each side of the drum housing. The slides were weighed before and after the run to obtain preliminary data on the radial distribution of the total (time integrated) solid particle mass flow.

## 2.4 TEST RESULTS AND DISCUSSION

There is no provision in the Hotshot Wind Tunnel system for direct measurement of the arc chamber temperature. It is common practice to calculate this temperature on the basis of the charging gas density (assumed constant during the arcing process) and the measured chamber pressure. However, due to the uncertainty of the composition of the gaseous mixture in the present experiments, the exact chamber temperature could not be determined in such a simple manner. Only the possible range of the chamber temperature could be calculated.

If it is assumed that no zinc vapor exists in the arc chamber, the chamber temperature can be calculated easily from the perfect gas law and the values of the measured chamber pressure and the charging density of the helium. This determines the upper bound of the chamber temperature.

A lower bound for the chamber temperature can be determined as follows. In Runs Nos. 2 and 3, the zinc fuse and center electrode were weighed before and after the run to determine the zinc lost during the run. These losses are listed in Table I as are the corresponding zinc mass fractions of the mixture. If all the zinc, lost from the fuse and electrode, is assumed to be vaporized, the ratio of the zinc and helium vapor pressures can be calculated directly from

the molecular weights and known masses of zinc and helium. The total chamber pressure, which is the sum of the partial pressures of the zinc and the helium, can then be compared to the measured maximum chamber pressure and, using the perfect gas law, a corresponding chamber temperature can be computed. This temperature represents the lower bound for the maximum arc chamber temperature.

These upper and lower bounds for the arc chamber temperature, for Run Nos. 2 and 3, are listed in Table I. Also shown for comparison purposes, are the temperatures for saturated zinc vapor in the arc chamber and the corresponding masses of zinc vapor required for saturation. The actual chamber temperature should be located between the upper and lower temperature bounds, since it is likely that some of the zinc, lost from the fuse and electrode, remained in liquid or solid form. But, in any case, the zinc that was in vapor form (at least for Run Nos. 2 and 3) was superheated in the arc chamber. The amount of superheating of zinc vapor is suggested by Fig. 14, which illustrates the case where all the zinc lost from the fuse and electrode was in the vapor state.

Table I also shows the energy increments necessary to achieve the computed maximum arc chamber conditions. Values corresponding to the zinc-free temperature and the lower bound temperature (Run Nos. 2 and 3 only) are included. The energy increments were determined by the use of Fig. A-1; the calculations leading to Fig. A-1 are described in Appendix A.

In Run Nos. 1 and 2, the time integrated particles samples collected from the flow stream, as well as the dust collected from the inside of the arc chamber, were analysed spectroscopically by the Chicago Spectro Service Laboratory. The complete results of these analyses are presented in Table II. Also shown are the results of an analysis of the zinc that was used to make the fuse and the center electrode. By comparing these results, it is seen that contaminants (principally copper, iron, and silicon) were added to the mixture in the arc

chamber. The probable source of copper was the beryllium-copper lower body of the center electrode and the arc chamber liner (which serves as the outer electrode). The probable source of iron was the steel baffle plate upstream of the throat, which is exposed directly to the arc. The only source of silicon was the silicon grease that is used generously in assembling the arc chamber and in filling the pressure transducer port. In Run No. 2, the amount of silicon grease used in assembly was substantially reduced; no significant reduction in silicon contaminant was observed. The total percentage of all contaminants is small but the effect of these contaminants to the zinc condensation process is not known. Arthur (Ref. 2) shows for the case of condensing nitrogen, that small amounts of contaminating material, if in the form of very small nuclei, can cause major changes in the condensation process. For example, the condensation may occur completely as condensation onto the contaminating nuclei rather than as nucleation and growth in the condensing vapor.

Particles samples, collected from the flow stream during all three runs, were photographed by an electronmicroscope. A typical photomicrograph is shown in Fig. 15. It is seen that most of the particles appear round and that the variation in particle size is small.

One arbitrarily picked photomicrograph, for each run, was analysed to determine the particle size distribution. To do this, each selected photomicrograph was divided arbitrarily into several segments. All the particles in each of three arbitrarily chosen segments, for each photomicrograph, were counted and classified by size; e. g. , all particles have diameters between 0. 08 and 0. 10 microns were counted as a single class. These data were averaged for each of the photomicrographs and the size distribution curves, shown in Fig. 16, were determined. To show the probability of finding a particle of a particular size, the normalized probability of occurrence is used as the ordinate for the distribution curves. The probability of occurrence values were obtained as follows.

The average number of particles found in each class was normalized by the total number of particles of all classes. Then the resulting number fraction was divided by the class width; e. g., the number fraction of particles with diameters between 0. 08 and 0. 10 microns was divided by 0. 02 microns. This number was plotted against the diameter corresponding to the center of the class. It should be noted that the integral of the distribution curve is unity.

Figure 16 also shows the sizes, shapes, and locations of the samplers. Despite the differences in the samplers and their locations, the results of Run Nos. 1 and 2 were very similar. Note that the samples from Run Nos. 1 and 2 were time integrated; i. e., collected over the entire run length. Both curves show a sharp increase in the number of particles occuring at diameters less than 0. 1 microns and an apparent maximum probability in the neighborhood of 0. 02 to 0. 04 microns. The magnification of the photomicrographs was not large enough to determine whether the apparent maximum occured because of the absence of smaller particles (either because they are not present in the flow or because they have failed to reach the collector) or because the magnification was too small to resolve the small particles. In any case, it is evident that the majority of the particles were much less than 0. 1 micron in diameter.

The curve for Run No. 3 was flatter and did not show an apparent maximum. However, most of the particles again occur at diameters less than 0. 1 micron. The difference in curve shape between that for Run No. 3 and the previous runs may be due to two reasons. First, the Run No. 3 sample was time resolved, corresponding to a time 9. 25 milliseconds after the beginning of the run. Second, the sample was taken very near the flow centerline where the larger particles, coming from the arc chamber, are expected to be more numerous. Much additional analysis, of the material collected by the rotating drum, will be required to establish a valid comparison with the time integrated samples.

A photograph of the drum sampler, taken after Run No. 3, is shown in Fig. 17. The drum surface was coated by a light deposit of blackish particles

everywhere except in the center. In the center of the drum, corresponding to the central core of the conical flow field, there was a distinct opaque gray band. The width of this band was approximately the same as the nozzle throat diameter, 0.1 inches. The band appeared to be a dense deposit of particles. It appears that a beam of particles, that were formed in the arc chamber, was focused on the flow centerline by the throat and was not diffused by the diverging flow.

The four gold foils used for Run No. 3 to collect samples for spectral analysis, were weighed before and after the run to determine the total weight of material collected during the run. The results of the weighings are shown in Fig. 18. These results show that the mass flow of the particles is not uniformly distributed. The sharp increase near the flow centerline again suggests the focusing of particles coming from the arc chamber. Condensation in the nozzle should occur uniformly over the inviscid core, resulting in a relatively uniform particles mass flow rate. These results, together with the particle pattern observed on the drum surface, suggest that most of the particles found in the nozzle flow were generated in the arc chamber itself and did not result from condensation in the nozzle.

Round impressions were observed on the back of the gold foils. These 'bumps' were as large as 1/64 inch in diameter and were probably formed by the im-pingement of large particles coming from the arc chamber. It appears that these large particles struck the foils during the early part of the run because the front surfaces of the foils were covered uniformly by a smooth deposit of very fine particles.

# 3. LIGHT SCATTERING STUDIES

## 3.1 Background

The phenomena of electromagnetic radiation scattering from a cloud of small particles (e. g. , aerosols, colloidal solutions, etc. ) produce effects that can be measured to obtain information about the scattering particles themselves. For example, the visible light scattered by appropriate solutions is used to determine the molecular weight of complex molecules. In fact, light scattering is a standard experimental technique in the field of physical chemistry (e. g. , see Ref. 10 and Chapter 19 of Ref. 11). In addition, light scattering has been used in the fields of meterology and astronomy since the beginning of the present century; e. g. , see Chapters 20 and 21 of Ref. 11.

In searching for instrumentation techniques for studying condensation phenomena, it appeared that light scattering could be applied. The size and growth rate of the condensed particles are quantities of primary interest in the present study. While, in the case of metallic condensates, it is possible to sample solid particles directly from the high speed stream, such is not the case for condensed gases (e. g. , nitrogen and argon). In the latter situation, the condensed particles would evaporate on contact with room temperature sampling devices. However, the size of the scattering particle is the quantity most directly determined by scattered light measurements and such measurements can be made without disturbing the flow. Appendix B presents a discussion of light scattering theory and its application to the measurement of the size and number density of condensed particles. The response characteristics of photomultiplier sensors, used to measure the scattered light, are such that quasi-steady flows, as generated in the hotshot wind tunnel, can be studied conveniently.

Although light scattering and absorption techniques have been used by many investigators of condensation phenomena, there apparently are relatively

few cases where light scattering has been used to study condensation in flowing systems. Perhaps the earliest such investigation was by Stodola (Ref. 1) who studied condensation in steam nozzles. Later, similar studies were made of the condensation of water vapor in air (e. g., Ref. 12) and of air in hypersonic wind tunnels (e. g., Refs. 13 and 14). These studies were mainly qualitative; light scattering was used to detect the presence of condensation rather than to obtain information about the condensed particles. (Stodola is an exception, since he used his observations to estimate the size of the water droplets.) A summary of the application of light scattering techniques to condensation experiments in flowing systems is presented by Winkler in Ref. 15.

Quantitative results from light scattering measurements in flowing systems appear to be limited to the studies of air condensation in hypersonic nozzles presented in Refs. 16 and 17. Reference 16 discusses an experimental arrangement for making such measurements and presents a single preliminary result. In Ref. 17, a large number of measurements are reported. An interesting feature of these measurements is that it was possible to follow the growth of the condensed particles as they traveled through the nozzle.

The extent to which light scattering can be applied to the study of condensation phenomena depends on its basic sensitivity. Without considering the problems involved in general polydisperse systems (i. e., systems containing particles of many different sizes), a preliminary evaluation of its applicability can be obtained from a relatively simple theoretical example. Appendix C presents an analysis of attenuation and scattering at $90^{o}$, of visible light, by a binary mixture of uncondensed gas and condensed droplets of uniform size. The results of this analysis indicate the extreme sensitivity of the instrumentation that is required to measure the size and number density of condensed particles, particularily during the early phases of condensation when the particles are small and their numbers are few.

In applying light scattering to the condensation studies planned under the present contract, the general procedure described by Durbin in Ref. 16 was followed. The overall objective was to develop a suitable light scattering apparatus and to apply it to the metal vapor experiments as soon as they were being made on a reliable basis. The development of the system was to be aided by experience gained by using it on condensing flows of pure gases, e. g., nitrogen and argon.

## 3. 2 FREE JET CONDENSATION STUDIES

Some experience in the use of light scattering instrumentation was obtained by making light scattering measurements on the condensation occurring in a nitrogen free jet issuing from a sonic orifice. The instrumentation used for these measurements is described in Appendix D. In these experiments, the hotshot arc chamber was used only as a pressure vessel. The chamber was charged with nitrogen at high pressures and room temperature by means of a hydrostatic pump capable of supplying pressures up to 6000 psi. The arc chamber nozzle section, Fig. 19,was arranged to give a sonic exit discharging to the atmosphere. Initially the orifice was blocked by a teflon plug held in place by the "Mark II" pressure release mechanism shown in Fig. 20. The release mechanism was triggered by the same switch that triggered the oscilloscope used to record the output of the photomultipliers.

The structure of the underexpanded jet is illustrated in Fig. 21. The Mach disk is a strong wave behind which the flow is subsonic and at nearly room temperature. It was expected that the state change across this shock wave would substantially alter the condensate; a rapid evaporation of the condensed particles is most likely. To avoid the effects of the shock wave, all measurements were made upstream of the Mach disk. The location of the Mach disk was determined from results of schlieren Fastax studies of the underexpanded jet flow fields reported in Ref. 18. A pressure ratio of about 400, obtained with a supply pressure of about 6000 psia discharging to the

atmosphere, was necessary to keep the Mach disc far enough from the exit plane, as well as to obtain a large enough jet diameter, to allow a reasonable field of study. The arc chamber could be moved axially, relative to the fixed light scattering system, to permit a detailed study of the condensation process between the nozzle exit and the Mach disk.

Close to the nozzle exit, the free jet expansion rate is extremely high. At high supply pressures, this high expansion rate results in the onset of a very high condensation rate within a very small distance downstream of the exit plane. This effect is illustrated by the numerical results presented in Fig. 22. These results were obtained from numerical computations of the condensation process occurring in an underexpanded nitrogen jet. The effective conical flow geometry, used for the calculations, was based on the data given in Ref. 19.

Due to the rapid geometrical expansion of the jet structure near the nozzle exit, the light beam entered the jet boundary at an appreciable oblique angle resulting in refraction of the beam. This partial deviation of the beam, from the view path of the photomultipliers, resulted in an apparent attenuation of the transmitted light beam which was not differentiable from the attenuation caused by condensation. In some cases this "attenuation" approached 100% near the nozzle exit. Thus it was not possible to obtain an indication of the condensation onset point or data on the condensation process occurring close to the nozzle exit.

All tests were made at supply pressures on the order of 6000 psi. The resulting condensation levels were high enough to cause from 30 to 70% attenuation of the transmitted light beam in the region upstream of the Mach disk. Since single scattering theory is valid only for attenuations on the order of 10% or less, values of particle size and number density, determined on the

basis of these measurements, were considered invalid. Attempts to infer quantitative results from these measurements would be made additionally difficult by the three-dimensional nature of the jet, which leads to non-uniform condensation conditions along the optical path.

The intensity of the scattered light from the condensed particles was extremely low. The resulting photomultiplier outputs were too low to permit an accurate reading of the data. An additional difficulty occurred because at such low light level operations, the signal to noise ratio of the photomultiplier output is of the order of one or less. Therefore, the scattered light channels also failed to provide usable data.

# 4. PHOTOMICROGRAPHY STUDIES

Photographic techniques have been used previously to gather information on small moving particles. Streak pictures of small particles have been used to investigate the flow patterns in boundary layers, Refs. 20 and 21. Photographs of slowly moving drops have been used to investigate the drop size distribution of atomized fuel, Ref. 22. Also, photographs of small airborne particles have been taken successfully by means of photomicrography techniques, Ref. 23. However, there apparently has been no work done on photography of micron size particles moving at very high speed.

One of the objectives of the present program was the investigation of the application of photomicrography techniques to the problem of determining the size and number density of condensed particles in a high speed flow. Besides the ordinary resolving power problems involved in photomicrography, the following two additional problems were considered;

1. the necessary illuminance of the light source, and
2. the time duration of the exposure.

In addition, two types of illumination were considered; namely, "bright field" and "dark field" illumination. Due to the infeasibility (see Appendix E) of bright field photography for high speed particles, only the application of the dark field illuminating system was investigated in detail.

At the time the photomicrography studies were begun, it was thought that the condensing particles would have sizes on the order of one micron ($10^{-4}$ cm.) and would be traveling at velocities up to 10,000 ft/sec. In addition, some evidence existed that the number density of the condensed particles might be as large as $10^{8}$ per $cm^{3}$. It was necessary, therefore, to consider the magnification and illumination (both light intensity and duration) requirements of the photomicrographic system from the point of view of these factors. These performance requirements are discussed in Appendix F.

In order to obtain experience in photographing small particles carried by a high speed flow, some photomicrographic experiments were carried out. These experiments also provided experimental performance data to compare with estimates based on the discussions of Appendix F. The experiments and their results are discussed in detail in the following paragraphs.

## 4.1 EXPERIMENTAL EQUIPMENT

The photomicrographic experiments were carried out in a slightly supersonic stream that was seeded with particles of various sizes and illuminated by a spark light source. Streak pictures were taken and the resulting calculated particle sizes were compared with the known sizes. The particles were added to the nitrogen stream with the ejector apparatus shown schematically in Fig. 23. There were two flow lines in the system, both of which used high pressure bottled nitrogen as the gas source. Referring to the figure, a small number of particles were picked up and carried into the mixing chamber by the secondary nitrogen stream as it passed through the particle container. In the mixing chamber, the particles carried by the secondary stream were mixed with the primary stream and the resulting mixture exhausted through a convergent nozzle with a 0.1 inch diameter throat. In order to minimize the consumption of particles, the duration of the secondary stream was controlled by the solenoid valve and was limited to the 3 to 4 seconds needed to take a picture.

The system provided no control of the exact amount of particles added to the stream. The relative quantity of particles that could be "picked up" was dependent on the flow rate of secondary stream that was controlled by the pressure difference between the two flow streams. The pressure of each stream was controlled by the loading pressure of the Grove dome regulator.

The seeded jet was illuminated by an open electrode spark source, energized by capacitors storing a maximum energy of 24 joules at 20 kv. Its

construction is shown schematically in Fig. 24 and its operation is discussed in Appendix H. Appendix H shows that maximum energy output was too small to be measured by a thermopile instrument, but its light intensity was measured photographically and found to be $8 \times 10^6$ candles/cm$^2$. The effective duration of the light pulse was measured and found to be about 5 microseconds. The spectrum of the spark was recorded by a Huet Prism Spectrograph. Very intense lines appeared in the region of 4550 Å to 4770 Å. These results were used as a guide in choosing film.

A standard press camera, with a 4 x 5 inch ground glass viewing screen, was modified by substituting a standard Bausch and Lomb compound microscope for the regular camera lens. The achromatic objective used had a NA of 0. 1. The magnification of the assembly was determined from the image of a 0. 062 inch diameter wire. A synchronized compur shutter was placed between the microscope and the camera-back and was used to decrease the background exposure due to stray light. The exposure of photographs was determined by the duration of light pulse.

Four-by-five inch Polaroid type 57 sheet film, having an ASA rating of 3200, was used for all the experiments. Its resolving power is 18 to 26 lines/mm. This film was chosen for its convenience of handling and its high sensitivity in the region where the most intense lines in the spark spectrum were located.

A photograph of the set-up of the ejector, the spark source and the camera is shown in Fig. 25. The relative positions of the several components are shown schematically in Fig. 26. The camera axis was located in a plane perpendicular to the jet axis and intersected the jet axis 5/8 inch downstream of the nozzle exit, where the jet began to diverge. The light source axis intersected the jet axis at this same point. The light from the spark source was condensed into a spot about 1/8 inch in diameter to yield high illumination

of the intersection of the three axes. The alignment of the axes was made by focusing the camera on a 0.062 inch wire that was placed in the center of the jet path and visually adjusting the light source for maximum illumination.

## 4.2 EXPERIMENTAL PROCEDURE

Both stationary and streak photographs were used to evaluate the procedure for determining particle sizes from photographs. Appendix G discusses the theoretical relationship between the particle size and the size of the image on the photograph.

In the stationary particle photograph experiment, the set-up was as described above except that no nitrogen jet was used. Particles were dusted lightly onto a microscopic slide that was placed at the focusing point of the light beam and the camera. Prior to adding the particles, the microscopic slide was blackened by an acetylene flame to reduce its surface reflection and improve the image contrast of the particles. The picture was taken by triggering the spark source.

In taking pictures of moving particles, it was found necessary to add the right amount of particles to the jet. If too many particles were added, the picture was "washed out"; the streaks could not be distinquished. If too few particles were added, either none or only a few particles appeared in the picture. Since there was no way to control the exact number of particles added to the jet, the relative quantity of particles in the jet was determined solely by the appearance of the jet. A densely seeded jet appeared white and opaque; a sparsely seeded jet appeared bluish. The density of particles in the jet appeared quite steady after the surge that occasionally occurred immediately following the opening of the solenoid valve. The picture was taken, as soon as the seeded flow appeared steady, by triggering the spark source.

The mixing chamber pressure was kept above 30 psig to insure a choked flow in the throat. The speed of moving particles was determined from the streak lengths and the duration of the light pulse and found to be about 930 ft/sec. This is near the choked flow speed at the throat for a room temperature nitrogen supply.

For both experiments, two types of particles were tried; 74-150 $\mu$(dia.) black glass beads, manufactured by Potters Brothers, Inc., and 1-30 $\mu$(dia.) Superbrite glass beads, manufactured by Minnesota Mining and Manufacturing Company. The glass beads were all spherical in shape but only the Superbrite beads were transparent. The sizes of the beads were checked visually with a high power microscope, but no size distributions were measured.

Both the streak photographs and stationary photographs were measured with a comparator for the particle size estimation. The comparator had a magnification of 10 and its smallest scale was 0.2 mm. Only the sharpest images were used for the analysis.

## 4.3 RESULTS

Typical photographs of stationary and moving particles are shown in Fig. 27. Their results will be discussed separately in the following paragraphs.

From the photographs of the stationary particles, it was found that, due to internal reflections, several high lights appeared on the Superbrite glass beads. Thus, the correct image of the light source on those beads could not be identified. In the case of the black beads, the internal reflections were decreased substantially and the high light could be identified readily. Therefore, only the data for the 74-150 $\mu$ black beads were analyzed.

The high light, as well as the corresponding particle image, was measured. Equation (G-3) of Appendix G was used to calculate the particle size on the basis of the high light diameter. Invariably, the calculated particle size was

larger than the measured particle size. Assuming the particle size measured from the photographs to be correct, the data were reduced to the form of the ratio between the calculated and measured particle sizes. The results are shown in Fig. 28. Each point in the figure actually represents several independent measurements. The indicated error boundaries are due to the fact that the high lights measured from the photograph were in the range of 0.2 ~ 0.3 mm which was very close to the lowest scale of the comparator; the maximum reading error was 50%.

The photographs of moving particles indicated little difference between the streaks produced by the black and the Superbrite beads, except that the streaks from black beads were sharper. It was possible that the fuzzy streaks from Superbrite beads were due to internal reflection noted in the stationary photographs. Only the streak photographs of the 74-150 $\mu$ black beads were analyzed. The particle sizes were computed by the use of Eq. (G-3) of Appendix G. The results are tabulated in Table III. It is seen that the computed particle sizes are much larger than the particles which were used.

If the errors involved in the streak photography are assumed to be the same as for the stationary photographs, the actual particle size can be obtained by adjusting the computed particle diameters by the ratio determined from the stationary photographs. Therefore, if on the basis of Fig. 28 the mean ratio is taken as 4, the computed particle diameters presented in Table III can be corrected. These corrected values are shown also in Table III. These corrected values agree well with the range of particle diameters used. Therefore, it is believed that a reasonable estimate of particle size can be obtained from a streak photograph, provided that the correction factor for the photographic system is known.

The streak photographs were used also to obtain an estimate of the light source requirement. The reflection density of streaks on the photographs was measured to be 0.3 by comparison with a Kodak Calibrated Gray Scale.

The corresponding exposure, $2.2 \times 10^3$ lumen-sec/meter$^2$, was determined from the published Polaroid film characteristic curves. Substituting this value and other known values of the optical system into Eq. (F-5) of Appendix F, the illuminance of the spark source was found to be $1.09 \times 10^7$ candles/cm$^2$. This is very close to the value $8 \times 10^6$ candles/cm$^2$ that was measured by a different method and reported in Appendix H. Therefore, despite the crude assumptions, Eq. (F-5) gave a fairly good estimation of the light source illuminance.

## 4.8 CONCLUSIONS

Some problems involved in the application of photomicrography techniques to the study of small high-speed condensed particles have been discussed above. This study has resulted in the following conclusions.

(1) Due to the sub-nanosecond exposure time requirements for bright field photography, only dark field photography is feasible at this time. The exposure time requirement for dark field photography (resulting in streak photographs) is governed by both particle velocity and number density and is in the sub-microsecond range.

(2) The performance of the best conventional flash light sources is not adequate for photography of small high speed particles; e. g., the photography of one micron diameter high lights (the particles may be 10 times or more larger) requires a minimum magnification of 25 for image resolution on the film; this allows a maximum particle velocity of about 240 ft/sec. A high energy laser light source gives more latitude in allowable magnification and particle velocity; one to two orders of magnitude improvement appears possible.

(3) The photographic system is capable of resolving particles with number densities the same order of magnitude as those measured in wind tunnels ($10^8$ particles/$cm^3$), provided that the exposure time is less than 0. 1 microsecond and the numerical aperture of the objective is larger than 0. 25.

(4) Particle sizes can be calculated from streak photographs of the particle high lights provided that the photographic system is calibrated using stationary photographs of particles of known size.

(5) A method for estimating light source output energy requirements has been checked experimentally and found to give fairly good results.

## REFERENCES


1. Stodola, A., Steam and Gas Turbines, Vol. II, pp. 1934-1075, McGraw-Hill, 1927.

2. Arthur, P. D., "Effects of Impurities on the Supersaturation of Nitrogen in a Hypersonic Wind Tunnel", Ph. D. Thesis, California Institute of Technology, 1952.

3. Stever, H. G., "Condensation in High Speed Flows", High Speed Aerodynamics and Jet Propulsion, Vol. III, pp. 526-573, Princeton University Press, Princeton, N. J., 1958.

4. Wegener, P. P., and Mack, L. M., "Condensation in Supersonic and Hypersonic Wind Tunnels", Advances in Applied Mechanics, Vol. V, pp. 307-447, Academic Press, 1958.

5. Daum, F. L., "The Condensation of Air in a Hypersonic Wind Tunnel", IAS Paper No. 63-53, Institute of the Aerospace Sciences, New York 1963. Also published in AIAA Journal, Vol. I, No. 5, pp. 1043-1046, May 1963.

6. Cox, A. L., "Colloidal Electrohydrodynamic Energy Converter", AIAA Journal, Vol. 1, No. 11, pp. 2491-2497, November 1963.

7. Norgren, C. T., "Onboard Colloidal Particle Generator for Electrostatic Engines", Progress in Astronautics and Aeronautics, Vol. 9, pp. 407-434, Academic Press, New York, 1963.

8. Hultgren, R., et al., Selected Values of Thermodynamic Properties of Metals and Alloys, John Wiley and Sons, Inc., New York 1963.

9. Sherman, P. M., "Development and Operation of an Arc Heated Hypersonic Tunnel", University of Michigan Report 02953-3-F, July 1963.

10. Stacey, K. A., Light-Scattering in Physical Chemistry, Academic Press, New York 1956.

11. Van de Hulst, H. C., Light Scattering by Small Particles, John Wiley and Sons, 1957.

12. Head, R. M., "Investigation of Spontaneous Condensation Phenomena", Ph. D. Thesis, California Institute of Technology, 1949.

REFERENCES continued.

13. Stever, H. G., and Rathbun, K. C., "Theoretical and Experimental Investigation of Condensation of Air in Hypersonic Wind Tunnels", NACA TN 2559, November 1961.

14. Hansen, C. F., and Nothwang, G. L., "Condensation of Air in Supersonic Wind Tunnels and Its Effects on Flow About Models", NACA TN 2690. April 1952.

15. Winkler, E. M., "Condensation Study by Absorption or Scattering of Light", High Speed Aerodynamics and Jet Propulsion, Vol. IX, Physical Measurements in Gas Dynamics and Combustion, pp. 289-306, Princeton University Press, Princeton, New Jersey, 1954.

16. Durbin, E. J., "Optical Methods Involving Light Scattering for Measuring Size and Concentration of Condensation Particles in Supercooled Hypersonic Flow", NACA TN 2441, August 1951.

17. McLellan, C. H., and Williams, T. W., "Liquefaction of Air in the Langley 11-inch Hypersonic Tunnel", NACA TN 3302, October 1954.

18. Sherman, P. M., Glass, D. R., and Crist, S. A., "An Experimental Study of the Shock Structure of a Jet Exhausting from a Highly Underexpanded Sonic Nozzle", Vol. II of the 5th Annual Report No. 4613-73-F, Ballistic Missile Radiation Analytical Center, IST, Willow Run Lab., University of Michigan.

19. Owen, P. L., and Thornhill, C. K., "The Flow in an Axially-Symmetric Supersonic Jet from a Nearly Sonic Orifice into a Vacuum", Brit., A. R. C. Tech. Report RM 2616, 1952.

20. Eichhorn, R., "Measurement of Low Speed Gas Flows by Particle Trajectories: A New Determination of Free Convection Velocity Profile", Int. J. Heat Mass Transfer, Vol. 5, pp. 915-928, 1962.

21. Chen, C. J., and Emrich, R. J., "Investigation of the Shock Tube Boundary Layer by a Tracer Method", Physics of Fluid, Vol. 6, No. 1, Jan 1963.

22. York, J., and Stubbs, H. E., "Photographic Analysis of Sprays", ASME Paper No. 51-A-48, Presented at the Annual Meeting, Atlantic City, N. J., November 25-30, 1951.

23. Cadle, R. D., and Wiggins, E. J., "Direct Photomicrography of Air-Borne Particles", AMA Archieves of Industrial Health, Vol. 12, No. 6, Dec 1955.

TABLE I

OPERATING AND TEST CONDITIONS FOR THE ZINC CONDENSATION TESTS

| | RUN NO. | | |
|---|---|---|---|
| | 1 | 2 | 3 |
| Helium charging pressure, psia | 305 | 305 | 305 |
| Calculated mass of helium, gm | 3.61 | 3.61 | 3.61 |
| Receiver pressure, mm Hg | 0.1 | 0.1 | 0.1 |
| Measured maximum current, amps | 37,500 | 40,000 | 46,000 |
| Measured maximum arc chamber pressure, psia | 2400 | 2900 | 3400 |
| Measured loss of zinc from fuse and center electrode, gm | ---- | 7.55 | 1.4 |
| Corresponding mass fraction of zinc | ---- | .68 | .28 |
| Zinc required to saturate mixture, gm | 22.8 | 34.0 | 43.4 |
| Calculated maximum arc chamber temperature, $^{o}$K: | | | |
| Zinc-free | 2400 | 2900 | 3400 |
| All lost zinc in the vapor state | ---- | 2570 | 3320 |
| Saturated mixture | 1730 | 1850 | 1950 |
| Calculated nozzle exit velocity (on basis of zinc-free temperature), ft/sec | 16,300 | 18,000 | 19,500 |
| Energy stored in coil (at maximum current), joules | 84,400 | 96,000 | 127,000 |
| Computed energy input to mixture in arc chamber, joules: | | | |
| Zinc-free | 27,100 | 29,350 | 35,000 |
| All lost zinc in the vapor state | ------ | 44,600 | 37,800 |

TABLE II

QUALITATIVE SPECTROCHEMICAL ANALYSIS*
OF PARTICLE SAMPLES

| | MASS FRACTION IN PERCENT | | | | |
|---|---|---|---|---|---|
| | | RUN NO. 1 | | RUN NO. 2 | |
| | Fuse Material | Flow | Inside of Arc Chamber | Flow | Inside of Arc Chamber |
| Silicon | | .05 to .5 | .5 | Low | .3 to 3 |
| Copper | .002 | .03 to .3 | .3 | Low | .3 to 3 |
| Iron | .01 | .003 to .03 | .08 | No quantatative evaluation was obtained due to the small amount of samples collected | .5 to 5 |
| Tin | <.002 | .001 to .01 | ——— | | ——— |
| Magnesium | <.0005 | .0005 to .005 | .01 | | .003 to .03 |
| Silver | ——— | .0001 to .001 | .0003 | | .0005 to .005 |
| Nickel | ——— | .0001 to .001 | ——— | | .0001 to .001 |
| Calcium | ——— | .0001 to .001 | .001 | | .001 to .01 |
| Aluminum | <.001 | ——— | .008 | | .005 to .05 |
| Molybdenum | ——— | ——— | .005 | | .005 to .05 |
| Manganese | ——— | ——— | .001 | | .005 to .05 |
| Boron | ——— | ——— | .001 | | ——— |
| Chromium | ——— | ——— | .0005 | | <.0001 |
| Beryllium | ——— | ——— | ——— | | .0005 to .005 |
| Cadmium | .0015 | ——— | ——— | | ——— |
| Lead | .002 | ——— | ——— | | .001 to .01 |
| Cobalt | ——— | ——— | ——— | | .0001 to .001 |
| Zinc | ——— Balance ——— | | | | |

*Obtained by Chicago Spectro Service Laboratory.

TABLE III

RESULTS FROM PHOTOGRAPHS OF MOVING BLACK GLASS BEADS, 74 TO 150 MICRONS IN DIAMETER

| Number of Measure-ments | Width of Streaks, mm | Calculated Diameter, microns | Corrected Diameter, microns |
|---|---|---|---|
| 14 | 0.2 | 242 | 61 |
| 5 | 0.3 | 363 | 91 |
| 4 | 0.4 | 484 | 121 |

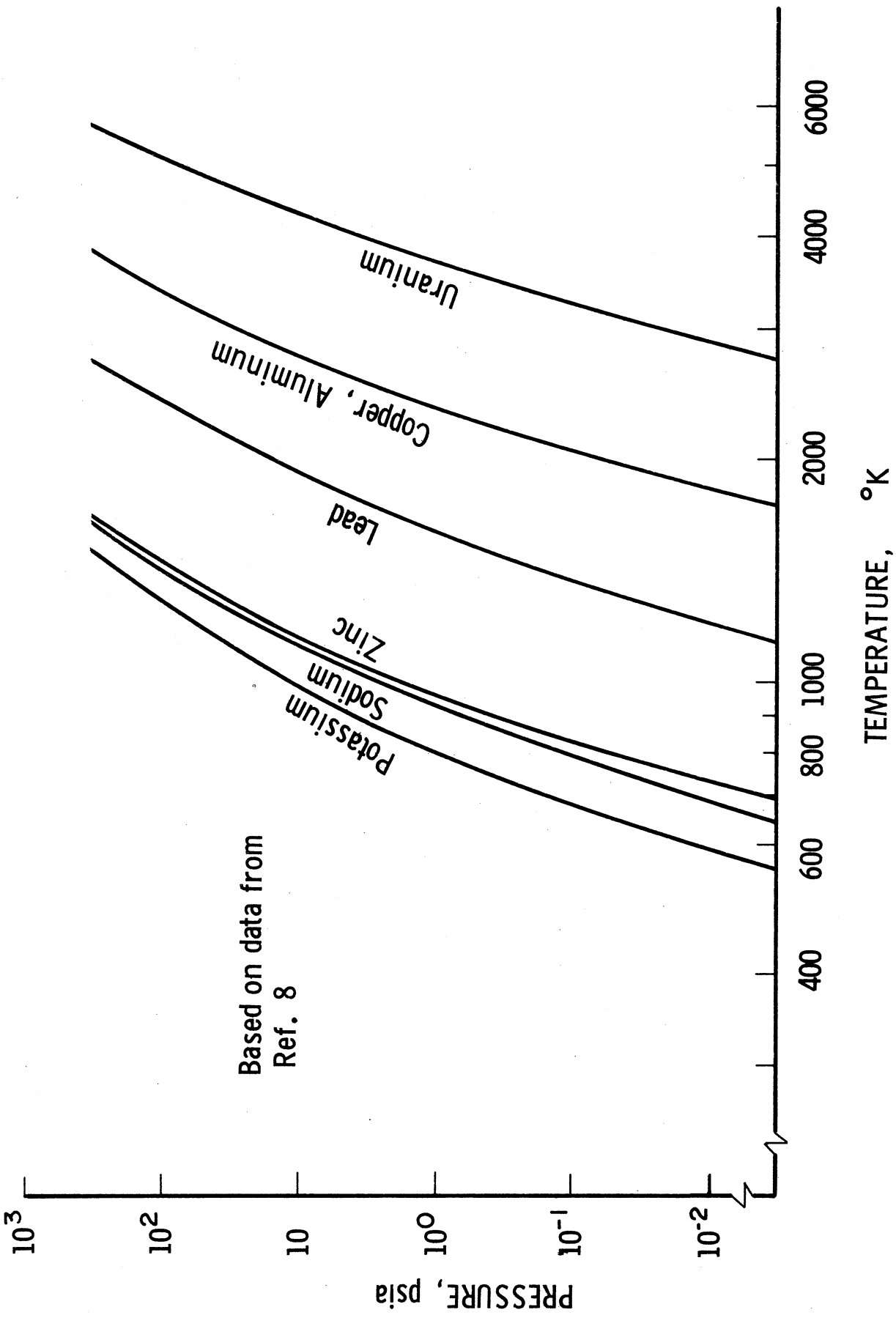


Figure 1. Vapor Pressure of Metals

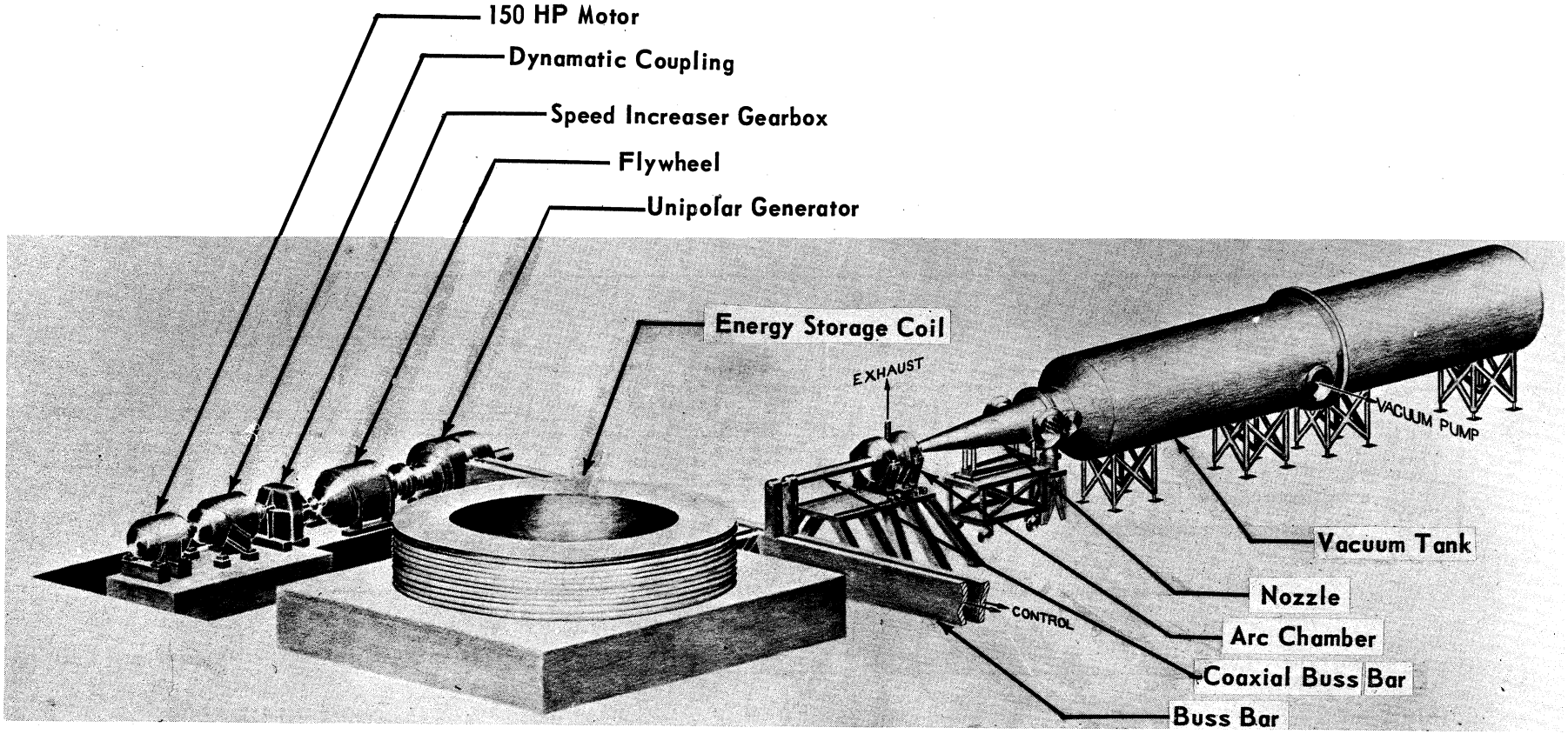


Figure 2. Hotshot Wind Tunnel Facility

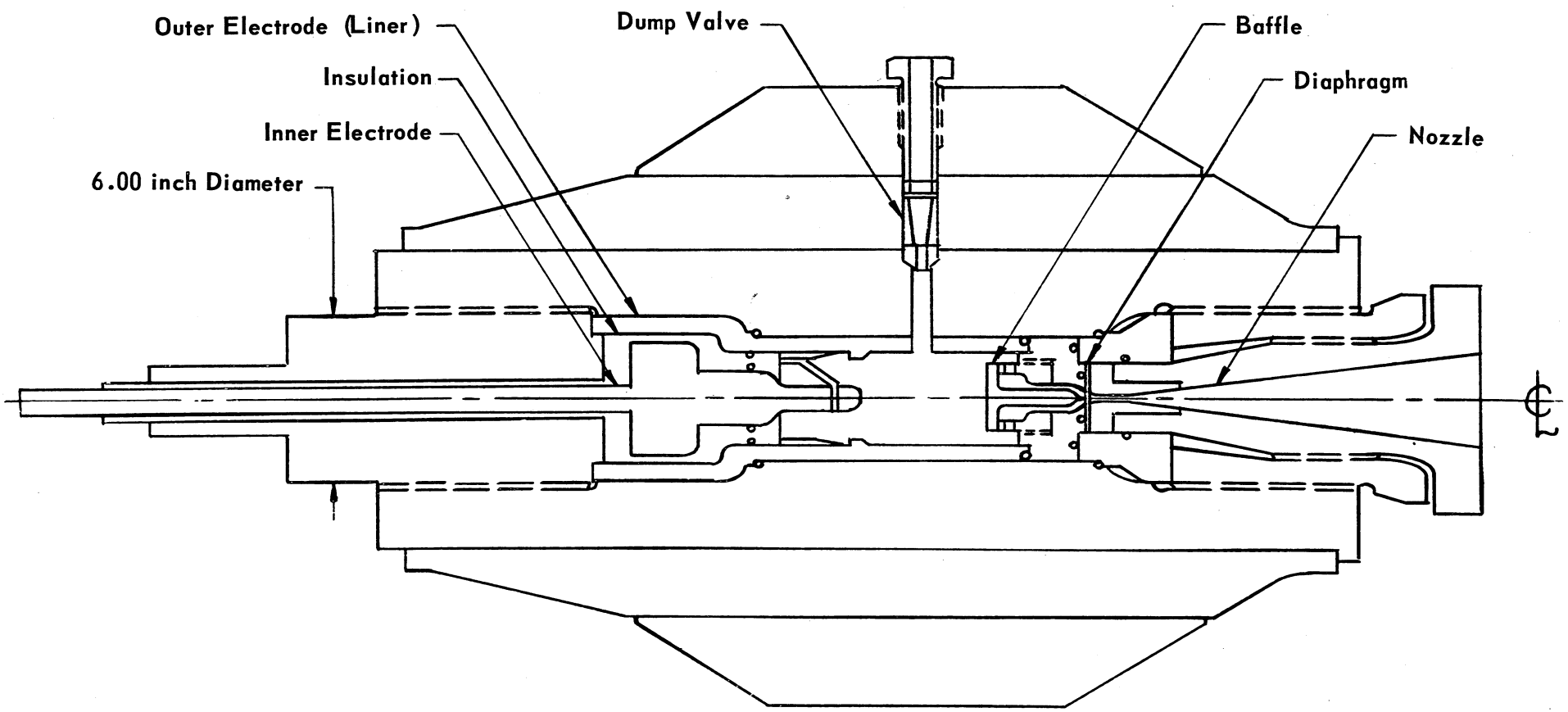


Figure 3. Sketch of the Hotshot Arc Chamber Assembly

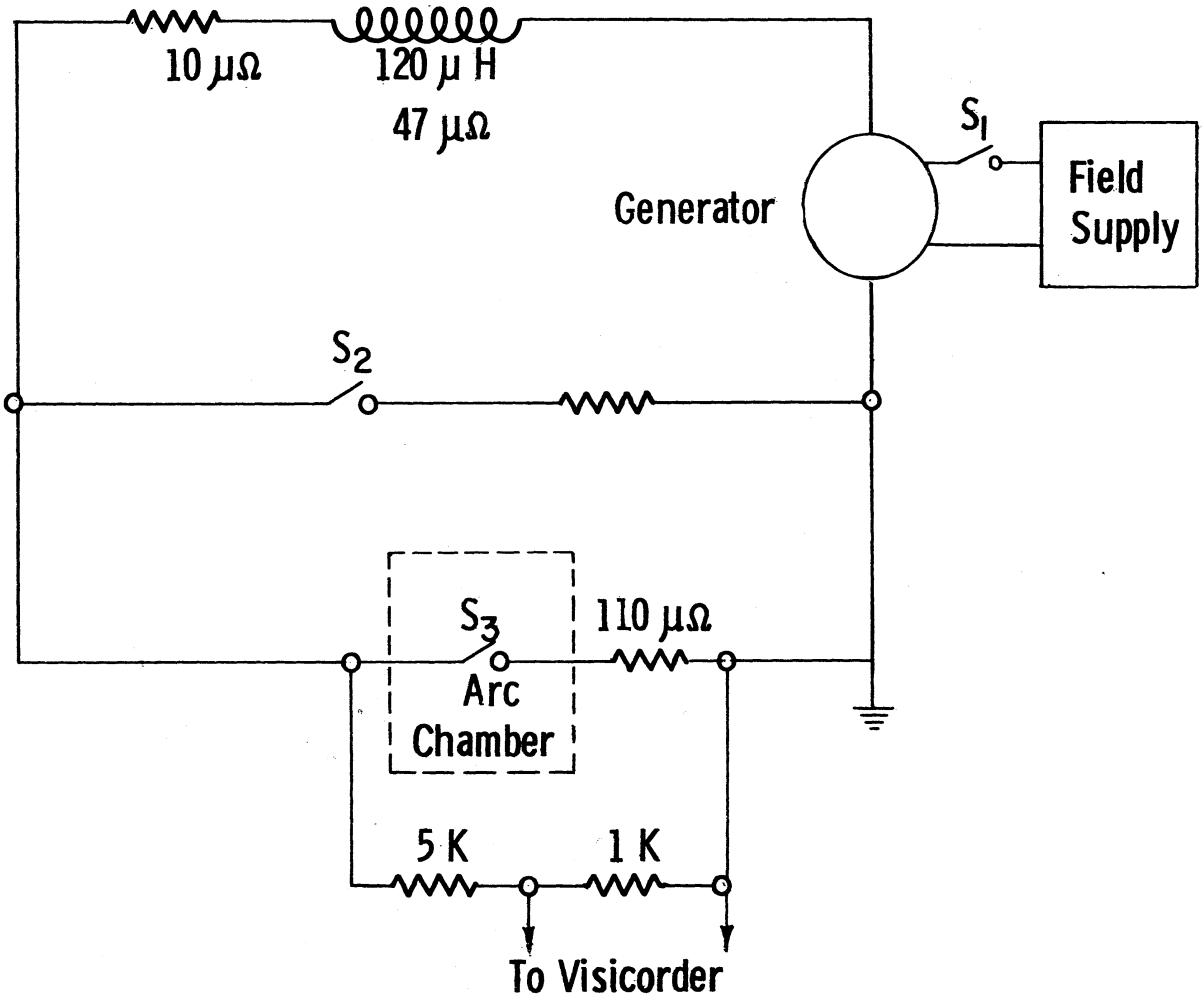


Figure 4. Circuit Diagram for the Hotshot Energy Supply

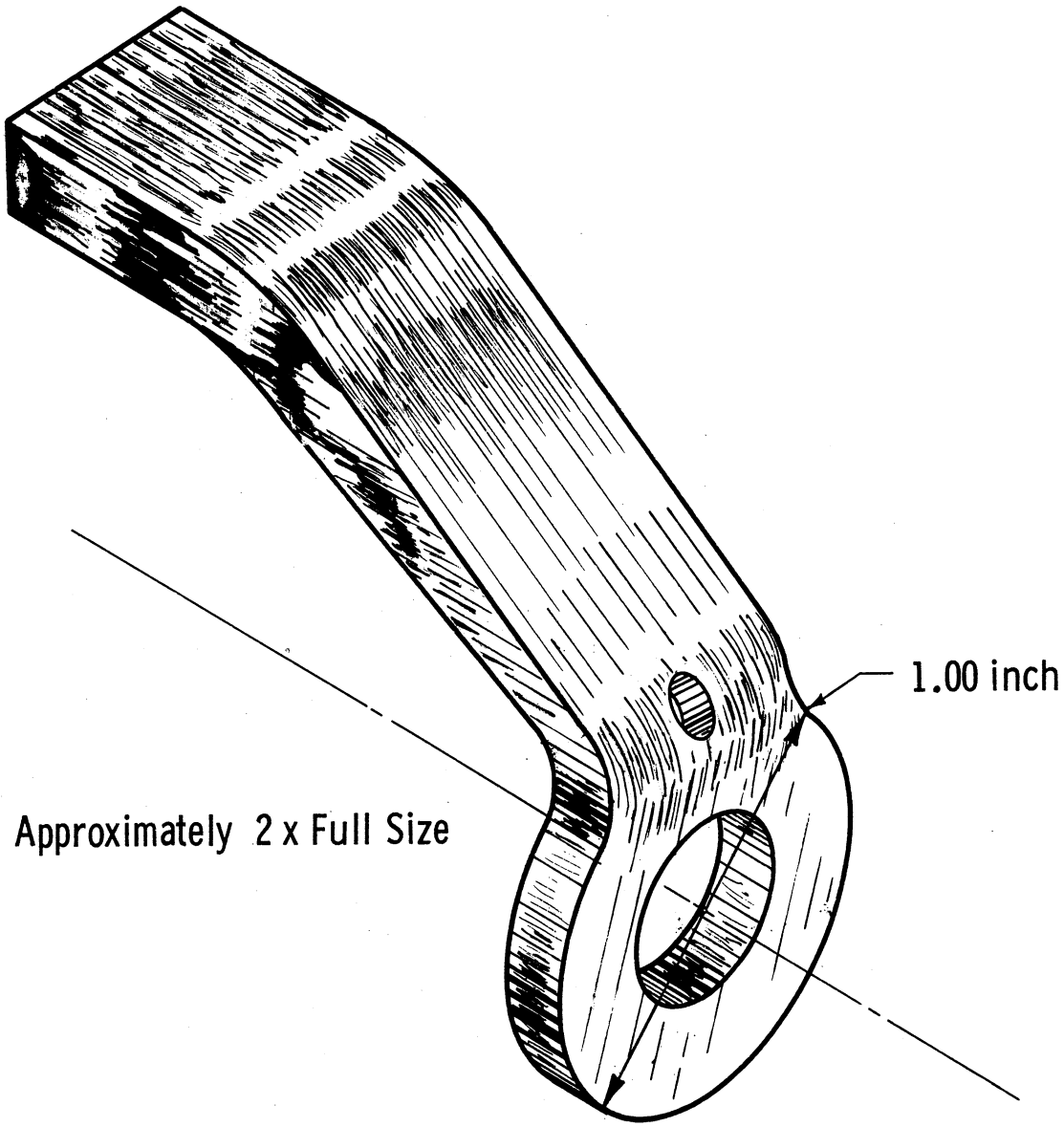


Figure 5. Zinc Fuse Configuration

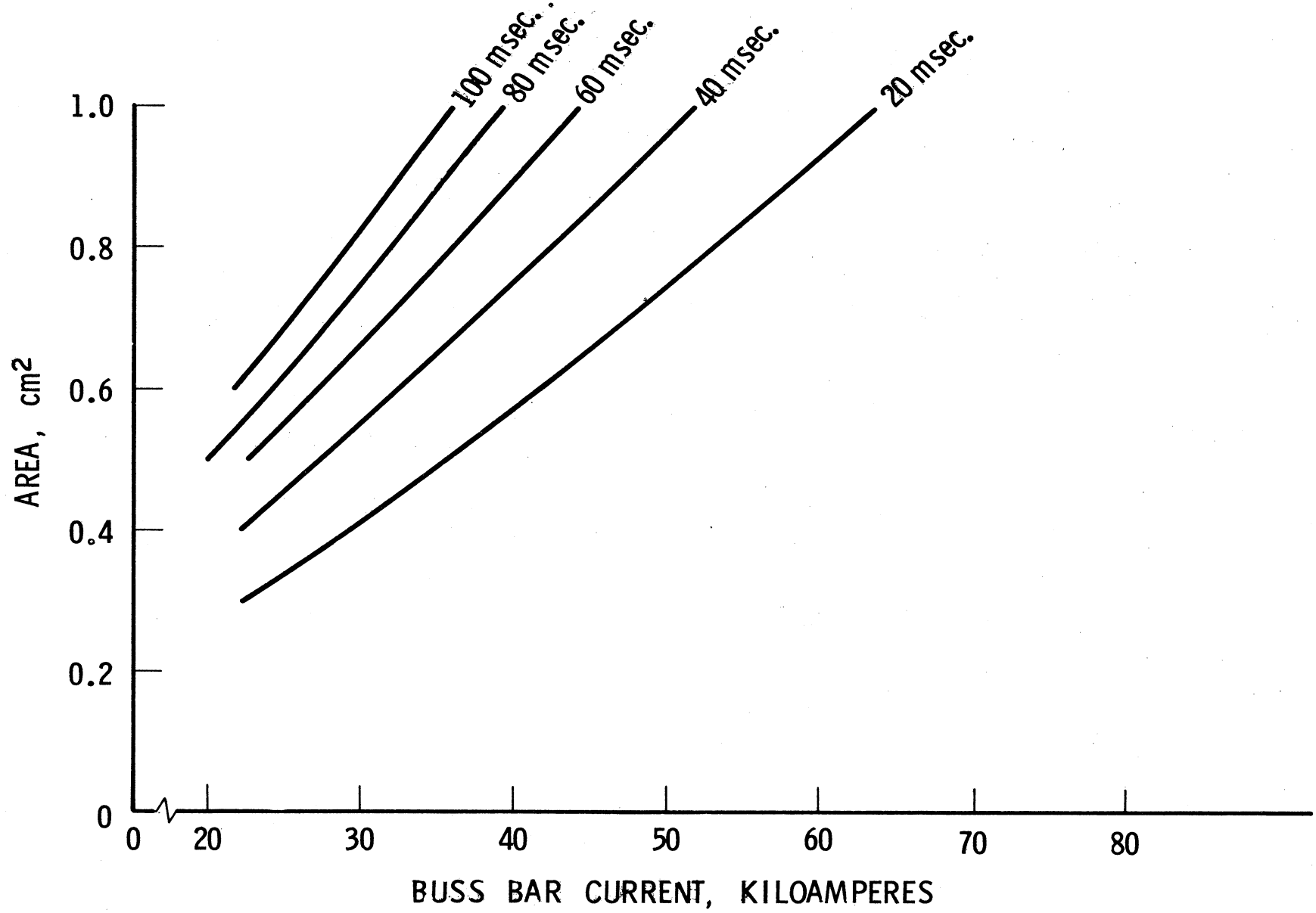


Figure 6. Fuse Cross Section Area vs Buss Bar Current for Various Fuse Delay Times

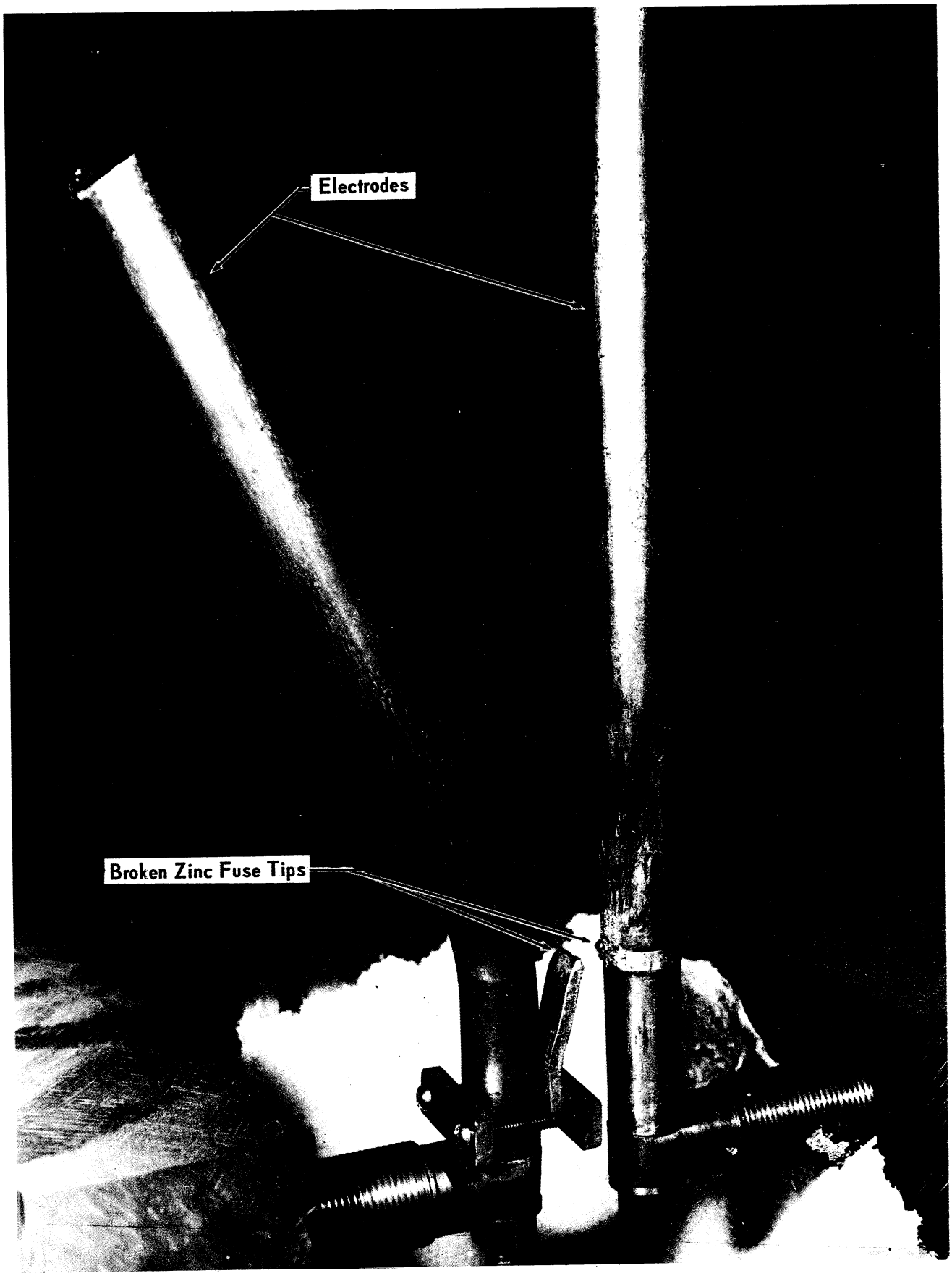


Figure 7. External Electrodes After Zinc Fuse Test

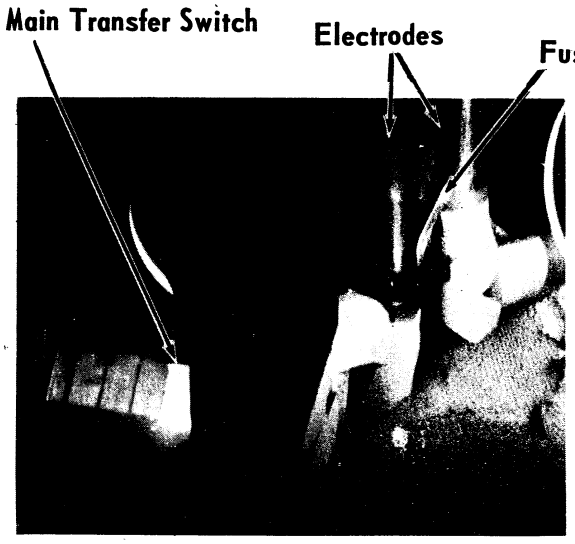


a.) Prior to Run

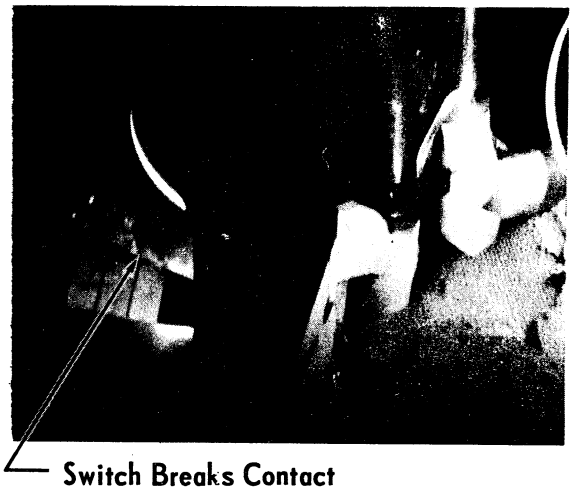


b.) t = 0


c.) t = 40 milliseconds

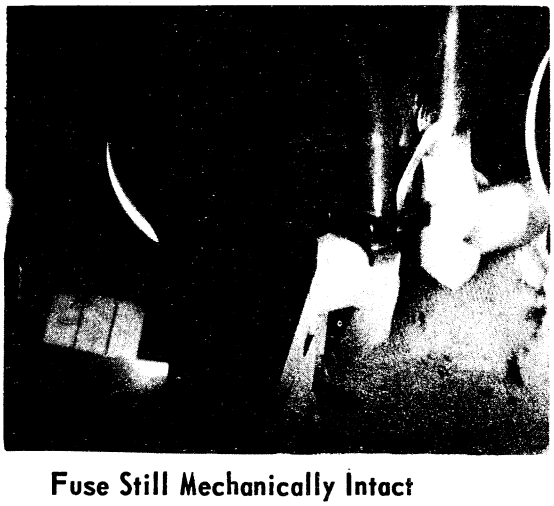


d.) t = 45 milliseconds

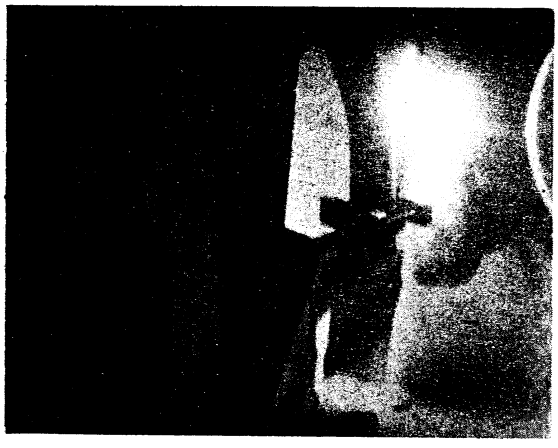


e.) t = 48 milliseconds

f.) After Run

Figure 8. Fuse Test Sequence

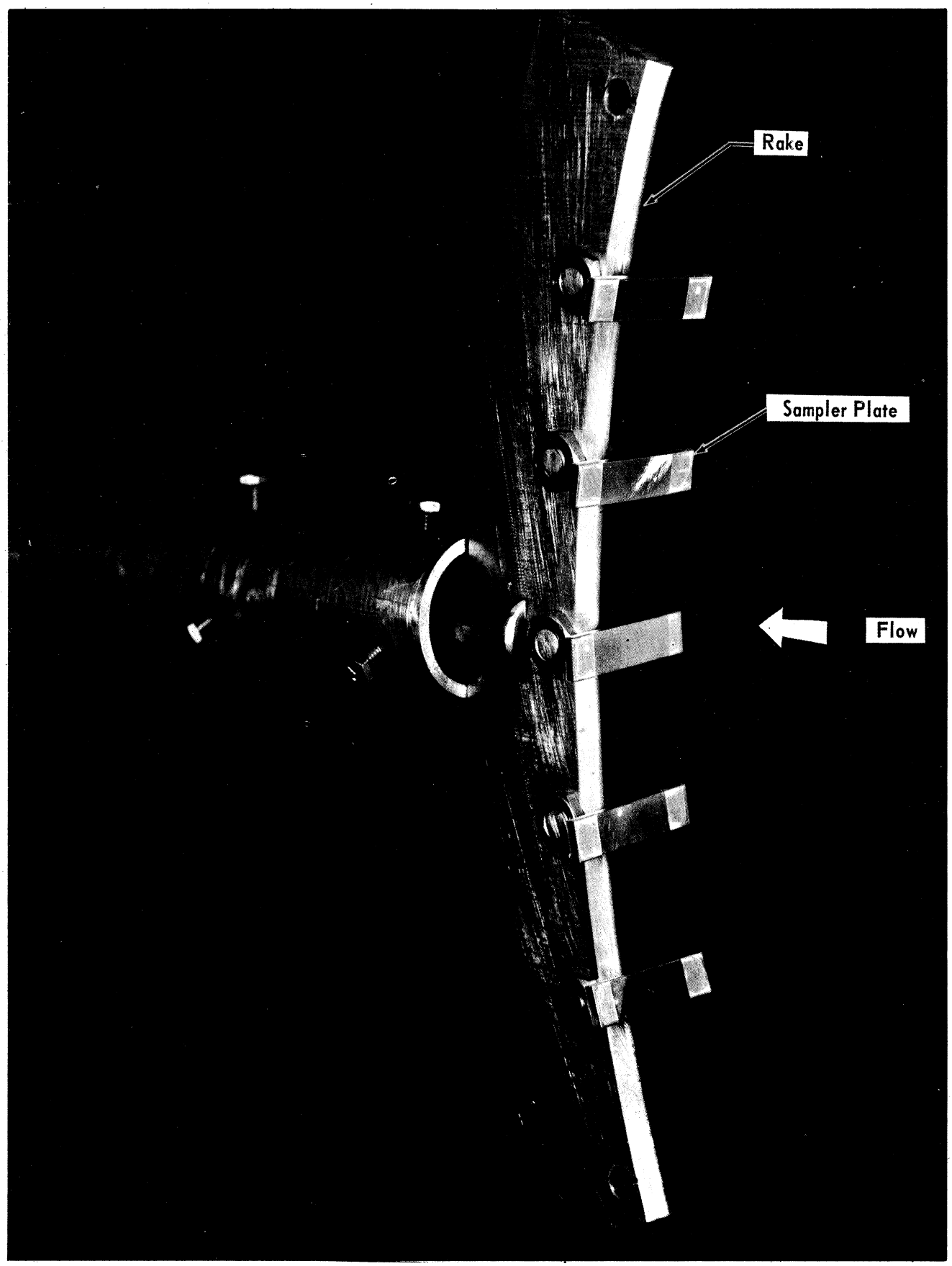


Figure 9. Photograph of Sampler Rake

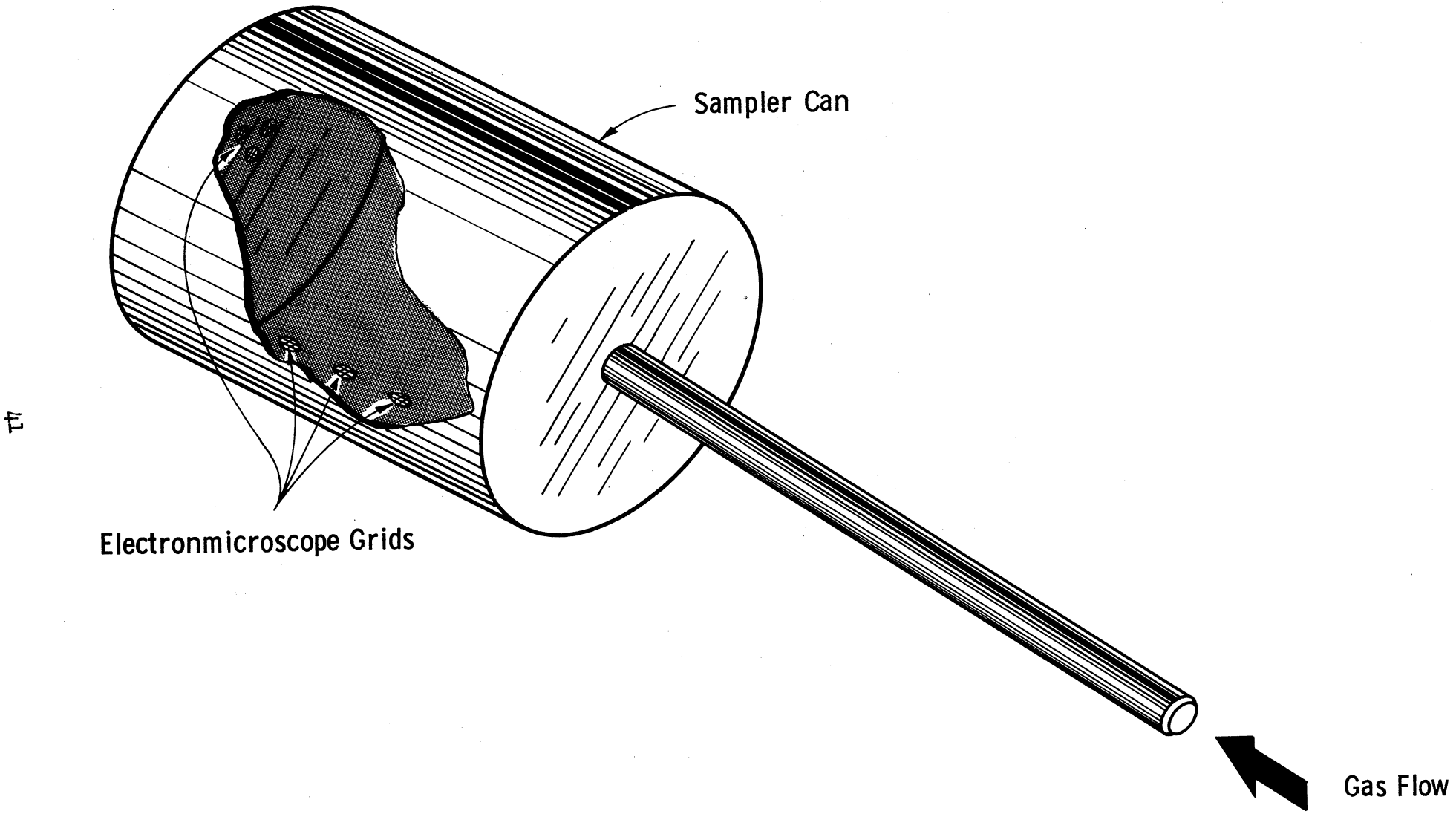


Figure 10. Particle Sampling Can

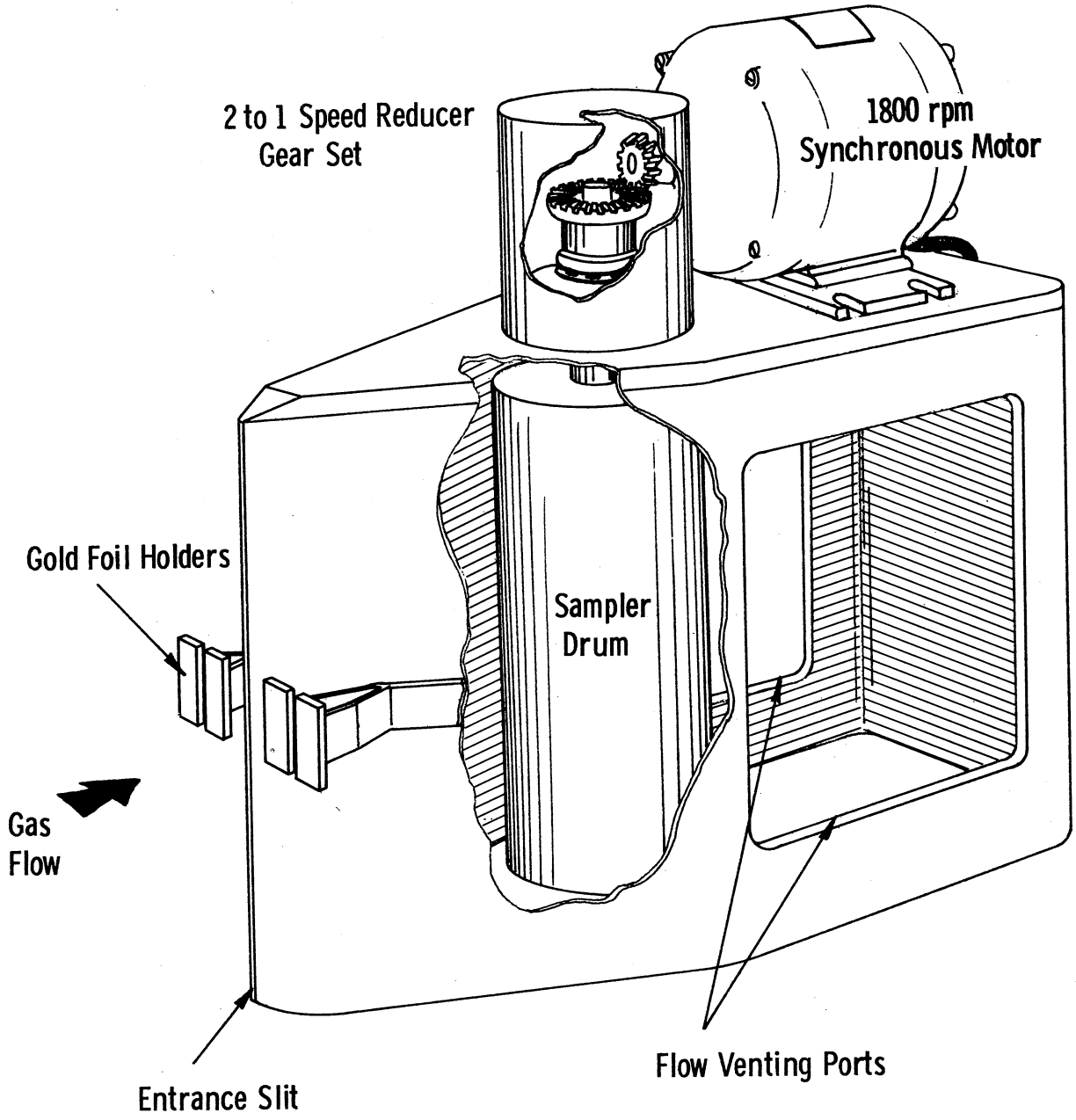


Figure 11. Sampler Drum and Housing with Gold Foil Holders

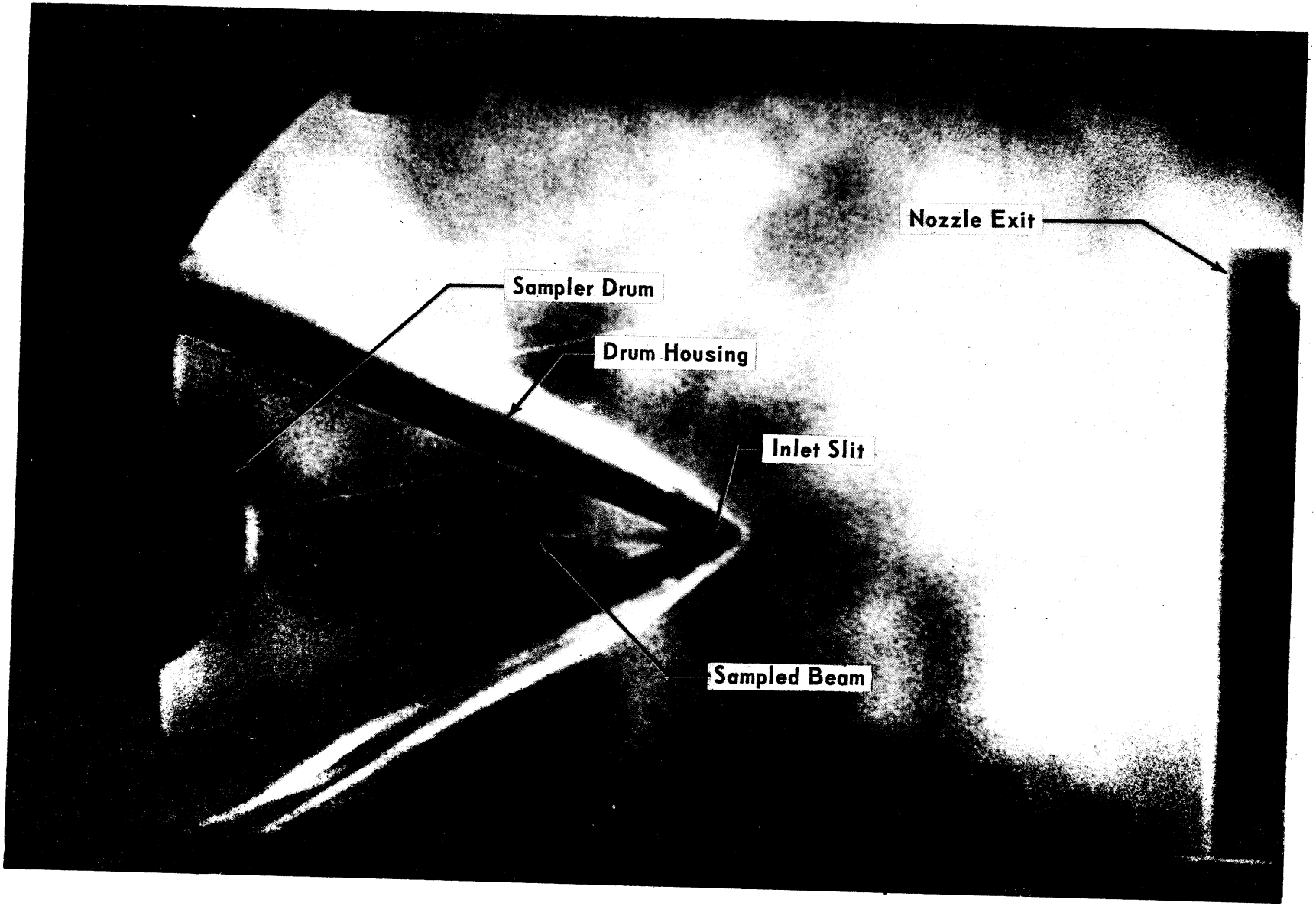


Figure 12. Schlieren Photograph of Sampler Drum Check Run

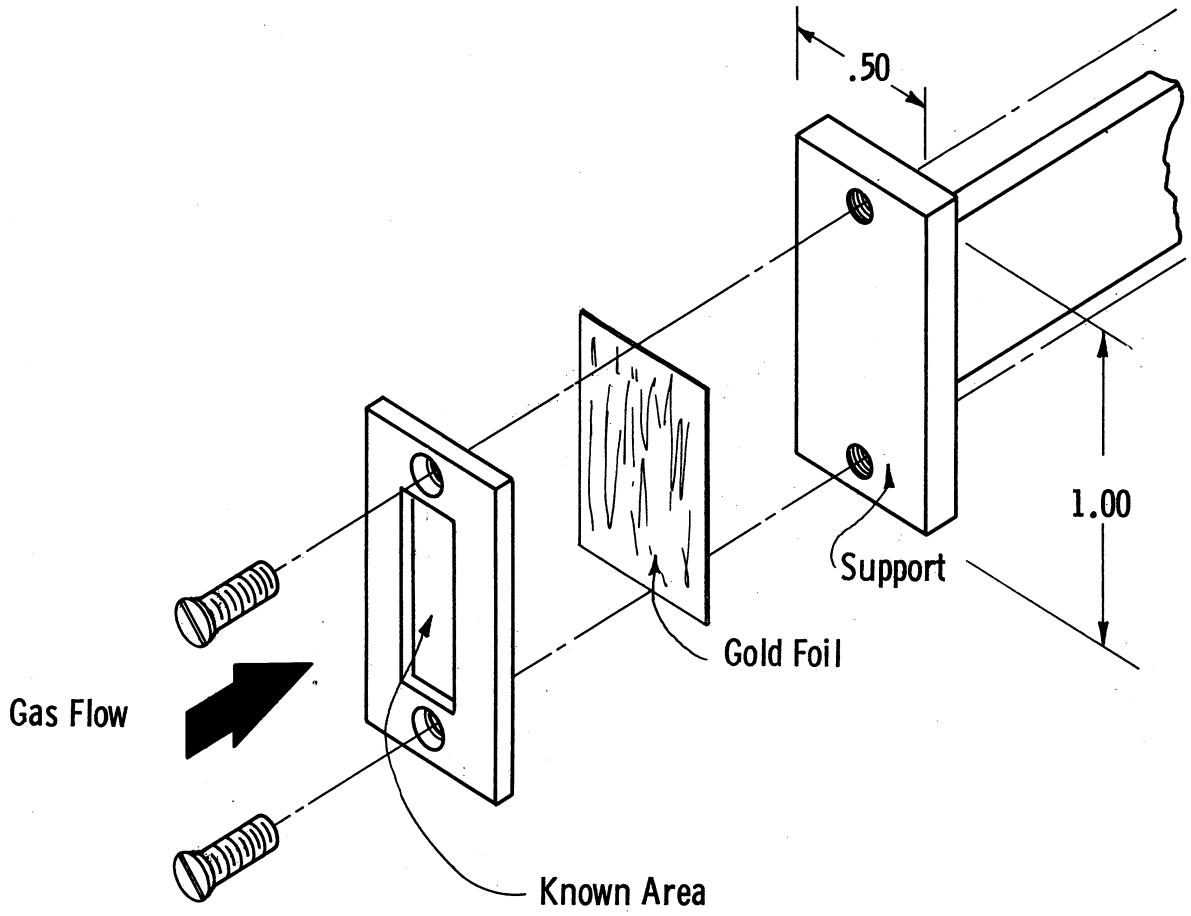


Figure 13. Exploded View of Gold Foil Holder

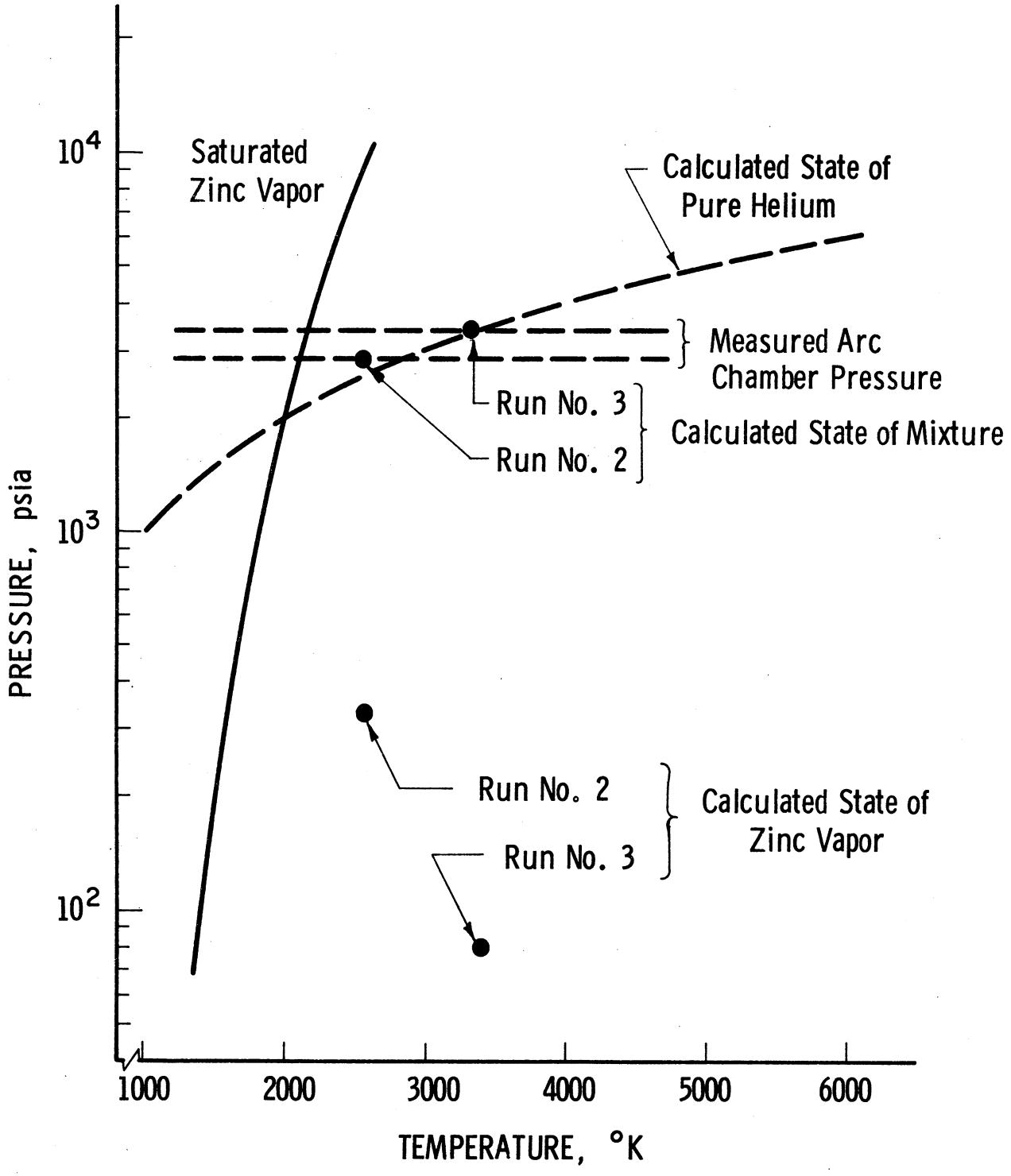


Figure 14. Calculated State of Zinc Vapor in the Arc Chamber

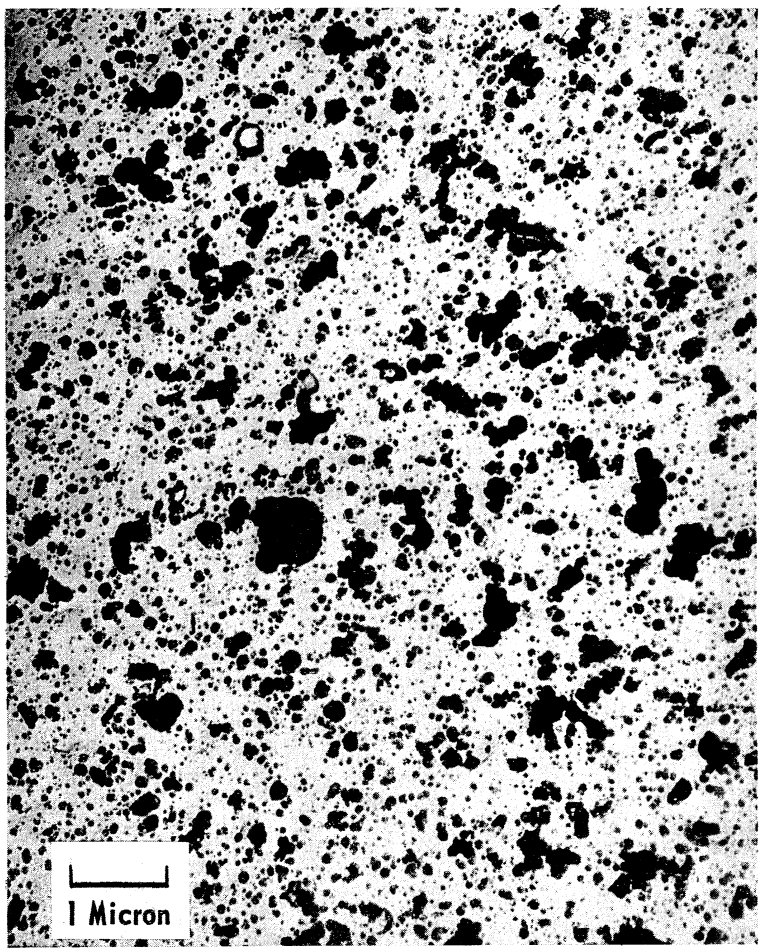


Figure 15. Electronmicroscopic Photograph of Particles Collected During Run No. 1

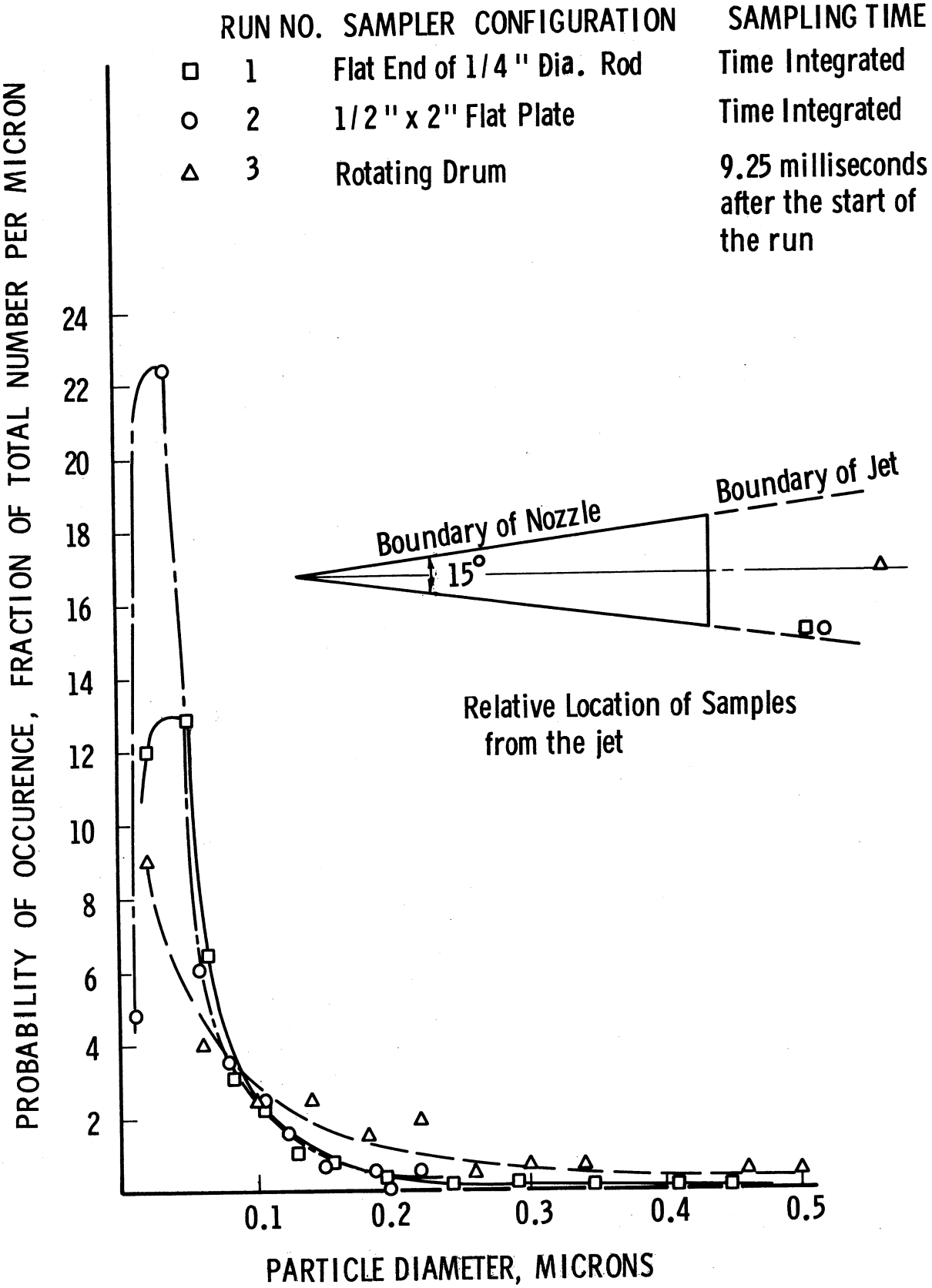


Figure 16. Normalized Distribution of Particle Diameters

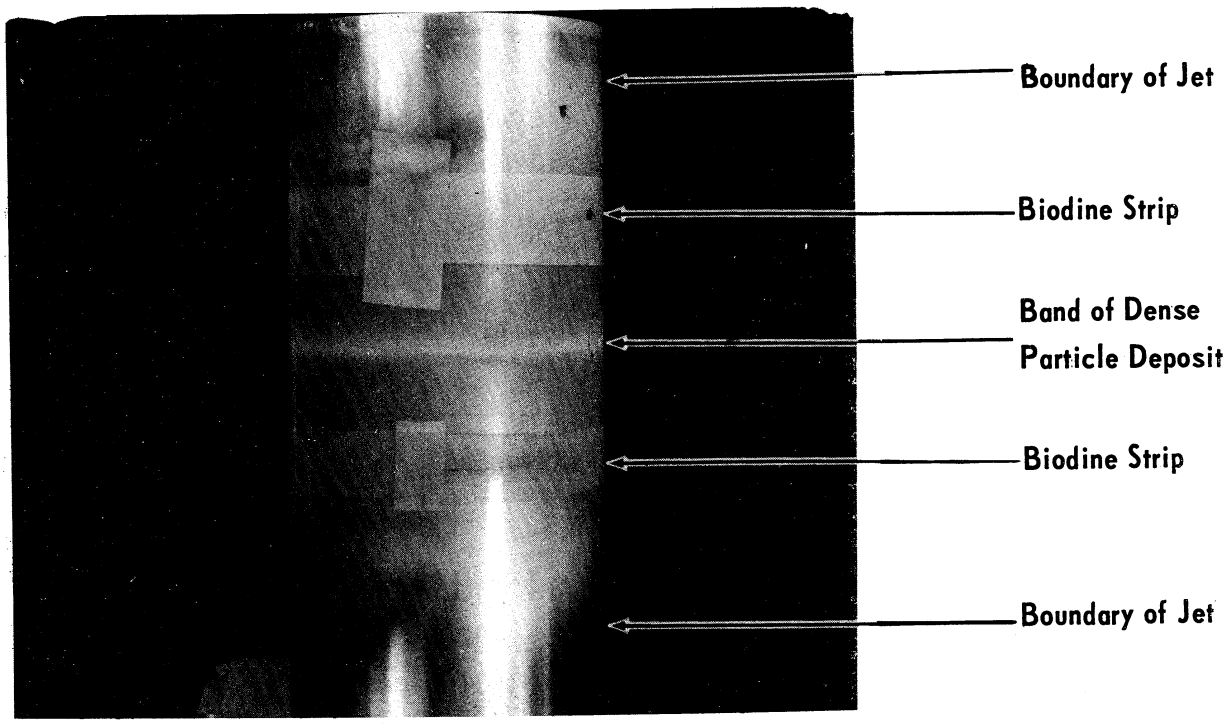


Figure 17. Photograph of Sampler Drum After Run No. 3

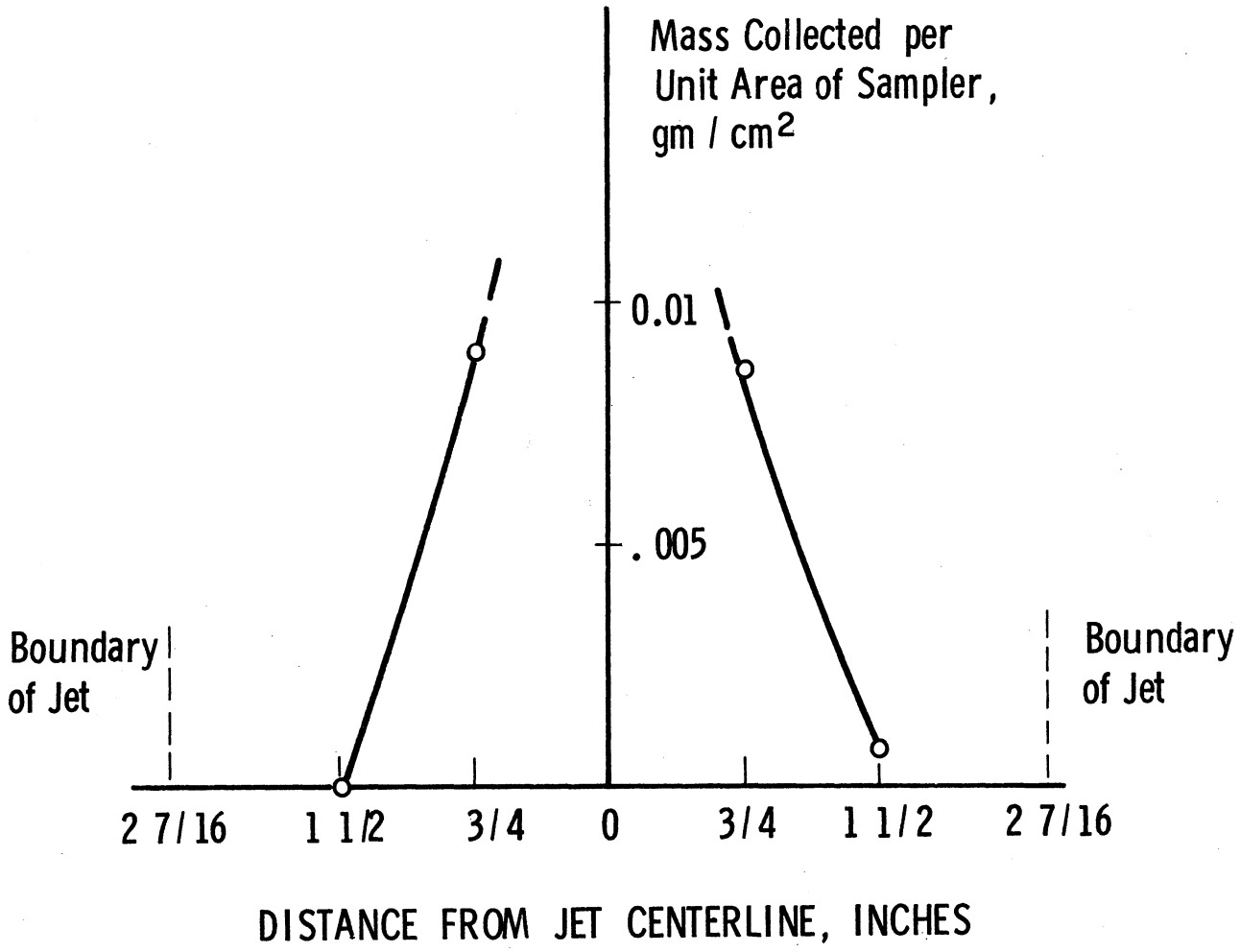


Figure 18. Integrated Area Mass Density of Particles Collected During Run No. 3

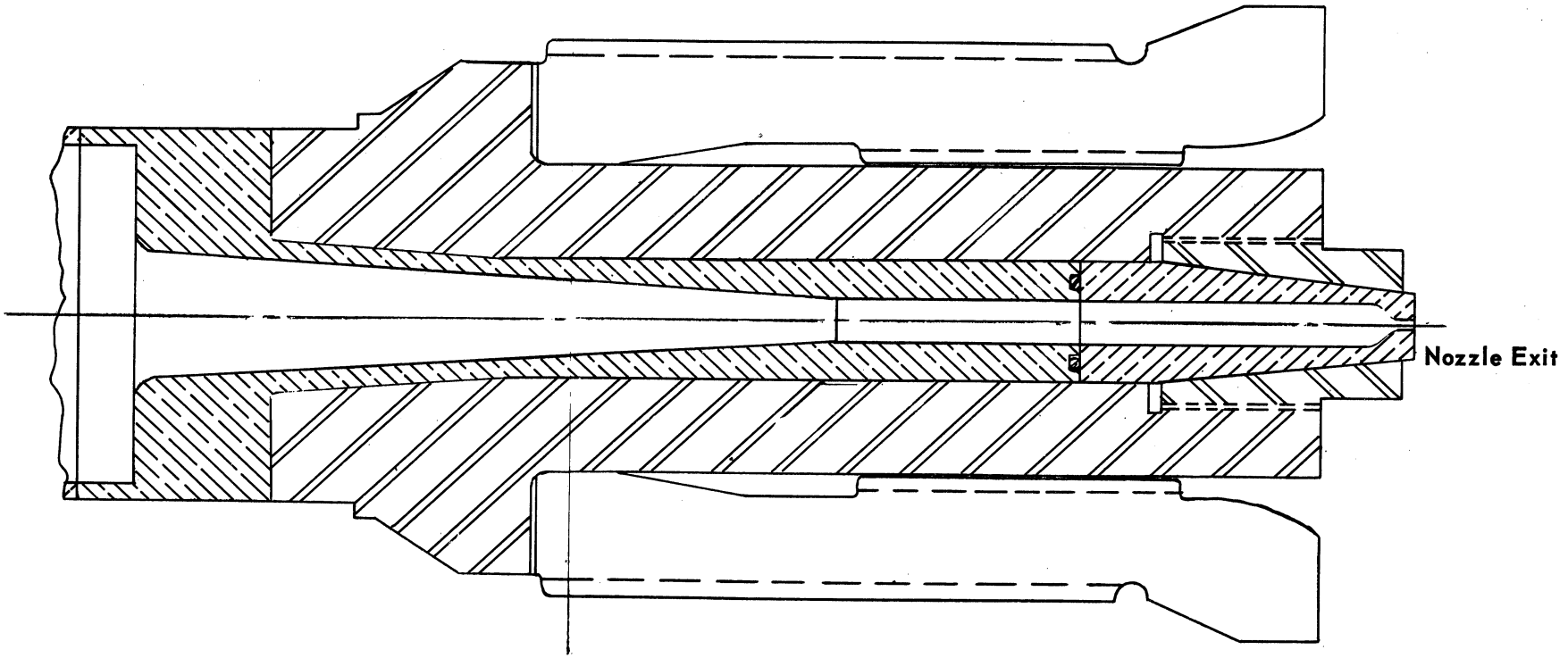


Figure 19. Arc Chamber Nozzle Configuration for Free Jet Condensation Studies

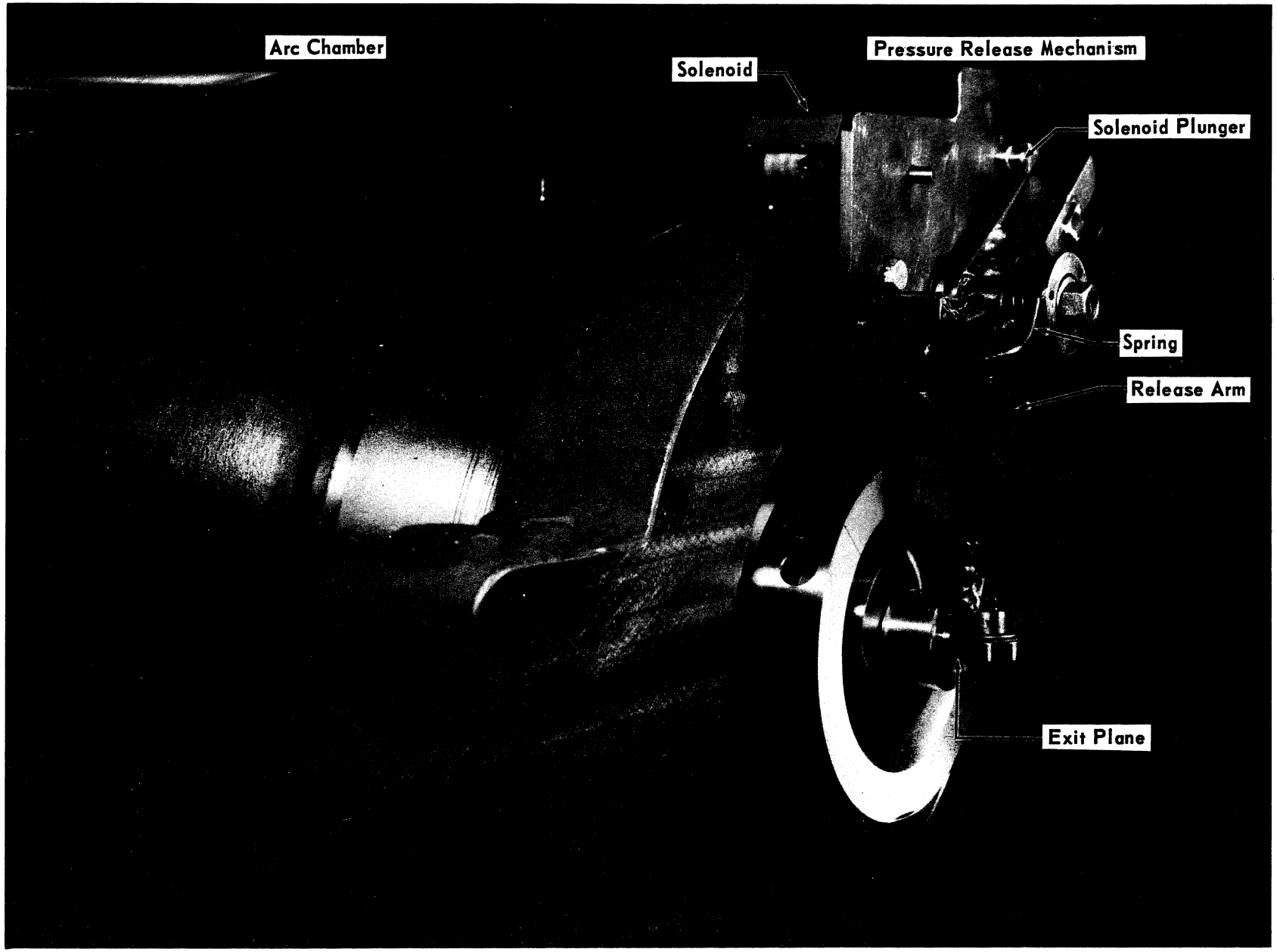


Figure 20. "Mark II" Pressure Release Mechanism

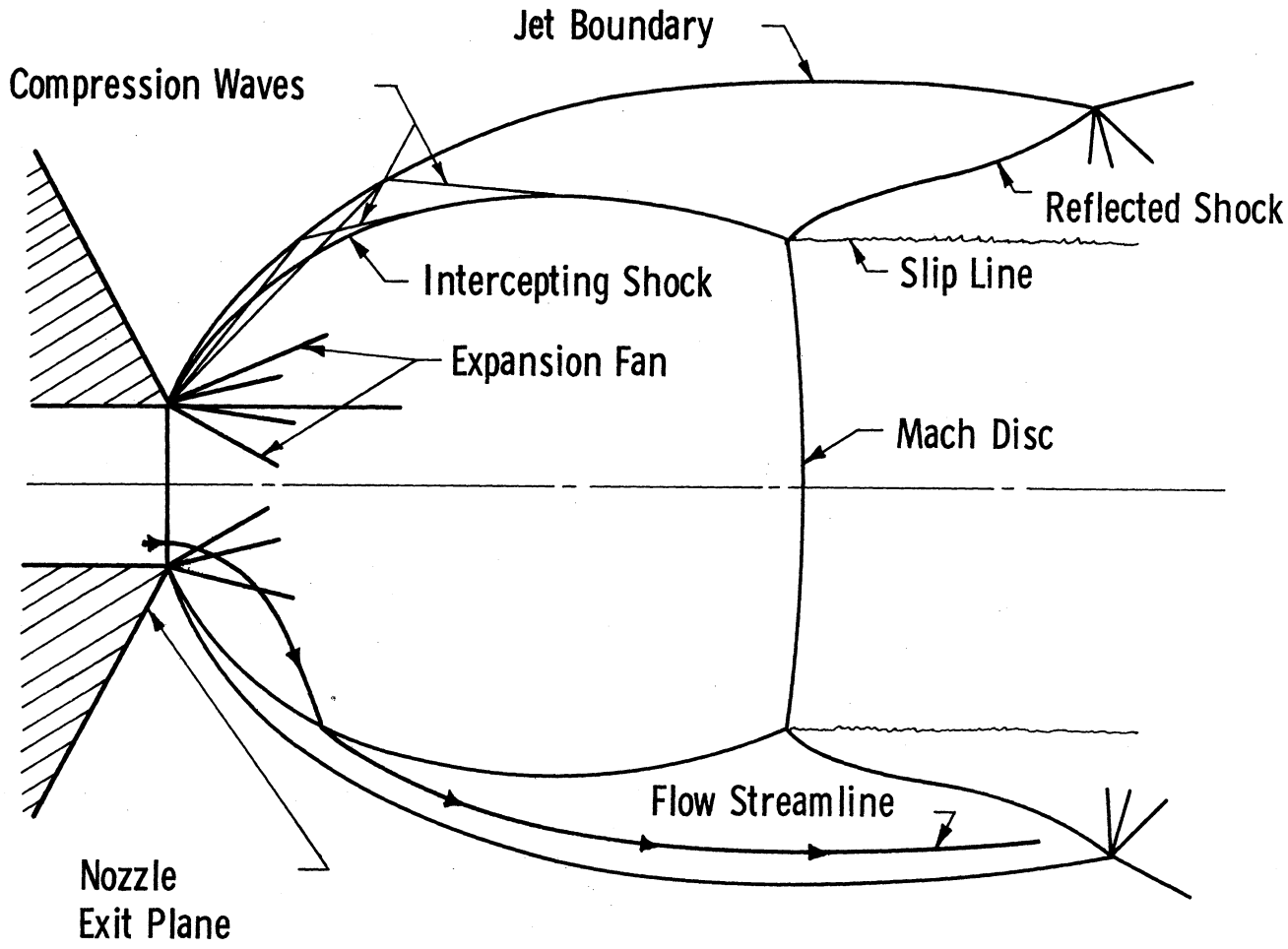


Figure 21. Structure of the Underexpanded Jet

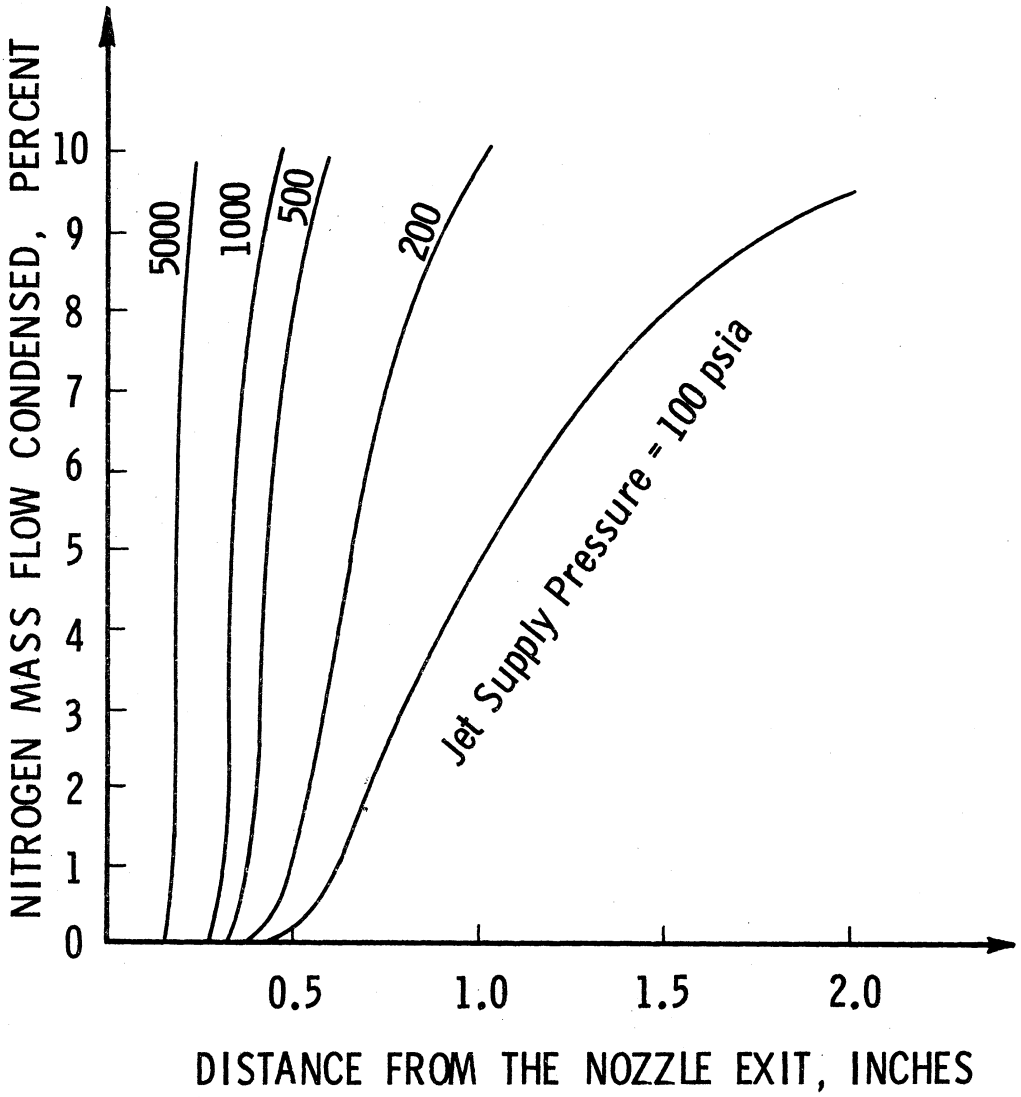


Figure 22. Calculated Condensation History in an Underexpanded Nitrogen Jet

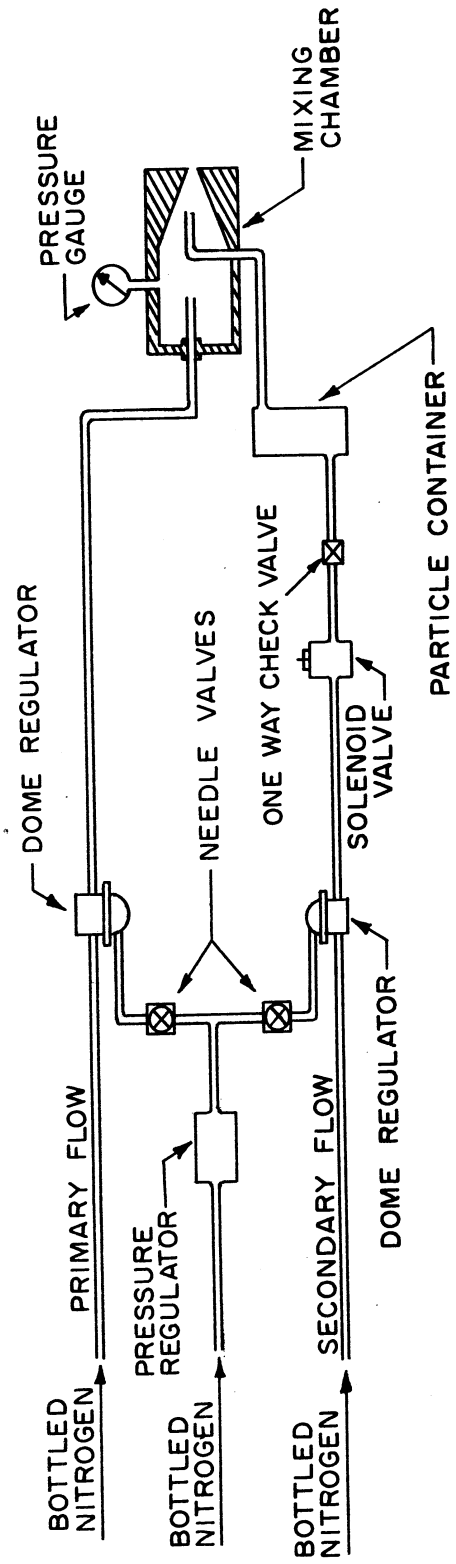


Figure 23. Flow Diagram of Particle Seeding Apparatus

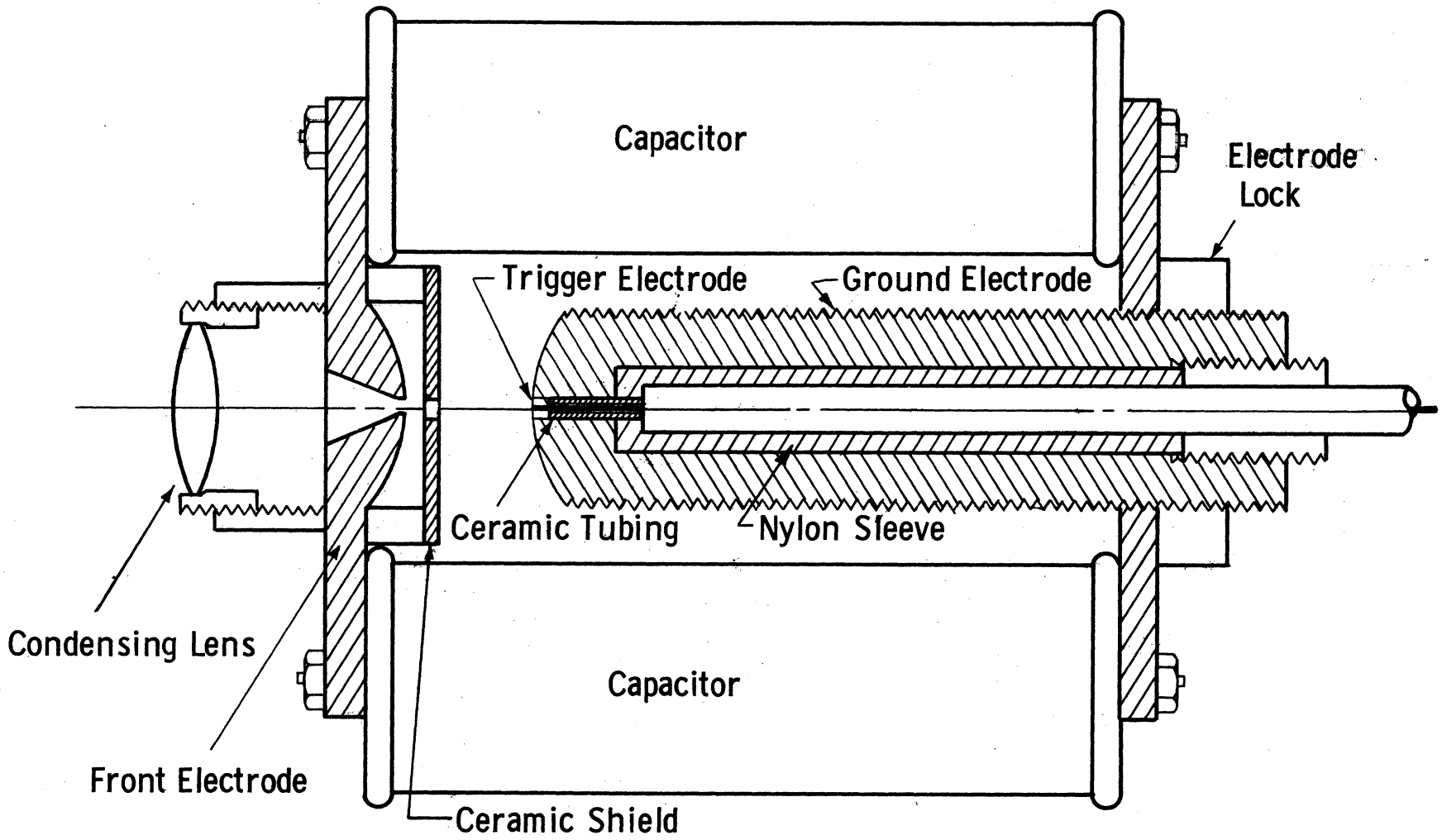


Figure 24. Assembly Sketch of 24-Joule Spark Light Source

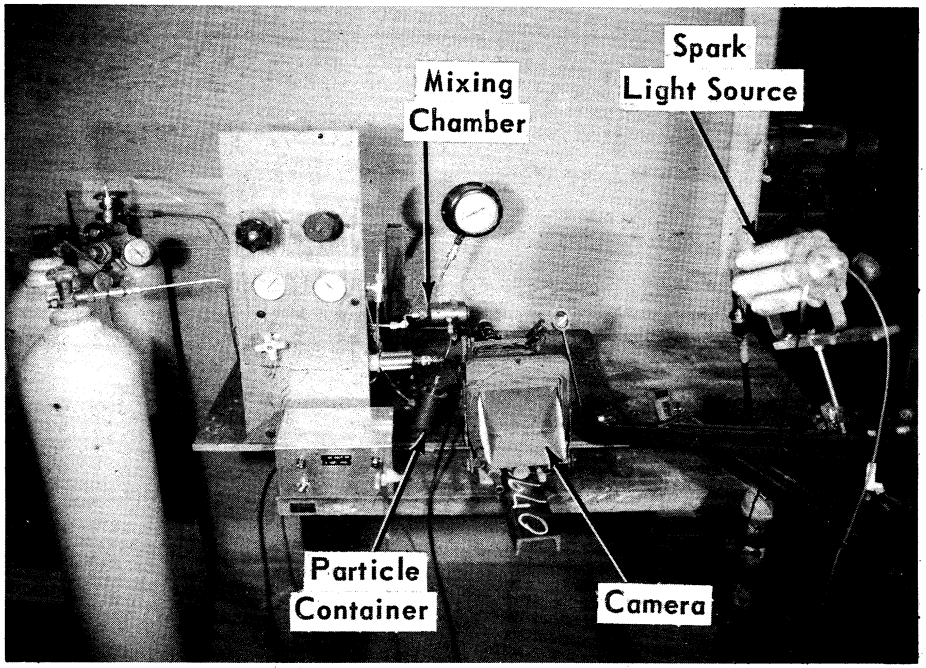


Figure 25. Photograph of Experimental Set-Up for Seeded Jet Photography Studies

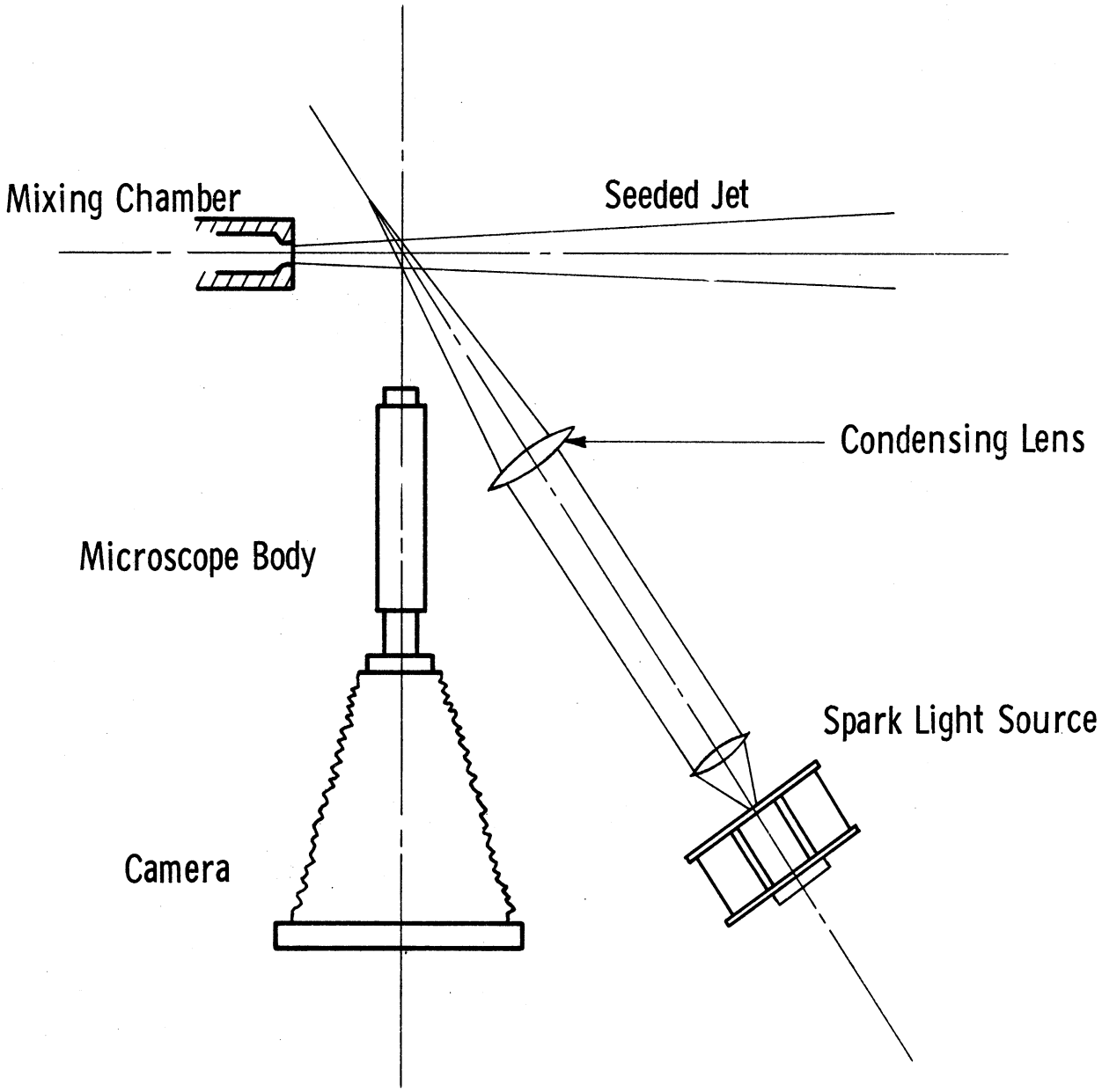


Figure 26. Arrangement of Camera and Spark Source for Seeded Jet Photography Studies

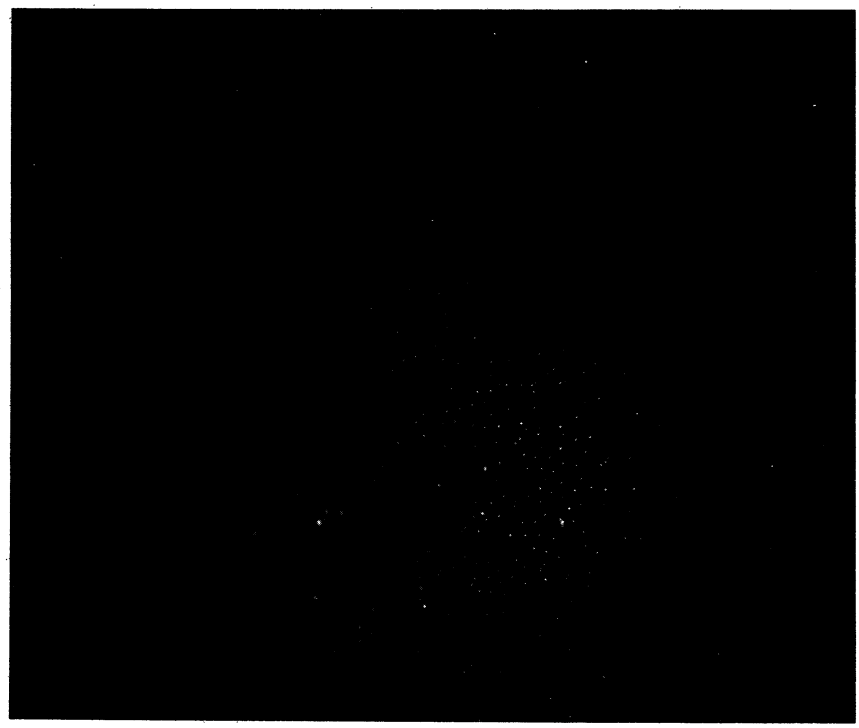

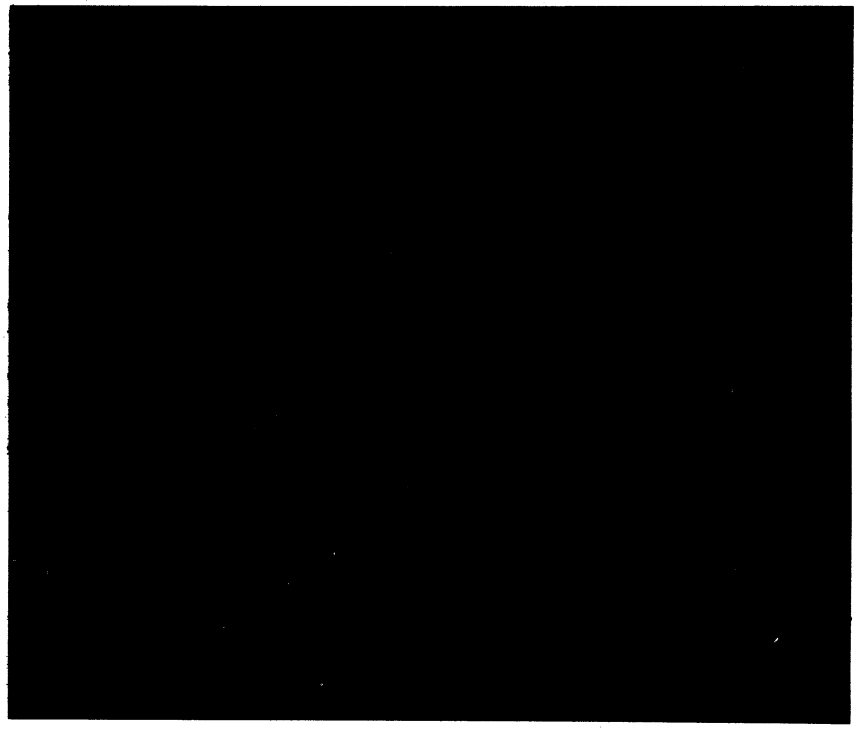

Figure 27. Photomicrographs of Stationary and Moving Black Glass Beads: 74 to 150 micron Bead Diameter, 24x Magnification

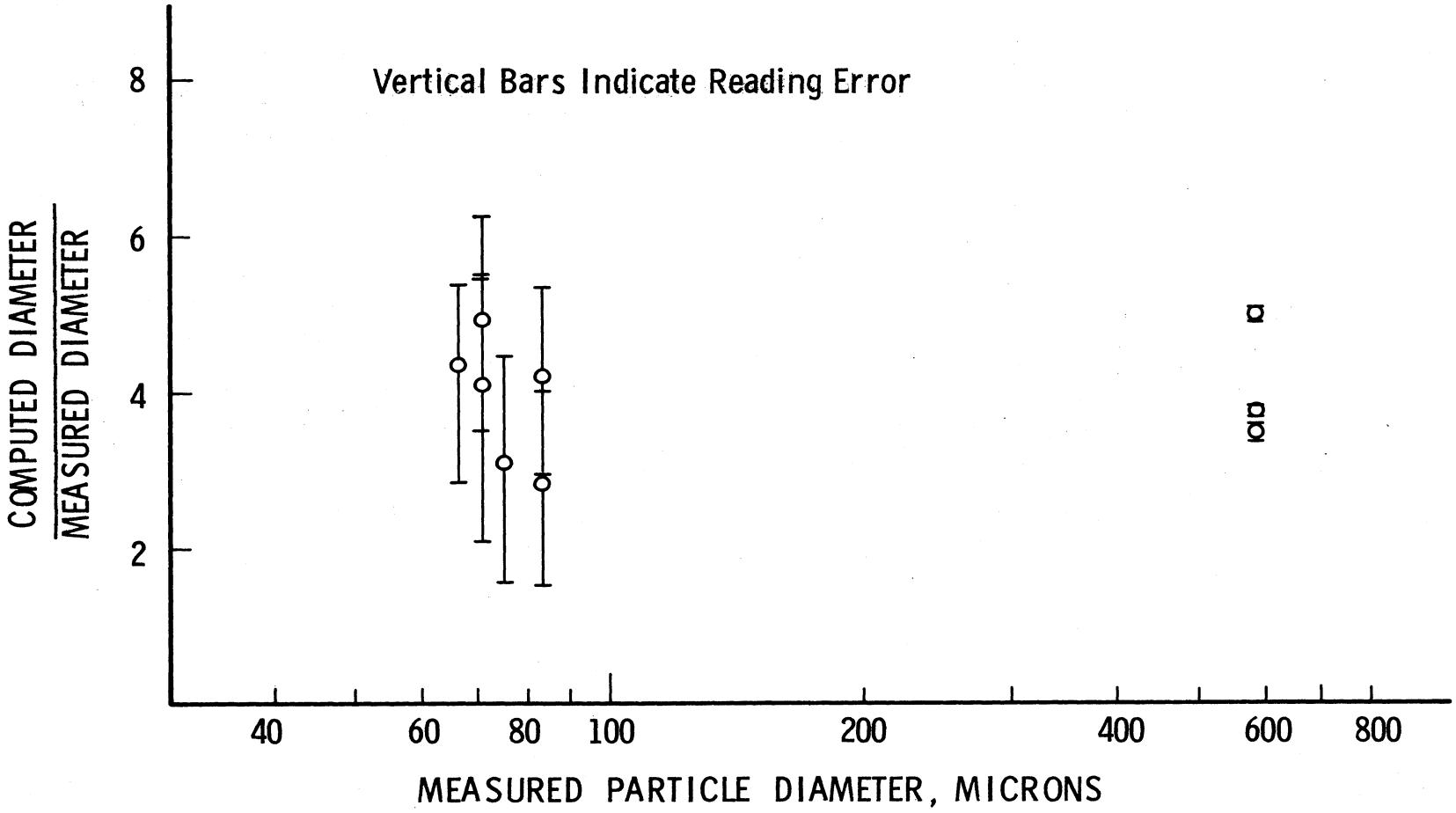


Figure 28. Results of Size Determinations from Stationary Photographs of Black Glass Beads

## APPENDIX A

## CALCULATION OF ENERGY REQUIREMENTS FOR GENERATING METAL-GAS MIXTURES

P. L. Lu

The total energy required to heat a given mixture of metal and thermally perfect carrier gas from an initial condition (where the metal is solid) to some final state (where the metal is vaporized) can be computed from their equilibrium thermodynamic relationships. The partial energy required to heat the carrier gas can be easily computed as the product of the temperature rise, the specific heat, and the mass of the gas. To calculate the energy required for the metal, the heating path must be considered. Two bounding paths may be assumed. One assumes that the metal vaporizes at the saturation temperature corresponding to the initial carrier gas pressure. The other assumes the vaporization of the metal takes place at the saturation temperature corresponding to the final mixture pressure. Once a vaporization temperature is selected, the required energy can be computed by the following expression:

$$\Delta E_m = C_{sm} (T_{sat} - T_i) + E_F + E_v + C_{vm} (T_F - T_{sat}) \qquad \text{(A-1)}$$

where $\Delta E_m$ = energy increment of the metal (Joules/lb)

$C_{sm}$ = specific heat of the metal in the solid state (Joules/lb $^{o}$K)

$T_{sat}$ = saturation temperature of the metal ($^{o}$K)

$T_i$ = initial temperature of the metal ($^{o}$K)

$E_F$ = energy of fusion of the metal (Joules/lb)

$E_v$ = energy of vaporization of the metal (Joules/lb)

$C_{vm}$ = specific heat of the metal in the vapor state (Joules/lb $^{o}$K)

$T_F$ = final temperature of the metal ($^{o}$K)

The energies calculated on the basis of the two bounding paths are very close; the differences are less than 1 %.

Knowing the mass ratio and partial energies of the gas and metal, the total energy per unit mass of the mixture can be expressed as follows:

$$\Delta E_{tot} = \frac{\Delta E_m \cdot M_m + \Delta E_G \cdot M_G}{M_m + M_G}$$

$$= \left( \Delta E_m \cdot \frac{M_m}{M_G} + \Delta E_G \right) \frac{M_G}{M_T} \qquad \text{(A-2)}$$

where $\Delta E_{tot}$ = total energy increment of the metal and gas mixture (Joule/lb)

$M_m$ = mass of the metal (lb)

$\Delta E_G$ = energy increment of the carrier gas (Joule/lb)

$M_G$ = mass of the carrier gas (lb)

$M_T$ = mass of the metal and gas mixture (lb)

Calculations based on Eq. (A-2) will yield the energy requirement per unit mass of mixture as a function of mixture temperature and mass ratio. However, for application purposes it is more convenient to express the energy requirement in terms of the final pressure and the volume of the mixture. This is done as follows:

$$\Delta E'_{tot} = \Delta E_{tot} \cdot \frac{1}{R_{tot} T_F} \qquad \text{(A-3)}$$

where $\Delta E'_{tot}$ = total energy increment of the metal and gas mixture (Joule/psi-in$^3$)

$R_{tot}$ = gas constant of the metal and gas mixture (in-lb/lb mole $^oK$)

As an example of results obtained from these calculations, the total energy required for a zinc-in-helium mixture is shown in Fig. A-1 as a function of mixture temperature for various values of mass fraction of zinc. The increase in

$\Delta E'_{tot'}$ with decreasing temperature, for the larger zinc mass ratios is due to the value of the vaporization energy, which is essentially fixed independent of the final mixture temperature and which is much larger than either of the energies required to heat the metal to its vaporization temperature and to superheat the metal vapor.

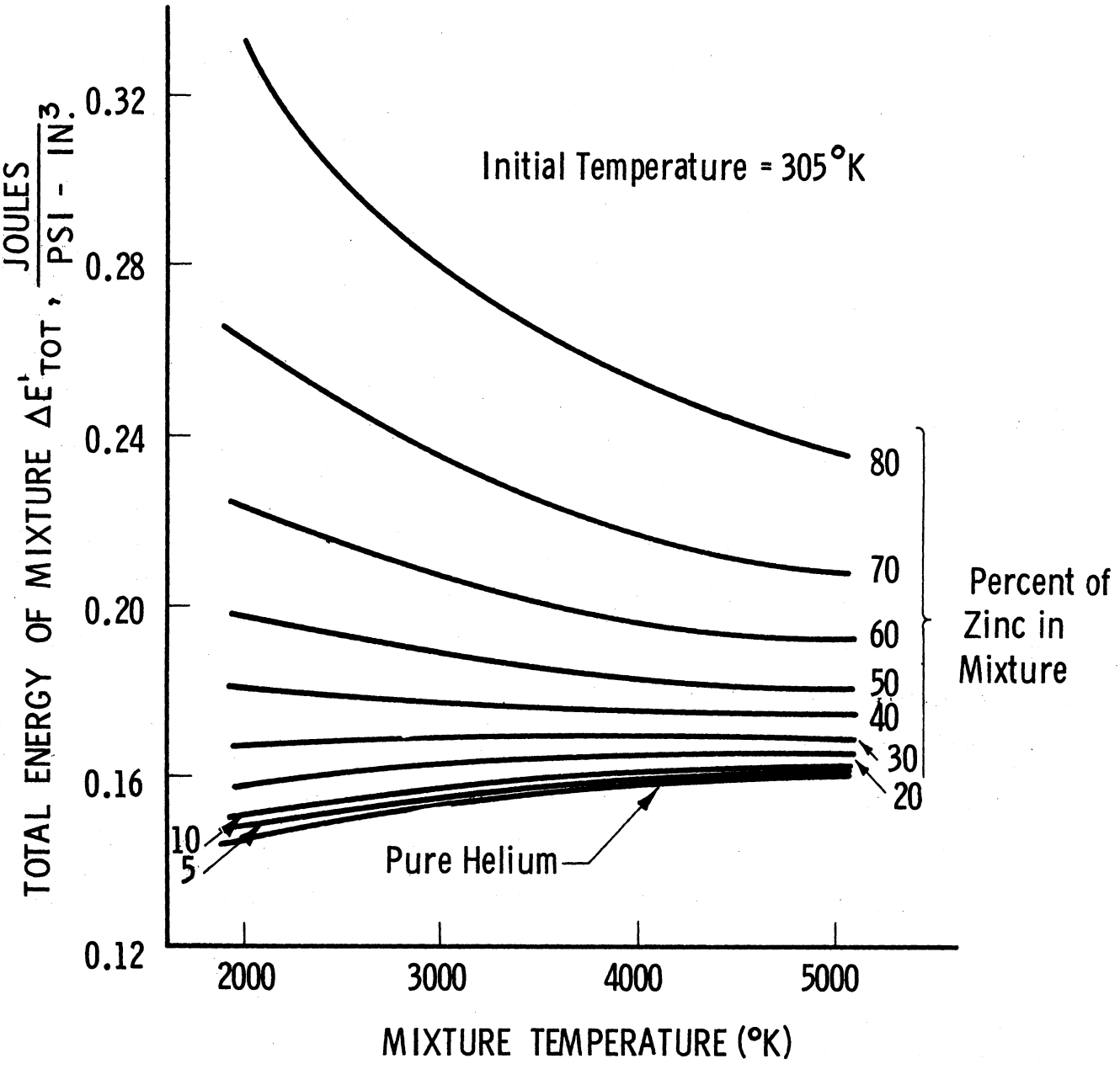


Figure A-1. Energy Requirement for Zn-He Mixture

## APPENDIX B

## A DISCUSSION OF LIGHT SCATTERING THEORY

K. R. Sivier

The interaction of electromagnetic radiation with a particle of arbitrary geometry and composition is characterized, in general, by scattering and absorption of energy by the particle. A general solution, to this very difficult problem, does not exist. However, a solution for a particularily useful special case does exist; i. e., the Mie solution (Ref. B-1)[1] for the interaction of a plane electromagnetic wave with a homogeneous sphere suspended in an infinite, homogeneous, and isotropic medium. This solution is of particular importance to the present studies, since the condensed particles are expected to be essentially spherical.

A simplified representation of the interaction process is presented in Fig. B-1. The incident radiation has an energy flux intensity of $I_o$. In general, the interaction results in absorption and scattering of this incident energy. The sum of these two effects is called the extinction and is evidenced by a decrease in the intensity of the transmitted energy flux I, as compared to $I_o$. The absorbed energy flux, $E_a$, appears as internal energy of the particles. In the case of a homogeneous and isotropic scatterer, illuminated by unpolarized radiation of intensity $I_o$, the intensity of the radiation scattered at the angle $\theta$ is given by the relation (e. g., see Ref. B-7)

---

(1) An abbreviated derivation of the Mie solution is presented in Ref. B-2. Detailed discussions and excellent reference lists are given in Refs. B-3, B-4, and B-5. Reference B-6 also presents a brief discussion of the theory. In addition, scattering from non-spherical particles is discussed in Refs. B-3 and B-4, and Ref. B-4 presents some material on non-homogeneous scatterers.

$$I_\theta = \frac{\lambda^2 I_o}{8\pi^2 R^2}\left[i_1(\theta) + i_2(\theta)\right]$$

$$= \frac{\lambda^2 I_o}{8\pi^2 R^2} i_T(\theta) \quad , \tag{B-1}$$

where $\lambda$ = wavelength of the incident radiation,

$\theta$ = scattering angle (Fig. B-1), the angle between the direction vectors of $I_o$ and $I_\theta$,

R = radial distance from the particle to the point of observation (R must be much greater than both $\lambda$ and the dimensions of the scattering particle),

$i_T(\theta) = i_1(\theta) + i_2(\theta)$

= a function proportional to the total intensity of radiation scattered from an unpolarized incident beam,

and $i_1(\theta)$, $i_2(\theta)$ = functions proportional to the intensity of the two incoherent, plane-polarized components of the scattered radiation. $i_1(\theta)$ has its electric vector perpendicular to the plane containing the direction vectors of $I_o$ and $I_\theta$; the electric vector of $i_2(\theta)$ is parallel to this plane.

(It is implicitly assumed here that $I_\theta$ is of the same wavelength as $I_o$; effects leading to wavelength shifts are excluded.) Because of the axial symmetry of the scattering pattern, the total flux of scattered energy can be written simply as the integral of Eq. (B-1)

$$E_s = 2\pi R^2 \int_0^\pi I_\theta \sin\theta \, d\theta$$

$$= \frac{\lambda^2 I_o}{4\pi} \int_0^\pi i_T(\theta) \sin\theta \, d\theta \tag{B-2}$$

It is convenient, in making use of the scattering theory, to deal with scattering and absorption coefficients. Thus,

$$E_s \equiv k_s \pi r^2 I_o \quad , \qquad E_a \equiv k_a \pi r^2 I_o \quad ,$$

where $k_s$ and $k_a$ are the scattering and absorption coefficients, respectively, and r is the radius of the scattering sphere. If the total extinction coefficient is defined as

$$k \equiv k_s + k_a \quad , \tag{B-3}$$

then the energy removed from the incident beam by a single, spherical scatterer of radius r is

$$E = \pi r^2 k I_o \quad . \tag{B-4}$$

The scattering functions $i_1(\theta)$ and $i_2(\theta)$, in addition to being functions of the scattering angle $\theta$, are functions of the index of refraction, m, of the particle material and of $\alpha$, proportional to the ratio of the particle diameter to the wavelength of the incident light, i. e., $\alpha = 2\pi r/\lambda$. Therefore, for given values of m and $\lambda$, the intensity of the scattered light, $I_\theta$, and the extinction coefficient, k, are both functions of the particle radius. In the general case, this functional relationship is extremely complex. Fortunately, a number of extensive tabulations are available for $i_1(\theta)$, $i_2(\theta)$, $i_T(\theta)$, and k; e. g., see Refs. B-8, B-9, and B-10 for tabulations for non-absorbing materials (real values of m) including metals ($m = \infty$). Additional references to tabulations for non-absorbing materials may be found on pages 167-171 of Ref. B-4. Reference B-11 presents useful approximate formulae for small absorbing and non-absorbing particles, again including the case of $m = \infty$.

In the simplest application of the above theory (developed for the case of a single, isolated scatterer) to the case of a cloud, or aerosol, of scattering

particles, it is assumed that only single scattering occurs. This situation is obtained if each particle is exposed, essentially, to only the original incident radiation. If this situation prevails for a cloud containing N illuminated particles, the energy scattered by the cloud is N times the radiation scattered by one particle and the energy removed from the incident beam is N times that removed by one particle. Reference B-6 suggests that this condition is satisfied when the particles are separated by distances on the order of 100 times their radii. However, Ref. B-4 suggests that the condition is satisfied when the optical depth, $\tau = k\pi r^2 n \ell$ (see Eq. (B-8) below), is less than 0.1.

In view of the single scattering assumption, the total intensity of radiation scattered at angle $\theta$ is then, by Eq. (B-1),

$$\bar{I}_\theta = \frac{\lambda^2 I_o n\bar{V}}{8\pi^2 R^2} i_T(\theta) \qquad \text{(B-5)}$$

where $\bar{V}$ = scattering volume; i.e., the volume, with particle number density n, from which scattered energy is received at the point of observation. Note that in Eq. B-5, the observation distance R must be much greater than the dimensions (say diameter) of the scattering volume $\bar{V}$. In addition, the above holds strictly only for the case of a monodisperse (particles of uniform size) cloud. In the polydisperse case, where particles of p different sizes are present, Eq. B-5 becomes

$$\bar{I}_\theta = \frac{\lambda^2 I_o \bar{V}}{8\pi^2 R^2} \sum_{j=1}^{p} n_j \left[ i_T(\theta) \right]_j \qquad \text{(B-6)}$$

In the case of transmission through a monodisperse cloud, assuming single scattering, the total decrease in intensity of a beam, in traveling a distance $d\ell$ through the cloud, is

$$dI = - k \pi r^2 I n d\ell \tag{B-7}$$

The intensity of the transmitted radiation, after having traveled a distance, $\ell$, through the cloud, then is found directly as

$$\bar{I} = I_o e^{-k\pi r^2 n\ell} = I_o e^{-\tau} \tag{B-8}$$

In the case of the homogeneous polydisperse cloud, (B-8) becomes

$$\bar{I} = I_o \exp\left[ - \pi \ell \sum_{j=1}^{p} k_j r_j^2 n_j \right] \tag{B-9}$$

It should be noted that, in the polydisperse case, measurements of $\bar{I}_\theta$ and $\bar{I}$ can be used to determine (using Eqs. B-5 and B-8) a fictitious monodisperse system with particles having an effective radius, $\bar{r}$, and an effective number density, $\bar{n}$.

It is apparent that several different measurements, or combinations thereof, can be made to obtain information about the size and number density of the scattering particles. The present work has applied the two methods described in Ref. B-6. In the first of these, the ratio of light intensity (at one wavelength) scattered simultaneously at two angles, $\theta_1$ and $\theta_2$, is measured. Applying Eq. (B-5), this ratio can be used to obtain an experimental value for the corresponding scattering function ratio, i. e. ,

$$\frac{i_T(\theta_1)}{i_T(\theta_2)} = \frac{\bar{I}(\theta_1)}{\bar{I}(\theta_2)} \left( \frac{R_1}{R_2} \right)^2 \tag{B-10}$$

The ratio $R_1/R_2$ has been included to account for unequal observation distances. However, the application of Eq. (B-10) assumes that both sensors are receiving light from the same scattering volume $\bar{V}$. In this sense, the scattering function ratio represents a "local" measurement.

Theoretically, for given values of $\theta_1$, $\theta_2$, m, and $\lambda$, the scattering function ratio is a function only of the particle radius r; the dependancy on number density has been divided out. Figure B-2 shows the variation of this ratio with drop diameter d for values of $\theta_1$, $\theta_2$, and $\lambda$ corresponding to the experimental apparatus described in Appendix D. The scattering functions used in constructing this plot were taken from Ref. B-10. This plot, or similar ones, can be used to determine the particle radius corresponding to the measured value of scattering function ratio. Figure B-2 shows that the scattering function ratio becomes multiple-valued for diameters greater than about 0.25 microns and becomes relatively insensitive to diameter for diameters less than about 0.05 microns.

The second method, described in Ref. B-6, involves the measurement of the attenuation of the incident light as it passes through the scattering cloud. In this case, Eq. (B-8) is used in the form

$$\ln I_o - \ln \bar{I} = k\pi r^2 n\ell \qquad \text{(B-11)}$$

where

$$k = k(m, \lambda, r)$$

If $I_o$ and $\bar{I}$ are measured at each of two wavelengths, an extinction coefficient ratio can be determined from the relation

$$\frac{k_1}{k_2} = \frac{k(m, r, \lambda_1)}{k(m, r, \lambda_2)} = \frac{\ln I_{o_1} - \ln \bar{I}_1}{\ln I_{o_2} - \ln \bar{I}_2} \quad . \qquad \text{(B-12)}$$

For given values of m, $\lambda$, and $\lambda_2$, this ratio is a function only of particle radius r. The theoretical variation of $k_1/k_2$, for values of $\lambda_1$ and $\lambda_2$ corresponding to the experimental apparatus, is shown in Fig. B-3. The extinction

coefficients used in this figure were obtained from Ref. B-9. This figure illustrates some limitations to the application of this method. The extinction coefficient ratio is practically independent of drop size for drop diameters below about 0. 1 microns; i. e., for drops small enough so that the scattering essentially follows the Rayleigh law, Ref. B-11. This Rayleigh scattering limitation is somewhat more severe than that shown in Fig. B-2 for the scattering function ratio. Figure B-3 also indicates that the extinction coefficient ratio is multiple-valued for diameters from about 0. 2 to 0. 4 microns. The peculiar variation for this range of diameters is directly due to the k vs $\alpha$ data given in Ref. B-9. For diameters greater than 0. 4 microns, the monotonic decrease shown in Fig. B-3 continues to diameters in excess of 2 microns.

Note that the attenuation measurements yield "integrated" rather than "local" data. Thus, additional problems in data interpretation are introduced unless the drop size (or size distribution) is constant over the physical optical path in the scattering cloud.

Each of the above methods determines only the particle radius. However, once the radius has been determined, the corresponding number density can be obtained from Eq. (B-11) by using attenuation data for one wavelength. Thus, even the scattered light method requires an attenuation measurement to determine number density; the number density determination represents "integrated" data in either case.

REFERENCES


B-1 Mie, G., "Beiträge zur Optik trüber Medien, speziellkolloidaler Metallösungen", Ann. Physik, No. 3, Vol. 25, pp. 377-445, 1908.

B-2 Stratton, J. A., Electromagnetic Theory, pp. 563-573, McGraw-Hill Book Co., Inc., New York, 1941.

B-3 Stacey, K. A., Light-Scattering in Physical Chemistry, Academic Press, New York 1956.

B-4 Van de Hulst, H. C., Light Scattering by Small Particles, John Wiley and Sons, 1957.

B-5 Winkler, E. M., "Condensation Study by Absorption or Scattering of Light", High Speed Aerodynamics and Jet Propulsion, Vol. IX, Physical Measurements in Gas Dynamics and Combustion, pp. 289-306, Princeton University Press, Princeton, New Jersey, 1954.

B-6 Durbin, E. J., "Optical Methods Involving Light Scattering for Measuring Size and Concentration of Condensation Particles in Supercooled Hypersonic Flow", NACA TN 2441, August 1951.

B-7 Sinclair, D., and LaMer, V. K., "Light Scattering as a Measure of Particle Size in Aerosols", Chemical Review, Vol. 44, pp. 245-267, 1949.

B-8 Chu, C. M., Clark, G. C., and Churchill, S. W., Tables of Angular Distribution Coefficients for Light-Scattering by Spheres, Univ of Michigan Engineering Research Institute, Ann Arbor, 1957.

B-9 Pangonis, W. J., Heller, W., and Jacobson, A., Tables of Light Scattering Functions for Spherical Particles, Wayne State Univ Press, Detroit, Michigan, 1957.

B-10 Pangonis, W. J., and Heller, W., Angular Scattering Functions for Spherical Particles, Wayne State Univ Press, Detroit, Michigan, 1960.

B-11 Penndorf, R., "Scattering Coefficients for Absorbing and Nonabsorbing Spheres", AFCRL-TN 60-667, Tech Rept. RAD-TR-60-27, AVCO Co., Oct. 1960. Also, "Scattering and Extinction Coefficients for Small Absorbing and Nonabsorbing Aerosols", J. Opt. Soc. Am., Vol. 52, pp. 896-904, August 1962.

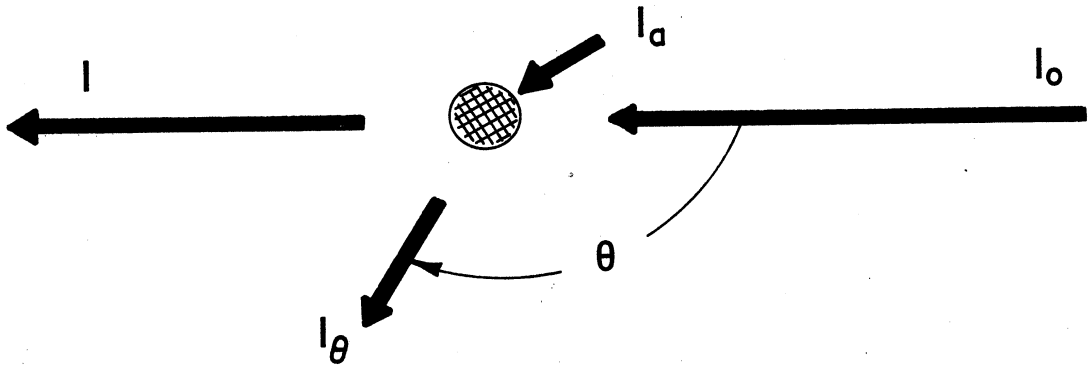


$I_o$ = Intensity of incident radiation

$I_\theta$ = Intensity of radiation scattered at an angle $\theta$ from the incident direction

$I_a$ = Equivalent intensity of radiation absorbed by the sphere

$I$ = Intensity of radiation transmitted in the direction of the incident wave

Figure B-1. Simplified Representation of Scattering Process

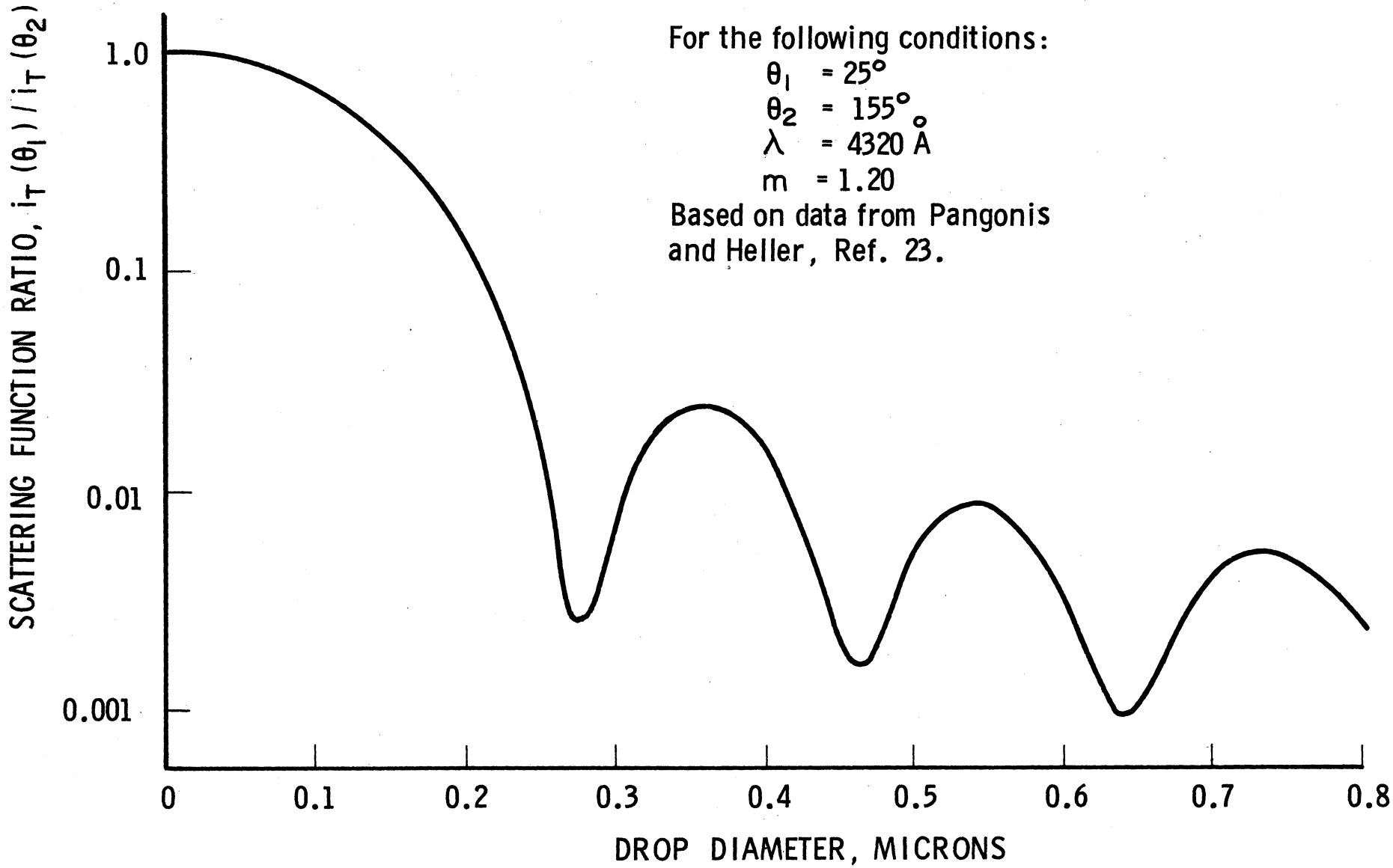


Figure B-2. Scattering Function Ratio vs Drop Diameter

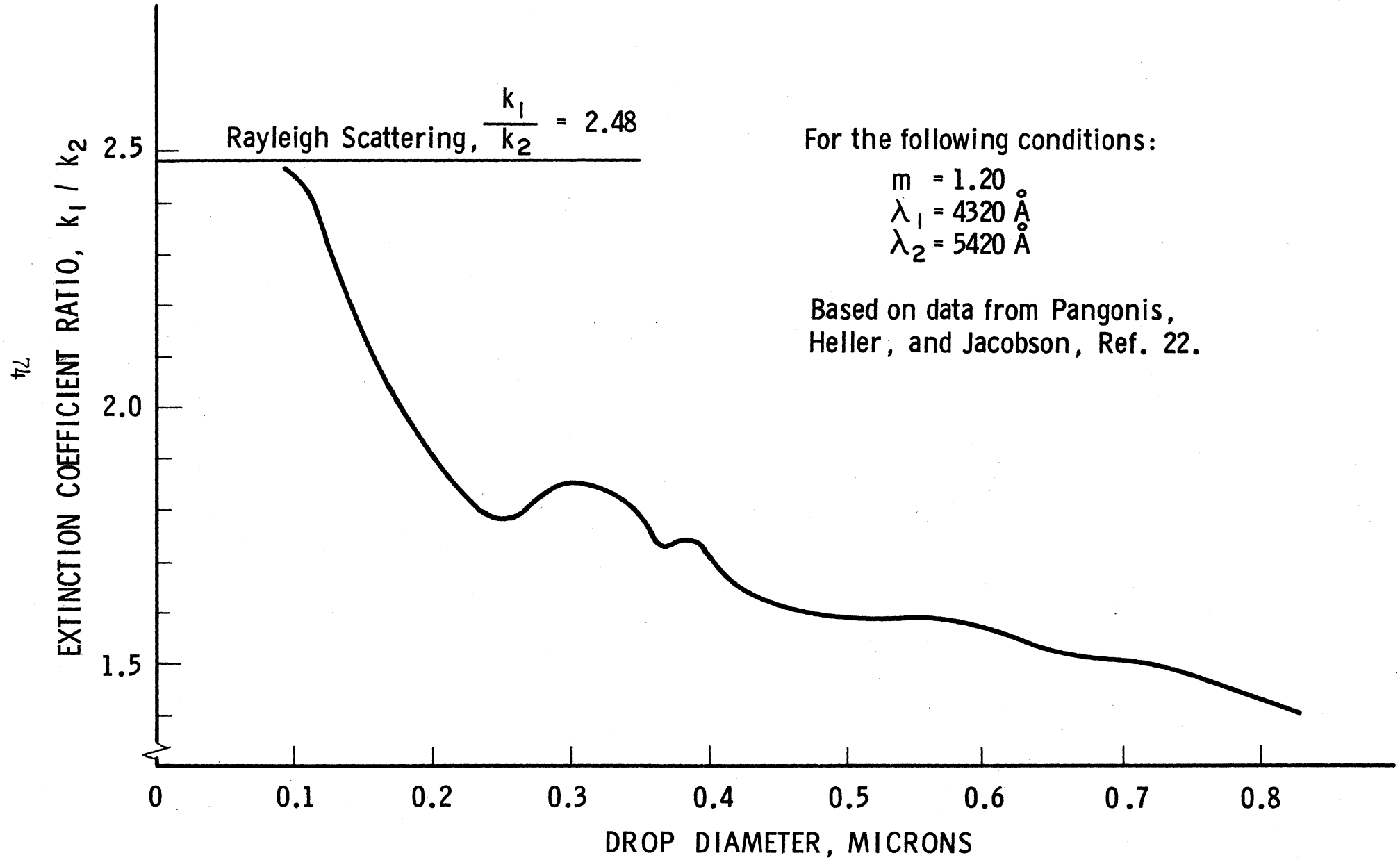


Figure B-3. Extinction Coefficient Ratio vs Drop Diameter

## APPENDIX C

## THE SENSITIVITY OF LIGHT SCATTERING MEASUREMENTS TO CONDENSATION PHENOMENA

K. R. Sivier

The condensation of a vapor, in a rapidly expanding flow, begins with the formation of a few, very small droplets or nuclei. The number of these droplets grows rapidly as nucleation continues. Additionally, their size increases due to condensation on the droplets themselves. The consideration of light scattering measurements, as an instrumentation technique for condensation studies, requires some information on the sensitivity of such measurements to these condensation phenomena.

An estimate of the sensitivity of light scattering measurements can be obtained by considering a simple binary mixture; i. e., molecular gas and condensed droplets of uniform size. The calculations, of the scattering from and attenuation of an unpolarized visible light beam by this mixture, are relatively simple.

Consider a cylindrical scattering volume, V, with cross-sectional area A and length $\ell$. The number of scattering particles (molecules) in this volume, before condensation begins, is

$$N_{m_o} = n_{m_o} V = \frac{p_o V}{kT_o} \qquad (C-1)$$

where $N_m$ = number of molecules in V

$n_m$ = number density of molecules

$p$ = pressure of molecular vapor

$T$ = temperature of molecular vapor

$k$ = Boltzmann's constant

$( )_o$ = conditions existing before condensation begins.

The mass of this uncondensed vapor is

$$M_o = N_{m_o} m_m = \frac{p_o \mathcal{M}}{R' T_o} V \qquad (C-2)$$

where $M$ = mass of vapor in V

$m_m$ = molecular mass

$\mathcal{M}$ = molecular weight of vapor

$R'$ = universal gas constant

If the total mass, of vapor plus condensate in V, is held constant as the condensation process proceeds, the number of gaseous molecules in V will be

$$N_m = n_m V = \frac{p_o V}{kT_o} (1 - g) \qquad (C-3)$$

where g = mass fraction of condensed vapor.

Also, the number of condensed droplets, having a radius $r_d$, will be

$$N_d = n_d V = \frac{gV}{\frac{4}{3}\pi r_d^3 \rho_L} \left( \frac{p_o \mathcal{M}}{R' T_o} \right) \qquad (C-4)$$

where $N_d$ = number of droplets, of radius $r_d$, in V

$n_d$ = number density of condensed droplets

$r_d$ = radius of condensed droplets

$\rho_L$ = mass density of the condensed vapor

The intensity attenuation ratio for a light beam passing lengthwise through the binary mixture in V is given by (Eq. (B-9), Appendix B)

$$\frac{I}{I_o} = \exp\left[ - \pi r_m^2 k_m n_m \ell - \pi r_d^2 k_d n_d \ell \right] \qquad (C-5)$$

where $I_o$ = intensity of the incident light beam

$I$ = intensity of the transmitted (attenuated) light beam

$\pi r_m^2 k_m = \sigma_m$

= scattering (extinction) cross-section of a molecular gas

$k_d$ = extinction coefficient for droplets of radius $r_d$.

Introducing molecular and droplet number densities from Eqs. (C-3) and (C-4), Eq. (C-5) can be written as

$$\frac{I}{I_o} = \exp\left\{ - \frac{p_o \ell}{T_o} \left[ \frac{\sigma_m}{k} (1 - g) + \frac{3 g k_d}{4 r_d \rho_L} \frac{M}{R} \right] \right\} \qquad (C-6)$$

Specializing to the case of nitrogen, Ref. C-1 gives the scattering cross-section of molecular nitrogen as

$$\sigma_m = \frac{4.41 \times 10^{-44}}{\lambda^4}, \ cm^2 \qquad (C-7)$$

where $\lambda$ = wavelength of the incident light, cm. Assuming Rayleigh scattering (i.e., $r_d << \lambda$) by the condensed droplets, the extinction coefficient, $k_d$, is given by (e.g., see Ref C-2).

$$k_d = \frac{8}{3} \left( \frac{m^2 - 1}{m^2 + 2} \right)^2 \alpha_d^4 \qquad (C-8)$$

where $\alpha_d = \frac{2 \pi r_d}{\lambda}$ and m equals the relative index of refraction of the droplet material. Incorporating (C-7) and (C-8) into (C-6) yields

$$\frac{I}{I_o} = \exp\left\{ - \frac{p_o \ell}{\lambda^4 T_o} \left[ \frac{4.41 \times 10^{-44}}{k} (1 - g) + \frac{32 \pi^4 r_d^3}{\rho_L} g \left( \frac{m^2 - 1}{m^2 + 2} \right)^2 \frac{M}{R} \right] \right\} \qquad (C-9)$$

Equation (C-9) was evaluated for nitrogen using the following data:

$p_o = 1$ psia $= 6.9 \times 10^4$ dynes/cm$^2$

$T_o = 50^oK$

(This represents a moderately supersaturated state for nitrogen.)

$\rho_L = 0.94$ gm/cm$^3$

$\ell = 10$ cm

$\lambda = 5000\ \mathring{A} = 5 \times 10^{-5}$ cm

$m = 1.2$

$M = 28$ gms/gmol

$R = 8.314 \times 10^7$ dyne-cm/gmol - $^oK$

$k = 1.329 \times 10^{-16}$ dyne-cm/$^oK$

These results, which are shown in Fig. C-1, suggest the difficulty involved in detecting the initial phases of condensation where the droplet diameters are on the order of $10^{-7}$ cm and the mass fraction of condensate is very small; i. e., $10^{-2}$ or smaller. On the other hand, once the instrumentation can detect the attenuation, the measurements are very sensitive to changes in droplet size; e. g., an order of magnitude change in attenuation corresponds to a factor of two in diameter for decreases in intensity greater than $10^{-5}$ of the incident light intensity.

Now, considering the case of Rayleigh scattering at 90 degrees, the ratio of scattered intensity to incident intensity for a single spherical particle, is given by (e. g., Ref. C-3)

$$\frac{I_{90^o}}{I_o} = \frac{8\pi^4}{R^2}\left(\frac{m^2 - 1}{m^2 + 2}\right)^2 \frac{r_d^6}{\lambda^4} \qquad \text{(C-10)}$$

If single scattering is assumed, the scattered intensity ratio for the binary condensing mixture, becomes

$$\frac{\bar{I}_{90^o}}{I_o} = \frac{8\pi^4}{R^2\lambda^4}\left(\frac{m^2 - 1}{m^2 + 2}\right)^2 \left(N_m r_m^6 + N_d r_d^6\right) \qquad \text{(C-11)}$$

Introducing the expressions for $N_m$ and $N_d$ from Eqs. (C-3) and (C-4), (C-11) becomes

$$\frac{\bar{I}_{90^o}}{I_o} = \frac{8\pi^4}{R^2\lambda^4}\left(\frac{m^2 - 1}{m^2 + 2}\right)^2 \frac{p_o V}{T_o}\left[\frac{r_m^6}{k}(1 - g) + \frac{3r_d^3}{4\pi\rho_L}\left(\frac{M}{R}\right) g\right] \qquad \text{(C-12)}$$

Equation (C-12) has been evaluated for nitrogen using the data introduced above for the intensity attenuation calculation and the following additional data:

$r_m = 1.5 \times 10^{-8}$ cm

$V = 1.0$ cm$^3$

$R = 10.0$ cm

The results, which are presented in Fig. C-2, again show the extreme instrumentation difficulties involved in detecting the initial phases of the condensation process and the sensitivity to drop size at intensity ratios in excess of $10^{-10}$.

REFERENCES

C-1. Dalgarno, A., "Spectral Reflectivity of the Earth's Atmosphere III: The Scattering of Light by Atomic Systems," Geophysics Corporation of America Technical Report No. 62-28-A, December, 1962.

C-2. Penndorf, R., "Scattering Coefficients for Absorbing and Nonabsorbing Spheres," AFCRL-TN 60-667, Tech. Rept. RAD-TR-60-27, AVCO Co., October 1960.

C-3. Sinclair, D., and LaMer, V. K., "Light Scattering as a Measure of Particle Size in Aerosols," Chemical Review, 44, 245-267, 1949.

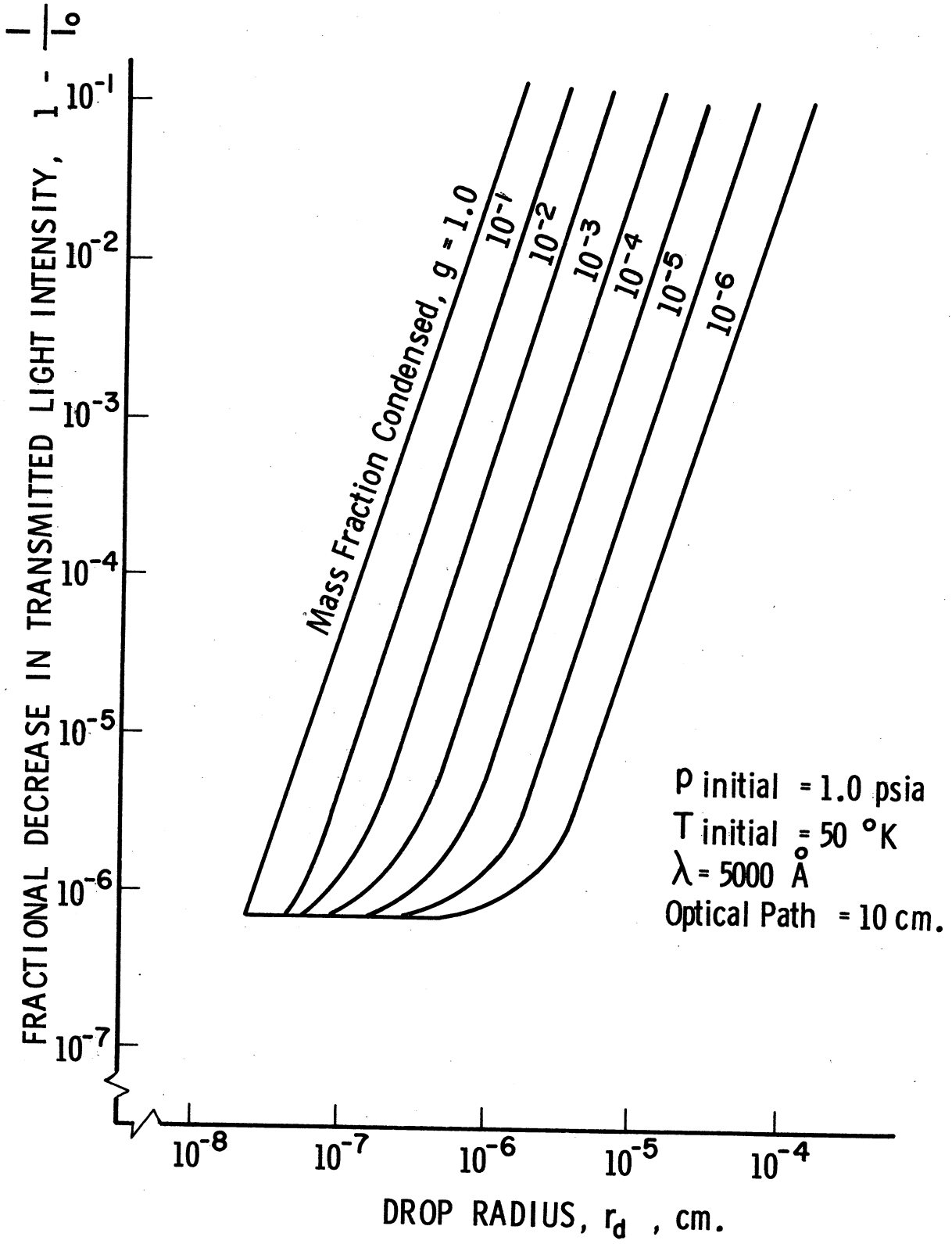


Figure C-1. Decrease in Transmitted Light Intensity Due to Condensation in Nitrogen (Binary Mixture Model)

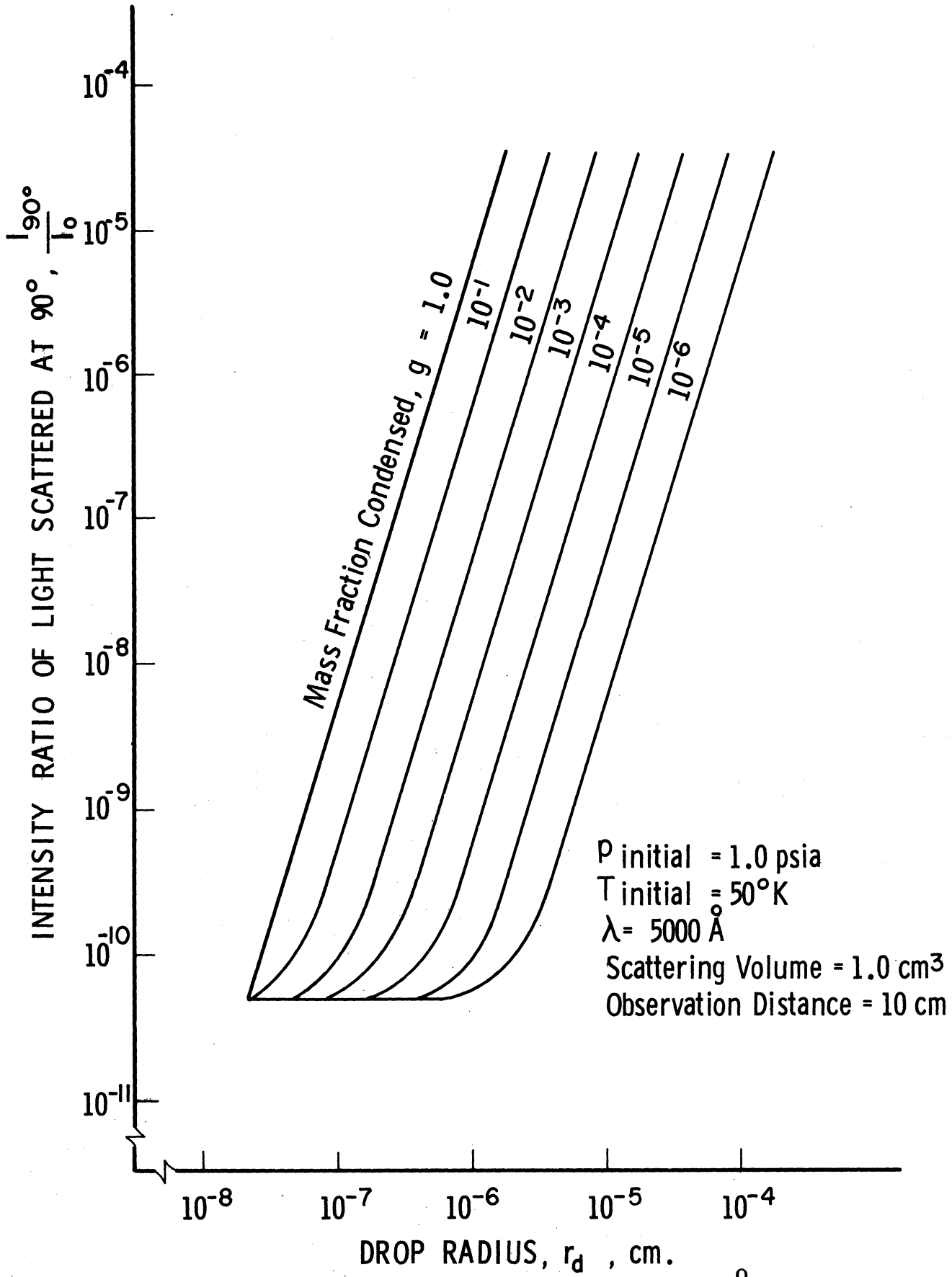


Figure C-2. Intensity of Light Scattered at 90° by Condensing Nitrogen (Binary Mixture Model)

# APPENDIX D

## LIGHT SCATTERING INSTRUMENTATION

E. Oktay

### INITIAL LIGHT SCATTERING SYSTEM

The initial light scattering system was designed to allow the simultaneous study of scattered and transmitted light measurements. A schematic drawing of the initial system is shown in Fig. D-1. A 100 watt PEK 110 high pressure mercury arc lamp was used as the light source. This lamp has a 0.012 x 0.012 inch arc source size. The light from the source was collimated to a 1.5 inch diameter beam and an aperture plate formed the 1/8-inch diameter unfiltered beam used in the experiments. The circuit diagram for the battery power supply, used with PEK 110, is shown in Fig. D-2. Batteries were used as a power source to eliminate light intensity fluctuations due to the "ripple" that is characteristic in the output of rectified a. c. power supplies.

Four 931A photomultiplier tubes were used to monitor the scattered and transmitted light. Tubes No. 1 and No. 2, used for the scattered light measurements, were located in light tight boxes at scattering angles of 25 and 155 degrees, respectively. The field-of-view of these tubes was controlled by baffled light tubes. Interference from ambient lighting was reduced by the use of a dull black background material mounted in the line-of-sight of the tubes but beyond the scattering region. The light entering the tubes was filtered for the 4320 $\mathring{A}$ mercury line by using Farrand interference filters having half band widths of about 150 $\mathring{A}$.

Tubes No. 3 and No. 4 were used to measure the intensity of the transmitted beam. The beam entered the light tight enclosure through a baffled light tube,

used to control effects of ambient light. A beam splitter[1] was used to supply a portion of the beam to each of the two photomultipliers. The resulting beams were filtered to obtain the 5420 Å (to tube No. 3 and called the "direct" beam) and 4320 Å (to tube No. 4 and called the "reflected" beam) mercury lines. Because of its intensity, it was necessary to attenuate the transmitted beam, by a factor of 100 to 1000, to avoid saturating these photomultiplier tubes. This attenuation was achieved by neutral density filters placed ahead of the beam splitter.

As pointed out in Ref. D-1, the photomultiplier cathode surface is not uniformly sensitive. To reduce the effects of motion, due to system vibration, of the light beam over the cathode surface, diffusing lenses were placed ahead of each tube to increase the size of beam falling on the cathode.

Figure D-3 presents a diagram of the circuit used with each of the photomultiplier tubes. The tubes were powered by a common set of dry cell batteries. The output of the tubes was read directly by a Tektronix 531 A oscilloscope using a Type M, 4-trace, plug-in unit. This combination permitted the simultaneous measurement of the outputs from all four photomultiplier tubes. The data were recorded by a Polaroid oscilloscope camera.

## APPARATUS FOR DEVELOPING LIGHT SCATTERING INSTRUMENTATION

On the basis of the attempts to make meaningful light scattering measurements with the underexpanded jet flow (as described in Section 3.2), it was concluded that scattered light studies were not feasible at the present time. The scattered light level was inadequate with a condensation level causing very large

---

[1] The beam splitter, supplied by the Liberty Mirror Division of the Libbey-Owens Ford Glass Co., was coated with dichroic coating No. 31018. When used at an incidence of 45°, this coating transmits approximately 80% of the light at 5420 Å and reflects approximately 95% of the light at 4320 Å.

attenuations of the incident beam. The lower condensation level necessary to obtain single scattering would result in an even lower scattered light intensity. Therefore, efforts to make scattered light measurements were abandoned.

The underexpanded jet experiments also indicated several other problem areas in the use of light scattering instrumentation, in general, and in making transmitted light attenuation measurements, in particular. These problems were in the areas of (1) physical arrangement of the apparatus, (2) electronic circuitry, and (3) instrument sensitivity and data output. To permit the careful study of these problems, and their solutions, a special apparatus was designed and built. This apparatus is primarily for making transmitted light measurements and is arranged to permit absolute system calibrations using specially prepared colloidal solutions of known particle size and number density.

## A. Physical Arrangement of the Apparatus

The original light scattering apparatus was affected by the ambient light of the room in which the experiments were being conducted. Variations in the intensity of this ambient light inevitably resulted in inconsistent data. Therefore, in the new apparatus, shown in Fig. D-4, all the system components are enclosed in a light tight box. The inside of the box is painted dull black to minimize reflected light effects.

The original system was subject to vibrations from the operation of the pressure release mechanism and from the shock waves generated by the free jet. These vibrations caused fluctuations of the light beam over the cathode surface. The effects of these fluctuations, although minimized by the diverging lenses previously mentioned, were sufficient to cause extraneous noise in the photomultiplier outputs. Although the new apparatus is not intended for use with an underexpanded jet, all components are mounted more rigidly to minimize vibration effects.

B. Electronic Circuitry

The problems with the electronic circuitry involved the power supply, the dynode circuitry, and the inherent noise of the photomultipliers.

(1) Power Supply. In the original apparatus, a set of dry cell batteries was used as the power supply. The power output of these batteries decreased during the experiments because of the unavoidably high drain caused by the four photomultiplier circuits. It is noted, from the characteristic curves for the RCA 931A photomultiplier tubes, that the median sensitivity of the tubes decreases from $25 \times 10^5$, at a supply voltage of 1000 v, to $4 \times 10^5$ at 900 v. This drift in the sensitivity of the photomultiplier resulted in unreliable data. In the new system, this problem was eliminated by incorporating a well regulated and very stable d. c. power supply, Honeywell Model 3K20.

(2) Dynode Circuitry. It is recommended in Ref. D-2 that the ratio of the dynode current to the plate current be at least 5. 0 in order to maintain the linearity of the photomultiplier. A very small load resistance is also recommended. A schematic of the revised photomultiplier circuitry is shown in Fig. D-5. Experiments with this circuitry showed that the photomultiplier was linear up to a plate current of 250 $\mu$a while the dynode current was 1440 $\mu$a at a supply voltage of 750 v. This represents a dynode to plate current ratio of about 5. 7.

(3) Noise. As reported in Refs. D-3 and D-4, ohmic leakage noise, thermal noise, and fluctuations due to statistical behavior of the electron emission from the photo-cathode become significant at low light levels. Experiments with the new system showed that the signal-to-noise ratio dropped from 4000 at a plate current of 60 $\mu$a to about 10 at .05 $\mu$a. Also, the noise level of the output increased as the supply voltage was increased. Therefore, in operating the new system, the supply voltage was reduced to 750 volts and the maximum light intensity was adjusted to yield a plate current of 60 $\mu$a at this voltage.

C. Sensitivity and Data Output

In the original system, two separate readings (the tare and the actual run) were necessary to determine the attenuation of the incident beam. Figure D-6 shows typical oscilloscope photographs from two such runs. The upper photograph is a recording of the tare data. For this run exactly the same procedure is used as in an actual run except that the chamber is not pressurized; i. e., the pressure release mechanism is cocked and triggered giving a record of the output of tubes No. 3 and No. 4 with unattenuated light input. The lower photograph is a recording of the outputs of the photomultipliers during the actual run. These photographs show that, due to reading error and photomultiplier output fluctuations, it is impossible to read attenuations of less than about 2% with reasonable accuracy.

In the new system, a single oscillograph trace yields the attenuation data directly and with much greater accuracy. This change in data output is accomplished electronically by means of differential amplifiers. The schematic diagram of the new output system is shown in Fig. D-7. Photomultipliers 1a. and 1b. record the intensity of the incident beam at wavelengths of 4320 $\mathring{A}$ and 5420 $\mathring{A}$ and photomultipliers 2a. and 2b. record the intensity of the transmitted beam at 4320 $\mathring{A}$ and 5420 $\mathring{A}$. The difference between the outputs of the photomultiplier 1a. and 2a. is proportional to the attenuation of the incident beam at 4320 $\mathring{A}$ and the difference between the outputs of photomultipliers 1b. and 2b. represents the attenuation of incident light at 5420 $\mathring{A}$. These differences are amplified by Type D Tektronix High Gain Differential Amplifiers, which at present make it possible to detect attenuations as low as 0. 1%.

REFERENCES

D-1 Christensen, R. L., and Ames, I., "Absolute Calibration of a Light Detector", J. Opt. Soc. Am., Vol. 51, No. 2, February 1961.

D-2 Sharpe, T., "Photoelectric Cells and Photomultipliers", Electronic Techniques, June 1961.

D-3 Engstrom, R. W., "Multiplier-Phototube Characteristics Application to Low Light Levels", J. Opt. Soc. Am., Vol. 37, No. 6, June 1947.

D-4 Price, W. J., Nuclear Radiation Detection, Ch. 7, McGraw-Hill, Inc. 1958.

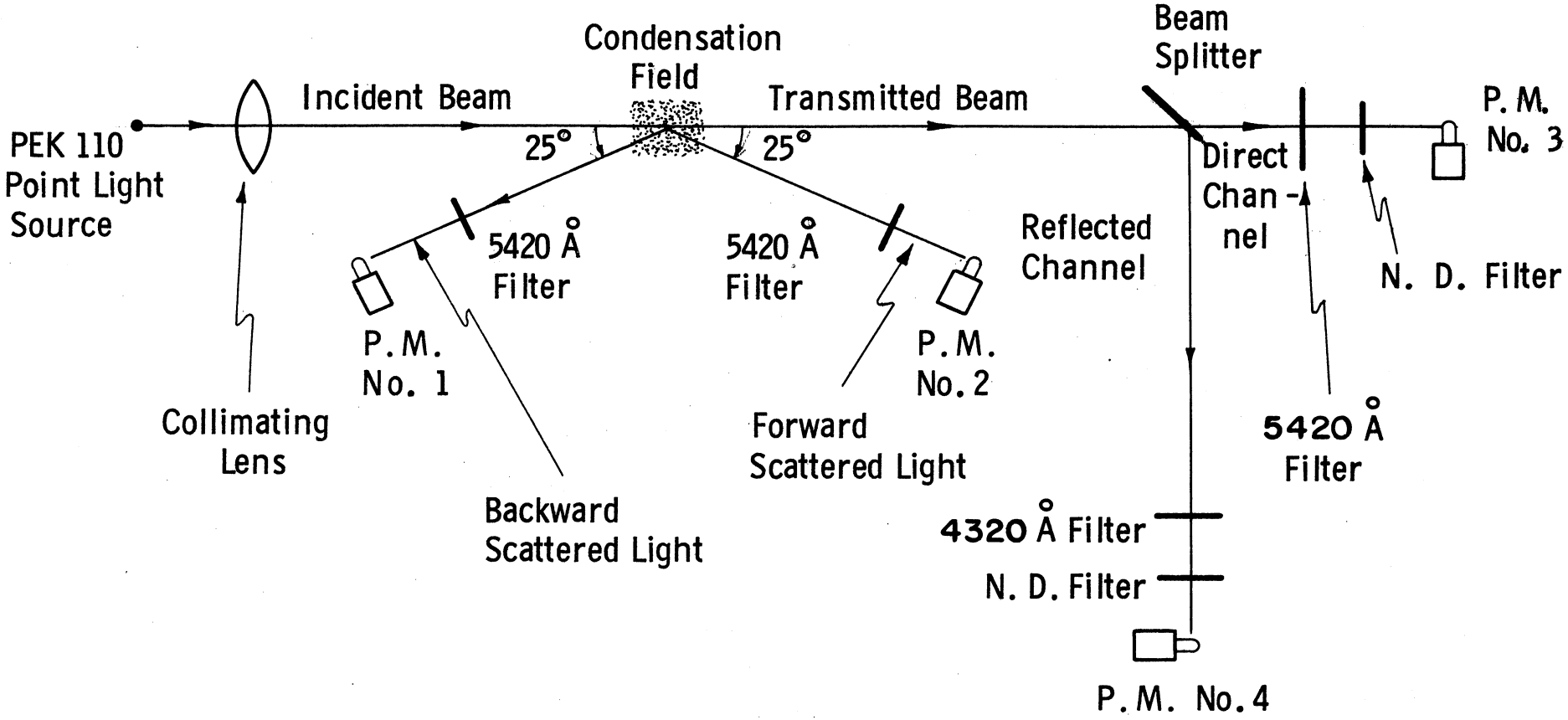


Figure D-1. Schematic Drawing of the Initial Light Scattering System

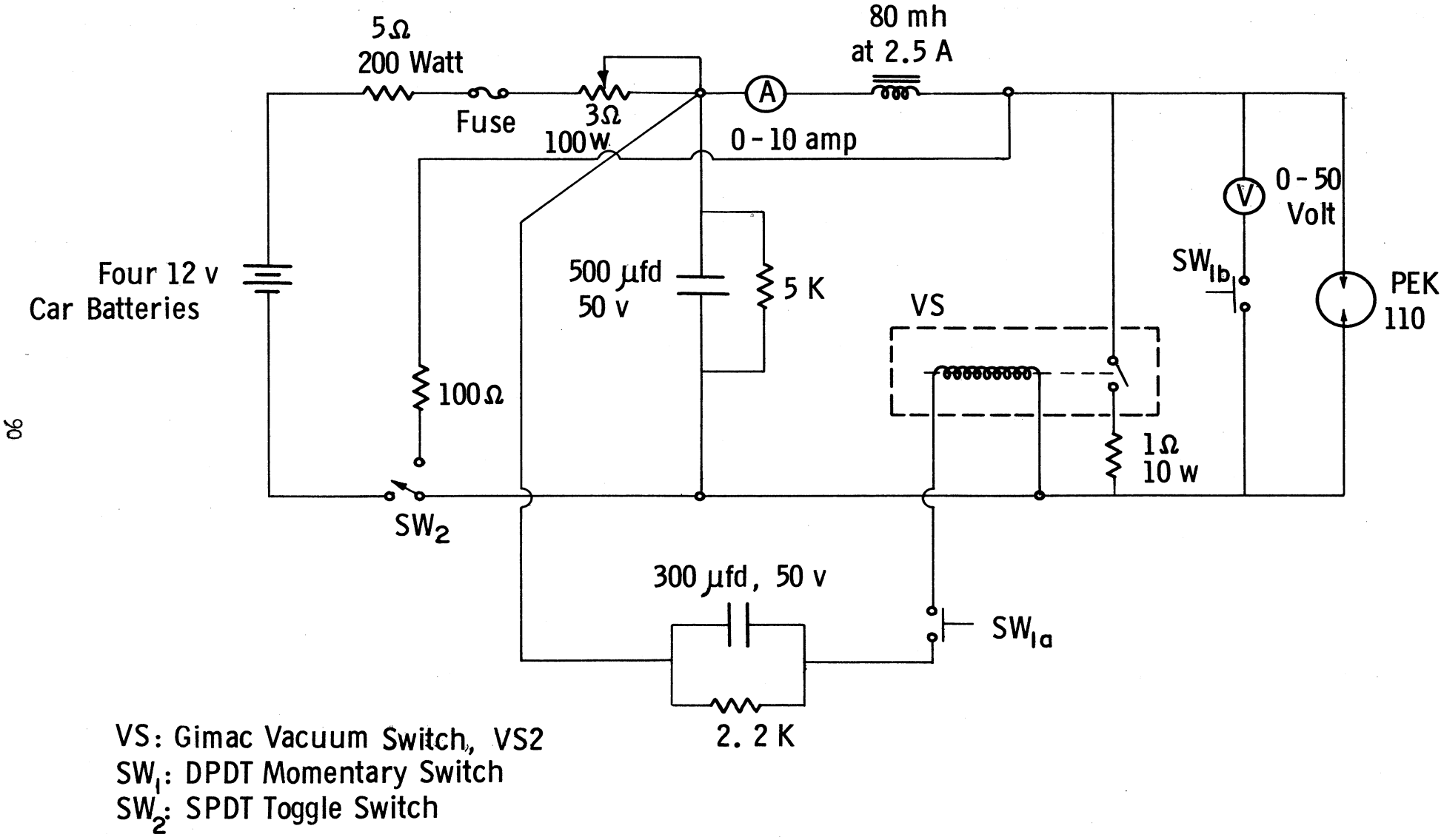


Figure D-2. Circuit Diagram for the PEK 110 Battery Power Supply

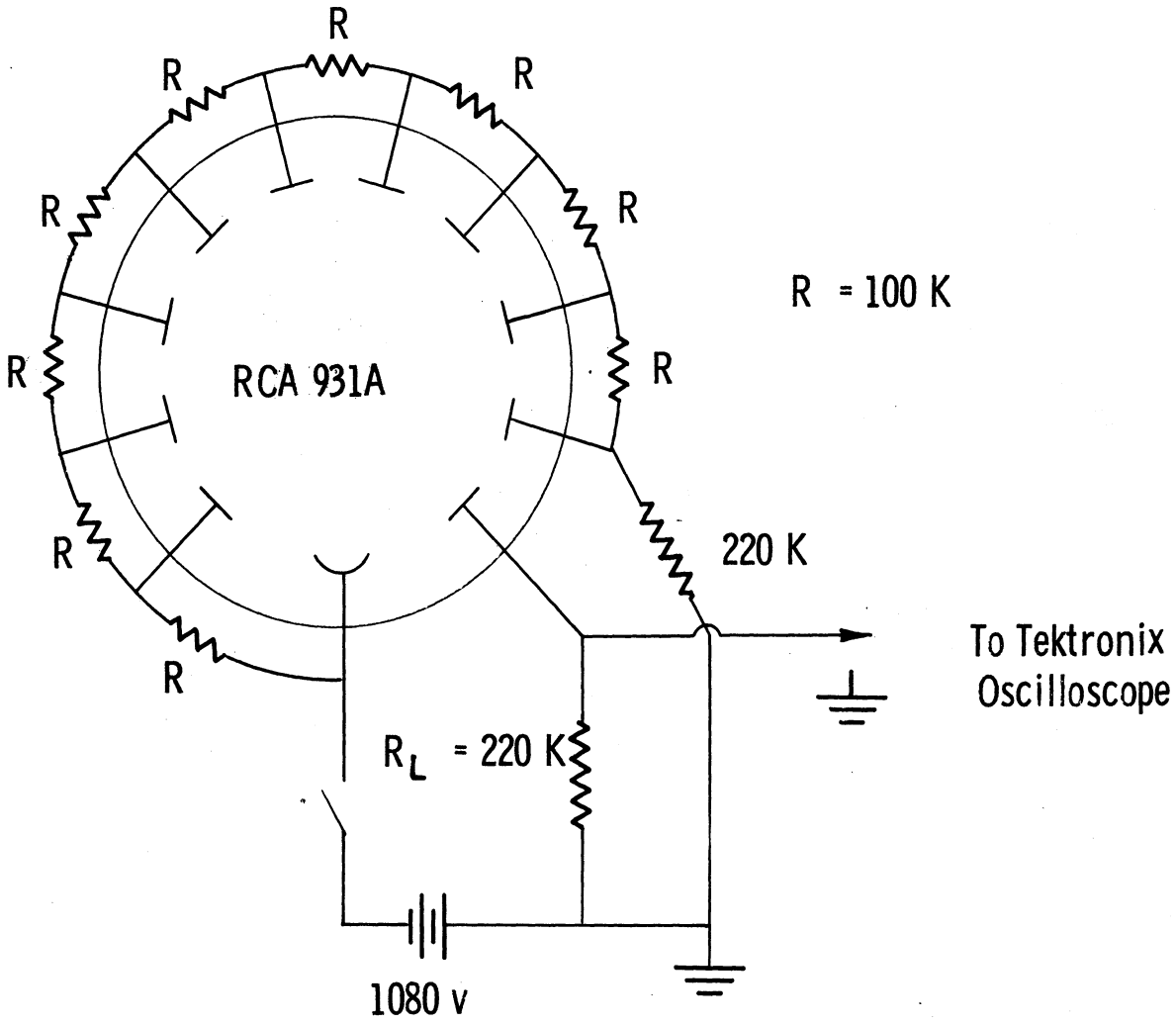


Figure D-3. Photomultiplier Circuit Diagram

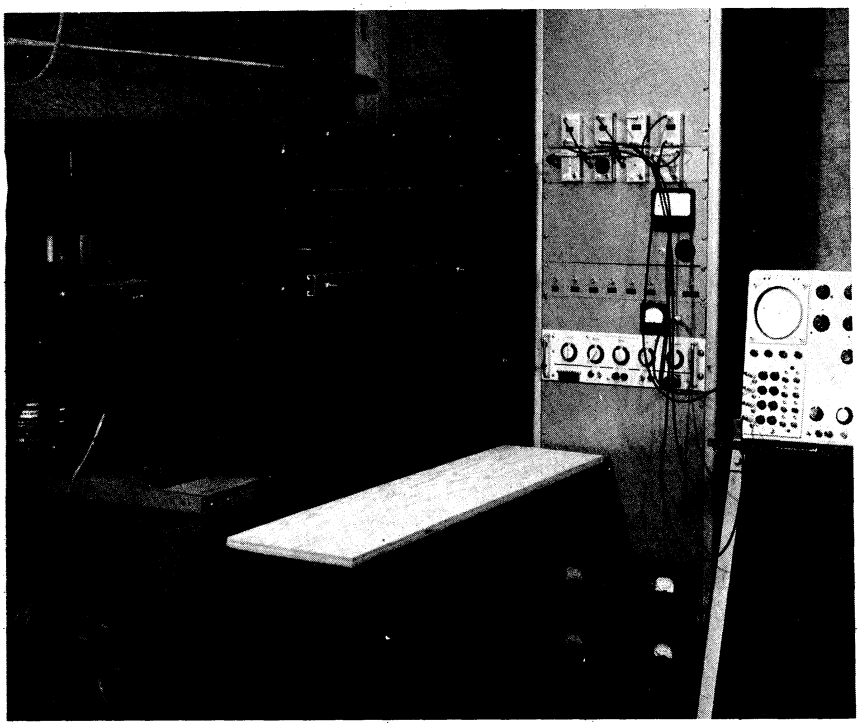

Figure D-4. Photograph of Light-Tight Box and Instrumentation Panel for the Improved Light Scattering System

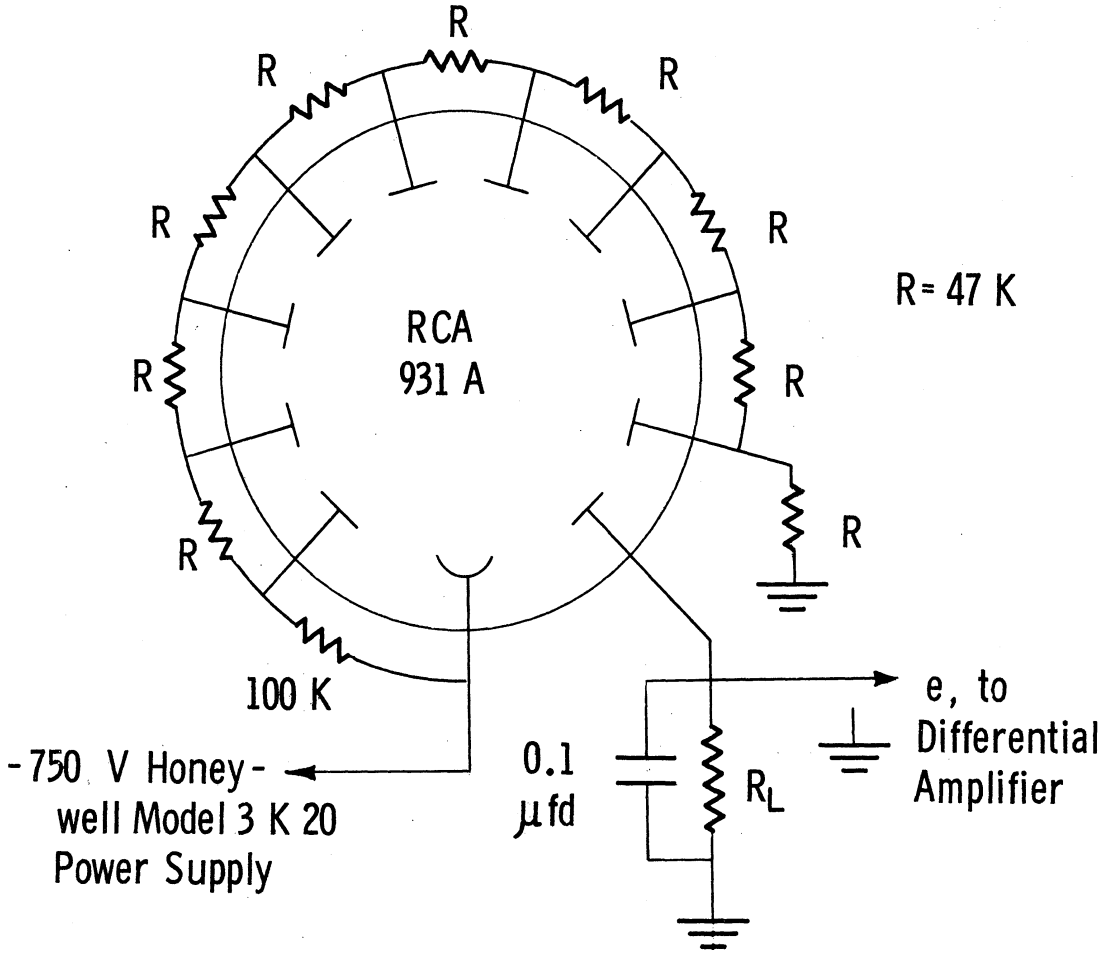


$R_L$ = 47 K for Photomultiplier No. 1b and 2b

= Variable from 10 to 100 K for Photomultiplier No. 1a and 2a

Figure D-5. Revised Photomultiplier Circuit Diagram

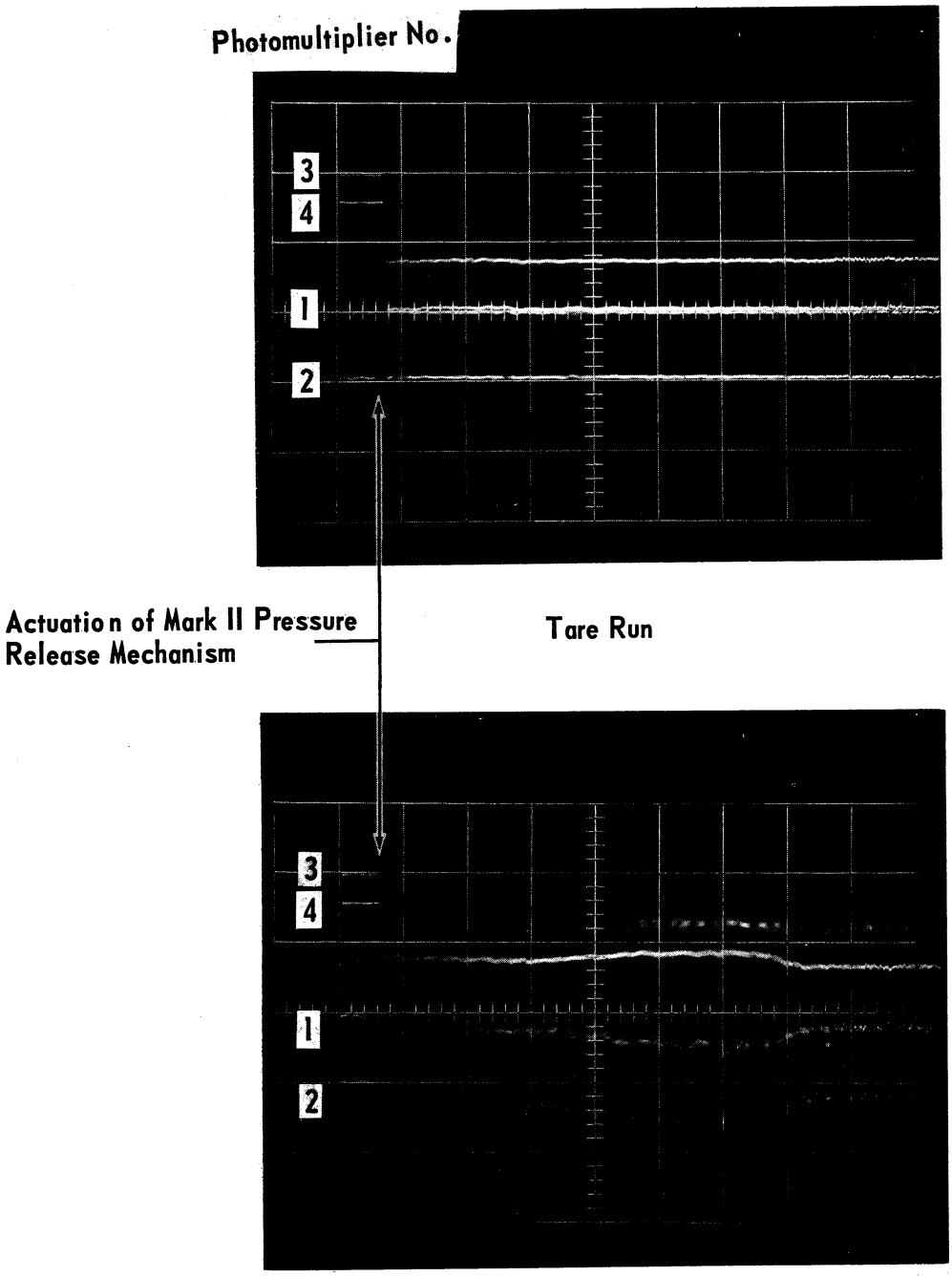


Figure D-6. Typical Oscillograph Traces From Light Scattering Tests on Underexpanded Nitrogen Jet

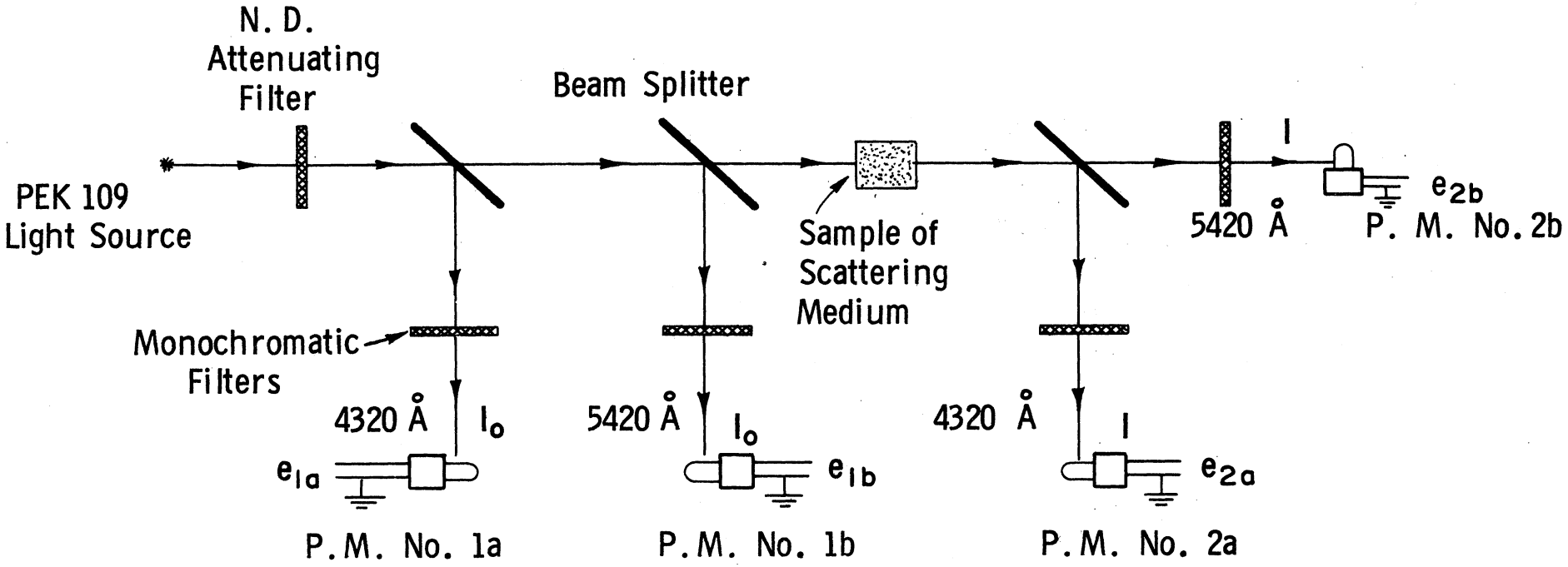


$I_o$ is proportional to Incident Beam

I is proportional to Transmitted Beam

Outputs $e_{1a}$ and $e_{2a}$ are fed into one Differential Amplifier

Outputs $e_{1b}$ and $e_{2b}$ are fed into second Differential Amplifier

Figure D-7. Schematic Diagram of New System for Light Scattering Studies

## APPENDIX E

## EXPOSURE TIME REQUIREMENTS FOR BRIGHT FIELD PHOTOGRAPHY OF SMALL, HIGH-SPEED PARTICLES

S. Goddard

In order to distinquish an object image from the background in a photograph, it is necessary to obtain some minimum contrast between them. The condition of adequate contrast can be described in terms of the image, negative and print contrasts, Ref. E-1. In the case of bright field photography, in which the object is located between the light source and the camera, the background is more intensely illuminated than the image and these contrasts are defined as

$$\text{Image Contrast, } C_I = \log_{10} \frac{\text{(background exposure)}}{\text{(image exposure)}}$$

$$\text{Negative Contrast, } C_N = \log_{10} \frac{\text{(intensity of transmitted light through the image on negative)}}{\text{(intensity of transmitted light through the background on negative)}}$$

$$\text{Print Contrast, } C_P = \log_{10} \frac{\text{(intensity of light reflected from the background portion on prints)}}{\text{(intensity of light reflected from the image portion on prints)}}$$

These contrasts are related by the expressions

$$C_P = \gamma_P \, C_N = \gamma_P \, \gamma_N \, C_I$$

$$C_N = \gamma_N \, C_I$$

where $\gamma_P$ and $\gamma_N$ are the "gammas" of the printing paper and film respectively; i. e., the slopes of the straight-line portions of the density and exposure characteristic curves of the printing paper or film.

According to Ref. E-1, $C_I$ should be close to one or greater if a negative of good quality is to be obtained; this requires a ratio of background intensity to

image intensity of 10:1. In addition, Ref. E-1 points out that $C_N$ should be equal to or greater than 0.5 if the emulsion is to resolve the image properly.

For most "fast" films, the maximum value of $\gamma_N$ is around 1.6. Therefore, from the requirement of $C_N \geq 0.5$, the exposure ratio between the background and image should not be less than 2.05. This restricts the image movement to less than one image diameter during the time of exposure.

The above limitation on image motion enables an estimate of the allowable exposure time to be made. Such an estimate is shown in Fig. E-1, in which the sizes of particles which are visible to the film are plotted against the velocity of moving particles for exposure times of 5, 1 and 0.1 nanosecond. Such short exposure times require special shuttering devices or illumination by short duration light sources. The usable exposure time ranges for the various exposure control methods are shown in Fig. E-2. It is seen that Kerr cells and image converter tubes are the only exposure control devices commercially available in the nanosecond time range. However, both of these systems are presently limited to a minimum exposure time of about $5 \times 10^{-9}$ seconds. In addition, the light transmission efficiency of Kerr cells and the resolution of image converters are very poor. Therefore, a considerable advance in very fast shuttering devices is necessary in order to allow bright field photography of micron size particles flowing at high speeds.

This restriction on the distance of image movement does not exist in the dark field illuminating system. In the dark field system, no light from the light source except that reflected from the particle is "seen" by the camera. Thus, the particle is seen as a bright image against a dark, or even black background. Although in this case infinite contrast is theoretically possible, it is unlikely to be realized because of low power stray ambient light entering the photographic field.

Reference E-1: Holder, D. W., North, R. J., and Wood, G. P., "Optical Methods for Examining the Flow in High-Speed Wind Tunnel", AGARDograph 23, Nov. 1956.

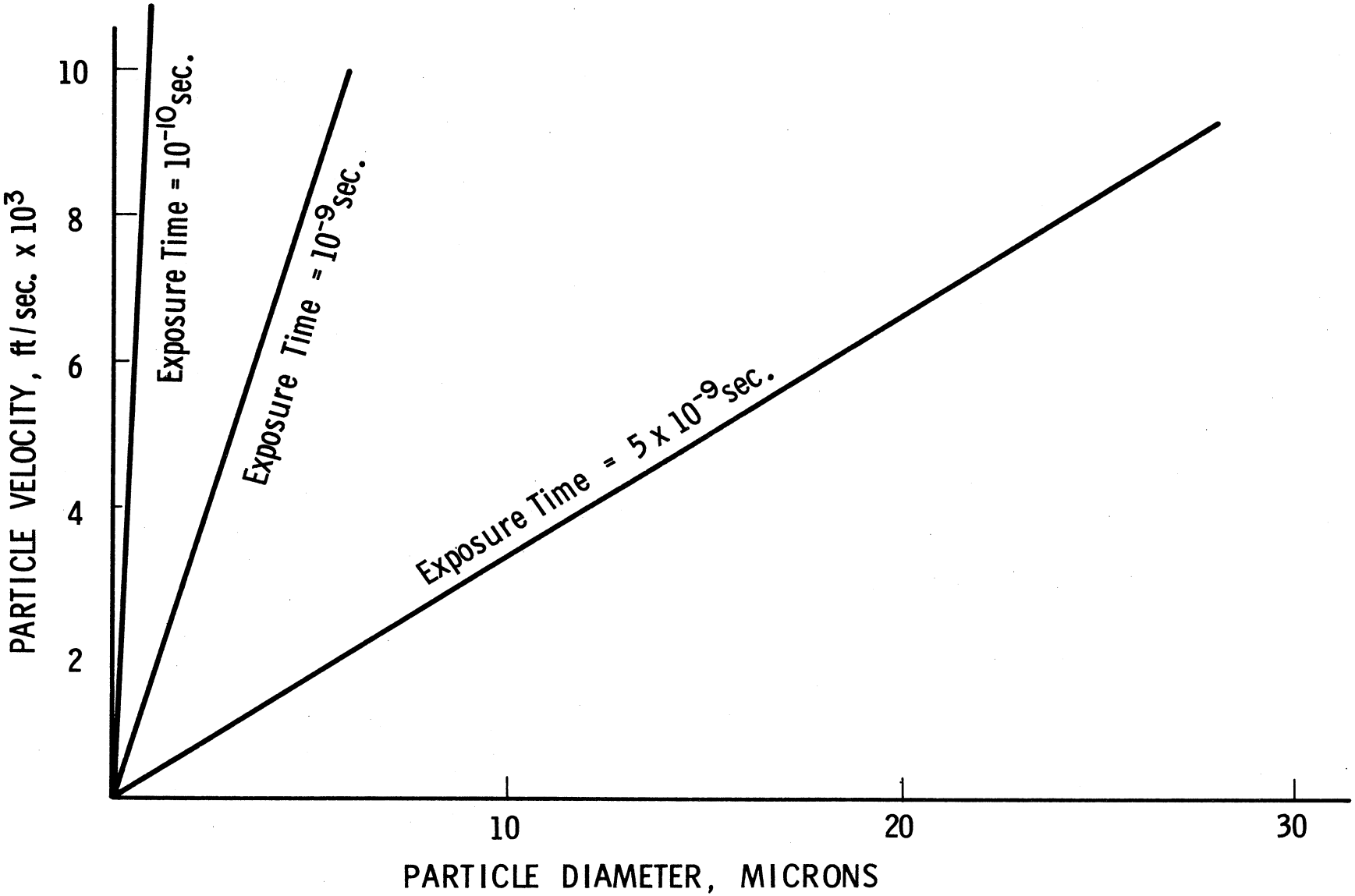


Figure E-1. Maximum Particle Velocity for Adequate Negative Contrast in Bright Field Photography

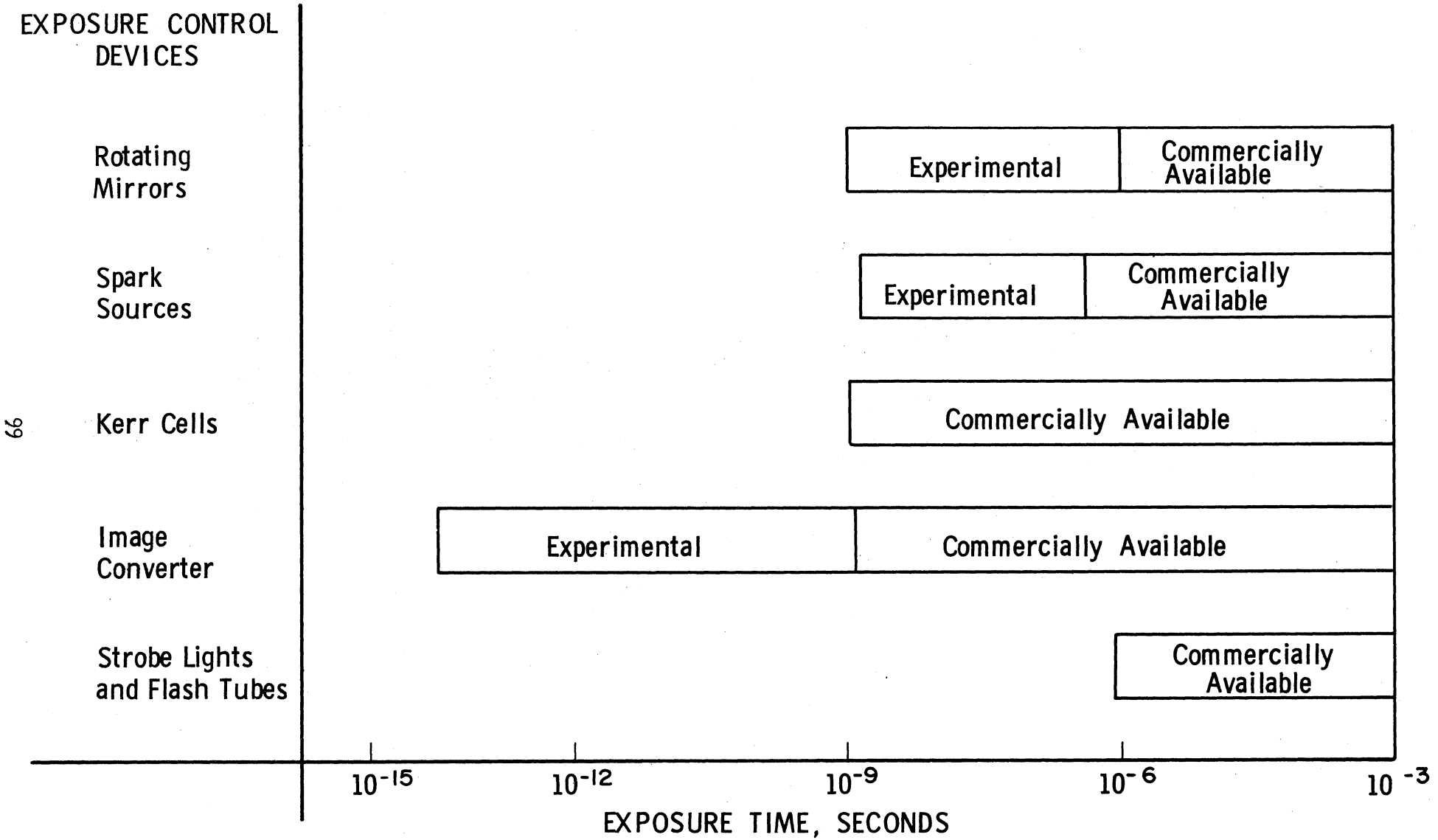


Figure E-2. Summary of Performance of Various Exposure Control Devices

# APPENDIX F

## APPARATUS REQUIREMENTS FOR PHOTOMICROGRAPHIC STUDIES

P. L. Lu

### MAGNIFICATION AND RESOLVING POWER

Two types of camera systems can be used in photomicrography. One uses a long extension camera with an ordinary photographic lens of short focal length. The other system uses a combination of a microscope and a camera back. The latter system is preferable due to its compactness and larger possible magnifying power.

Several factors determine the required magnifying power of the camera system. They are (1) the size of particles to be measured, (2) the resolving power of the film, (3) the brightness of the light source, and (4) the resolving power of the objective lens.

The image size is controlled by the magnifying powers of the objective and eyepiece and by the bellows extension of the camera. However, there is a usable limit of magnification which can be achieved with a particular combination of objective, eyepiece, and bellows extension. If the magnification of the camera system is carried beyond this limit, no additional detail is obtained even though the image becomes larger.

The usable limit of magnification of a camera system is controlled by the resolving power of the objective; i. e., the ability of a lens to render fine details. Usually, the resolving power is given as the number of fine lines per unit distance that can be distinquished, e. g., lines/mm. According to the Rayleigh criterion (Ref. F-1), the resolving power of an objective can be expressed as

$$RP = \frac{1}{S} = \frac{1}{\frac{.61\lambda}{NA}} \quad , \qquad \text{(F-1)}$$

where S is the minimum distance between two self-luminous points, $\lambda$ is the wavelength of light, and NA is the numerical aperture of the objective. The NA is equal to the product of the index refraction m, of the medium in which the object is situated, and the sine of the half angle u of the cone of rays admitted by the objective; i. e., NA = m sine u. As a first order approximation, this may be written

$$NA = \frac{\text{m x diameter of the effective aperture of lens}}{\text{2 x equivalent focus}} \qquad \text{(F-2)}$$

Here, the equivalent focus is the object-to-lens distance when the object is in focus. Equation (F-1) shows that an objective with a large NA and light with a low wavelength has a large resolving power. This value, for a given objective/light combination, gives the upper-bound that a particular camera system can achieve. The resolving power for several different lenses, based on a wavelength of 5500 $\mathring{A}$, have been tabulated in Table F-1.

From Eq. (F-2) above, it is apparent that the larger the NA of an objective, the smaller will be its focal length. Due to the present application to the photography of particles in a supersonic stream, a lens system with a too short focal length is not desirable. Such a lens system can protrude too deeply and disturb the flow field. This restriction gives a loose boundary of the most powerful objective which can be used.

The resolving power of a film is defined in the same way as the resolving power of a lens; the number of resolved lines per unit distance. Generally, a "fast" film has a low resolving power. For ordinary high-speed, general-purpose film, e. g., Kodak Royal X-Pan, the resolving power is about 40 lines/mm, under forced developing conditions.

Knowing the resolving power of the lens and the film, it is possible to determine the minimum magnification required to produce a photograph showing the desired details of the object. This minimum magnification is given by the

relation (Ref. F-2)

$$M = \frac{NA}{.61\lambda} \quad \frac{1}{\text{resolving power of film}} \qquad \text{(F-3)}$$

As an example, the minimum magnification for a system with a 0.10 NA objective and a film with a resolution of 40 lines/mm will be 7.45, if 5500 Å light is used. This number is only a general guide for the lower limit of magnification which the system may require. The image thus produced, although adequately resolved on the film, may be still too small for human eyes to resolve. Additional optical aids may be needed in order to obtain the desired information from the photograph.

EXPOSURE TIME

In photomicrography work, there are two commonly used illuminating systems; bright field and dark field illumination. In the bright field illuminating system, which is also known as transmitted light system, the subjects are photographed by transmitted light and appear dark against a bright background. In the dark field system, no direct illuminating light enters the objective. Only light that is scattered or reflected by the object enters the objective and the images appear bright against a dark background.

At high particle speeds, it is very difficult to "freeze" the motion of the image on the film. Instead of photographs of "stationary" particles, streak photographs can be obtained more easily. However, in order to separate the streak images from the background there must be good contrast between the streak images and the background illumination. As shown in the Appendix E, the image contrast requirement limits particle motion to less than one diameter when bright field illumination is used. This, in turn, requires a very short exposure time, achieved by either a very fast shutter or a short duration light source. As an example, a one micron diameter particle moving at a speed of 1000 ft/sec requires an exposure time of less than 3.3 nanoseconds.

With dark field illumination, it is possible to obtain sufficient contrast between the image and the background with streak lengths many times larger than the diameter of the particle image. Therefore, contrast requirements normally do not limit the exposure time for the dark field illuminating system.

The image streak length is directly proportional to the product of the exposure time, the particle speed, and the magnification of the camera. It is desirable that the exposure time be kept short enough so that a complete streak is seen on the photograph. As an example, the exposure time for a one micron diameter particle, moving at a speed of 1000 ft/sec, will be about 3 microseconds if the streak length is to be less than a 5-inch width of film and a magnification of 40 is used.

The density of the photographic image on the film is normally a function only of the film exposure; the product of the incident light intensity and the time duration of the exposure. This is referred to as the reciprocity law. However, this simple film density/exposure relationship does not hold for very low light intensity or very short exposures. Although the validity of the reciprocity law for sub-microsecond exposures is uncertain, Castle (Ref. F-3) has reported no appreciable loss in film sensitivity for exposures on the order of a microsecond. It seems safe, therefore, to assume that the reciprocity law is applicable to the work that follows.

Two approaches can be used to obtain short exposure times. They are the combination of a steady light source and a shutter and the flash light source. The fastest commercial shutter is the Kerr cell, which has a time duration as low as 1 nanosecond. However, due to its poor transmission efficiency, i. e., only 7% of the incident light is transmitted, it is impractical for the present application. For an example, the intensity of the brightest carbon arcs is about 90,000 candles/$cm^2$. After transmission by a Kerr cell, the intensity is only about 6300 candle/$cm^2$. In comparison with the brightness of the spark light source described below, this value is very low.

There are two general types of flash light sources, namely; the gas-filled flash tube and the open electrode spark gap. Both are powered by capacitor discharges. The best output of either of these light sources is about $50 \times 10^6$ candles/cm$^2$ with a minimum time duration of 0.5 microsecond.(Refs. F-4 and F-5).

It is of interest to estimate the exposure requirement (intensity times time) of the photomicrography system and compare it with the performance of the above light sources. Due to the complexity of the problem, only a lower bound for the exposure can be estimated. Let the illuminance of a light source be B candles/cm$^2$. The light source image formed by the condenser lens will be of the same intensity B if it is assumed that there is no loss through the condenser. If each particle acts as a mirror, the amount of light captured by the camera will be $R_f B\ \omega$ lumens/cm$^2$, where $\omega$ is the solid angle extending from the particle to the objective of the camera and $R_f$ is the reflection factor of the surface of the particles. The geometrical relationship is shown in Fig. F-1. During the exposure time t, the streak length is equal to Vt + d, where d is the diameter of the light source image on a particle moving at a velocity V. Considering the linear magnification M, the transmission factor T of both the condenser system and the camera system, and the included angle $\theta$ between the light path and camera axis, the approximate image brightness, I, can be written as

$$I = \frac{R_f B\ \omega T \cos\theta}{M^2 \frac{Vt + d}{d}} \quad , \quad \text{lumens/cm}^2 \quad . \qquad \text{(F-4)}$$

Then, the exposure of film in time t is

$$\text{Exposure} = \frac{R_f B\ \omega Tt \cos\theta}{M^2 \frac{Vt + d}{d}} \quad , \quad \text{lumen-sec/cm}^2 \quad . \qquad \text{(F-5)}$$

In Eq. (F-5), if the optical system is selected and the speed, size, and reflectivity of the moving particles are known, then the performance of the light source required to produce a minimum image density on a particular film can be determined as a function of magnification. This is illustrated by the following example in which the values are chosen to simulate the conditions which may be obtained in the metal vapor condensation experiments:

$R_f$ = 50%, a typical value for polished copper

V = 3000 ft/sec, 5000 ft/sec

$\theta = 40^o$

$\omega$ = 0.201, corresponding to a NA 0.25 objective

Royal X-Pan film, which under forced developing condition has an ASA rating of 3000.

A minimum image density of 0.6; this is 0.2 above the fog level and 0.1 larger than the minimum recommended by ASA (Ref. F-6).

Using these values, the required intensity of the light source I can be calculated as a function of magnification. The results are shown in Fig. F-2 and give the lower bound of the light source requirement. The maximum output of the commercial flash light source is also shown in the figure. It is seen that the performance of the flash light source is not adequate for photography of small high speed particles; e.g., the photography of one micron diameter high lights (the particles may be 10 times larger) requires a minimum magnification of 25 for image resolution on the film; this allows a maximum particle velocity of about 240 ft/sec.

The photography of micron size particles may be possible with a laser light source. The laser has a very short discharge time and produces an intense light beam. It is interesting to estimate the performance of a laser source with the optical system assumed in the last example. Changing the film to Kodak 103 a-U, which is more sensitive to the laser light (wavelength of 6900 A) than Royal X-Pan, the exposure required to produce an image

density 0.6 above fog level is .058 erg/cm$^2$ (Ref. F-7). With this value, the performance requirements of the laser source can be calculated. The results are shown in Fig. F-3. At present, lasers with an output of 550 kw/cm$^2$ and a 20 nanosecond duration have been built (Ref. F-8). The performance capabilities of this laser light source greatly exceed the flash light source as shown in Fig. F-3. It appears that photography of micron size particles can be accomplished only with a laser light source.

INFLUENCE OF PARTICLE NUMBER DENSITY

During the time exposure, each particle that flows through the field of view of the camera will produce a sharp streak image on the film. Therefore, the number of sharp streaks on the film represents the number of particles that the camera "sees" in the volume determined by the product of the area and the depth of field, if it is assumed that no streaks are superimposed. An estimate of the maximum number density, that the camera can successfully see, is given by the relation

$$\frac{\text{number of streaks on film}}{\text{area of field x depth of field}} = \frac{\dfrac{\text{area of film}}{D(Vt + D)\, M^2}}{\text{area of field x depth of field}} = \frac{1}{D(Vt + D) \text{ x depth of field}} \qquad \text{(F-6)}$$

where V is the velocity of the particles, D is the particle diameter, t is the exposure time, and M is the magnification of camera. The depth of field can be calculated from the formula

$$\text{depth of field} = \frac{\text{diameter of "circle of confusion"}}{\tan(\sin^{-1} \text{NA})} \qquad \text{(F-7)}$$

where the diameter of circle of confusion can be assumed to be the resolution of the objective.

The allowable maximum number density of particles in a flow can be estimated from Eq. (F-6). As an example, the number density of particles moving at 3000 ft/sec and 5000 ft/sec is plotted against the particle size in Fig. F-4. The typical measured number density of condensate in wind tunnels is of the order of $10^8$ particles/$cm^3$ (Ref. F-9). Figure F-4 shows that the photographic system is capable of resolving particles with number densities of this order of magnitude provided that the exposure time is less than 0.1 microseconds and the NA of the objective is larger than 0.25.

REFERENCES


F-1 Sears, F. W., Optics, Addison-Wesley Press, Inc., Cambridge, Mass., 1949.

F-2 Boutry, G. A., and Auerbach, R., Instrumental Optics, Interscience Publishers Inc., New York, 1962.

F-3 Castle, F., Woodbury, W., Shelton, W. A., "Reciprocity-Law Failure at Very Short Exposure Time", Proceedings, Third International Congress on High-Speed Photography, Butterworth Scientific Publications, London, 1957.

F-4 Nolan, P., "High Intensity, Fractional Microsecond Light Source", Proceedings, Fifth International Congress on High-Speed Photography, Society of Motion Picture and Television Engineers, New York, 1962.

F-5 Moden, J. C., "Short-Duration Spark Light Source of Extreme Luminance", Proceedings, Fifth International Congress On High-Speed Photography, Society of Motion Picture and Television Engineers, New York, 1962.

F-6 Pressman, Z., "A Comparison of High-Speed Photographic Films with Different Vigorous Development Conditions", Proceedings, Fifth International Congress on High-Speed Photography, Society of Motion Picture and Television Engineers, New York, 1962.

F-7 Kodak Plates and Films for Science and Industry, Eastman Kodak Company, 1962.

F-8 Ellis, A. T., Cal. Tech., Personal Correspondence, February 7, 1964.

F-9 McLellan, C. H., and Williams, T. W., "Liquefaction of Air in the Langley 11-inch Hypersonic Tunnel", NACA TN 3302, October 1954.

TABLE F-1

CALCULATED OPTICAL PROPERTIES OF OBJECTIVE
(light wave length = 5500 Å)

| Numerical Aperture (NA) | Calculated Resolving Power*, lines/mm | Calculated Depth of Field**, microns |
|---|---|---|
| 0.08 | 238 | 52.4 |
| 0.1 | 304 | 32.6 |
| 0.17 | 505 | 11.5 |
| 0.25 | 746 | 5.1 |

$$^{*}\text{Resolving power} = \frac{\text{NA}}{0.61 \times 5.5 \times 10^{-4}\ \text{cm}}$$

$$^{**}\text{Depth of field} = \frac{\text{Objective resolution}}{\tan(\sin^{-1}\text{NA})}$$

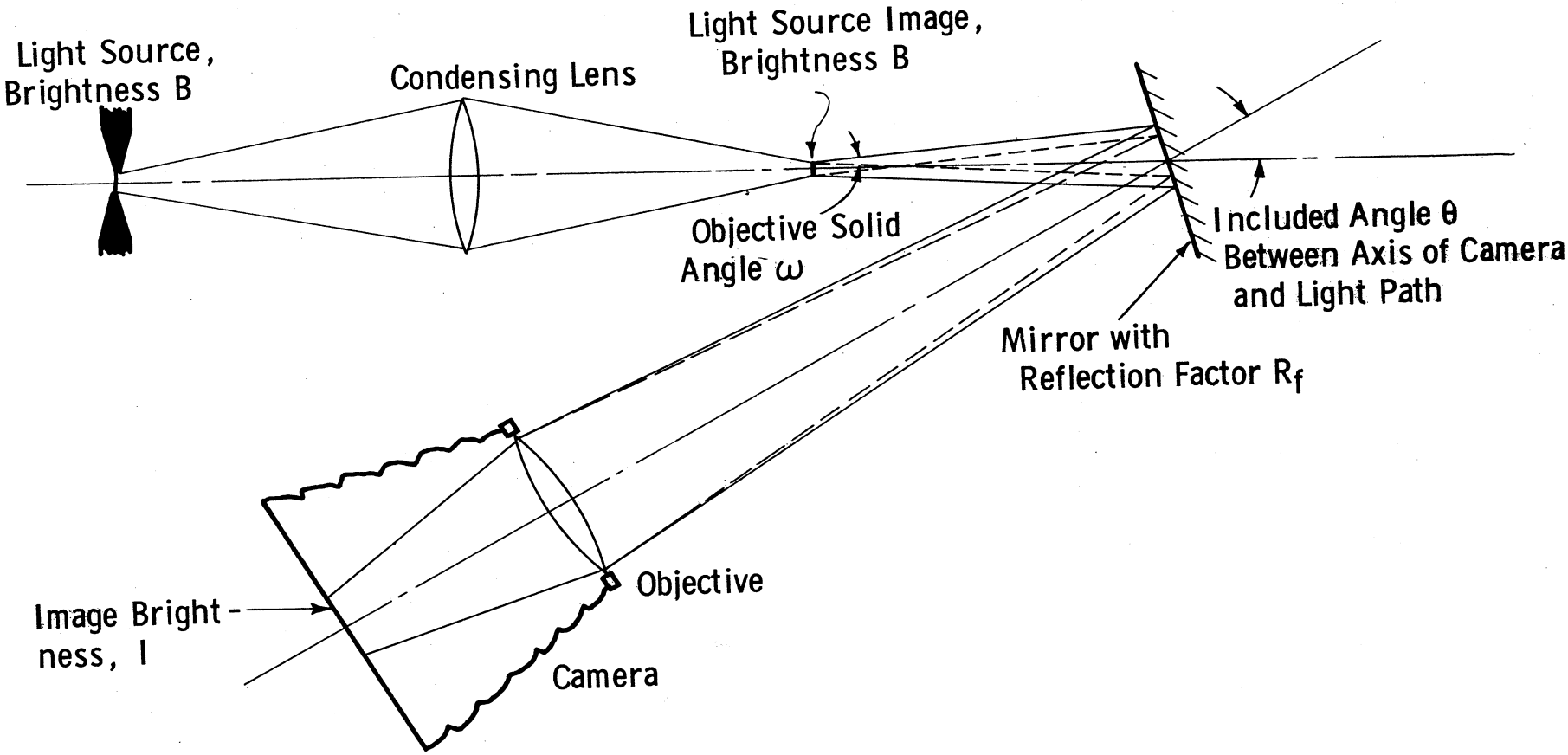


Figure F-1. Geometrical Relationships Used in Computing Image Brightness I

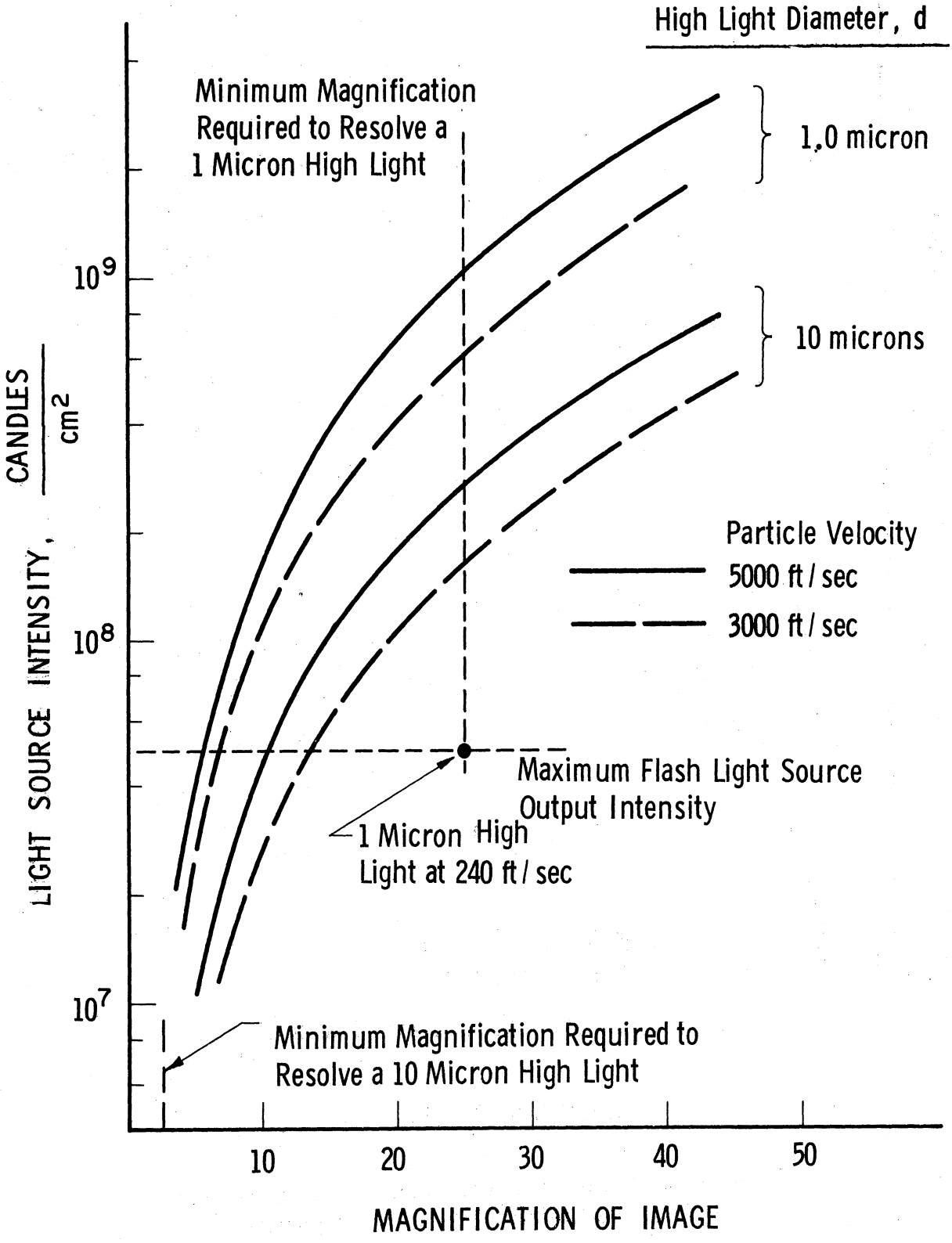


Figure F-2. Conventional Light Source Intensity Requirement for Photographing Small, High-Speed Particles

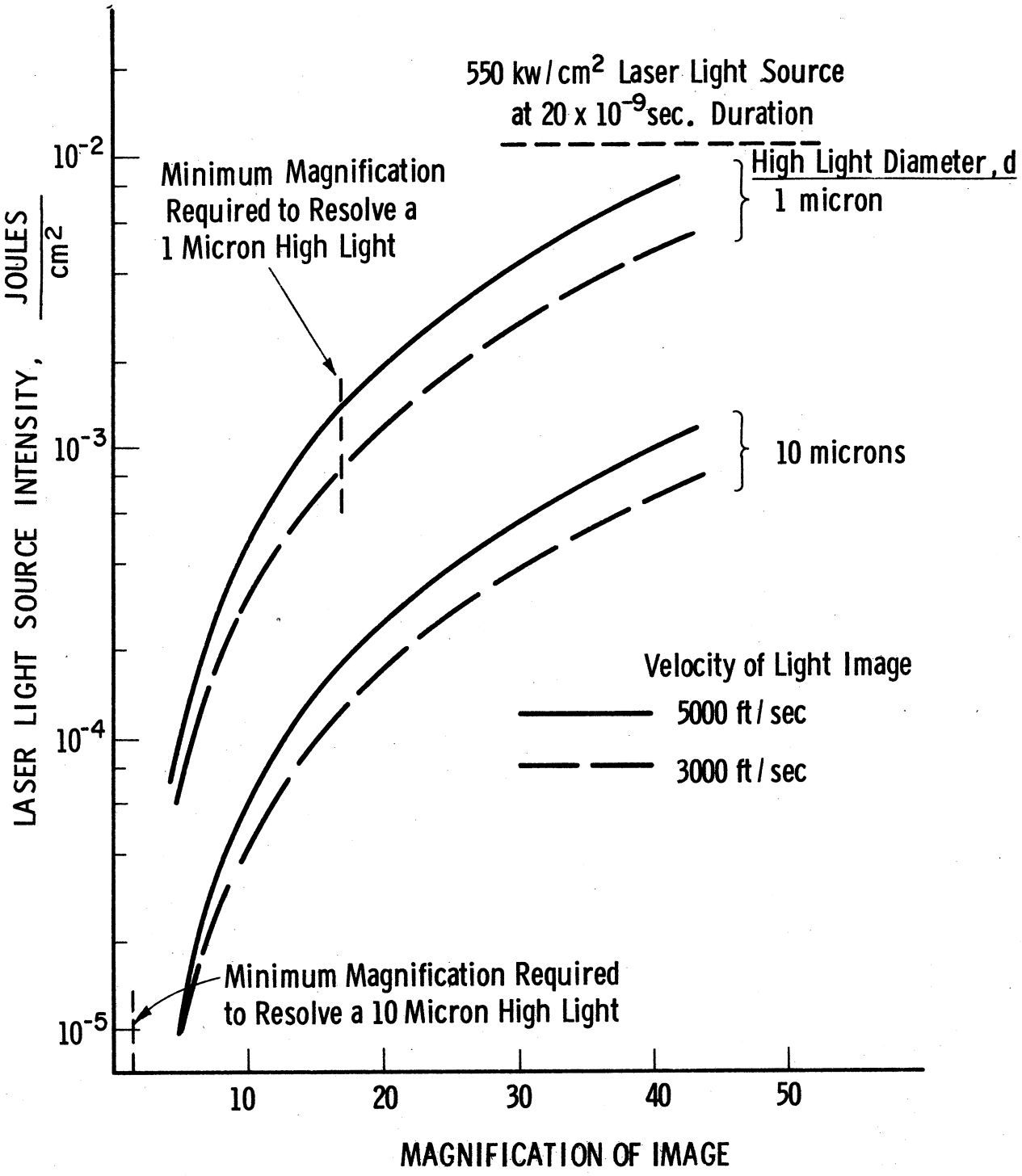


Figure F-3. Laser Light Source Intensity Requirement for Photographing Small, High-Speed Particles

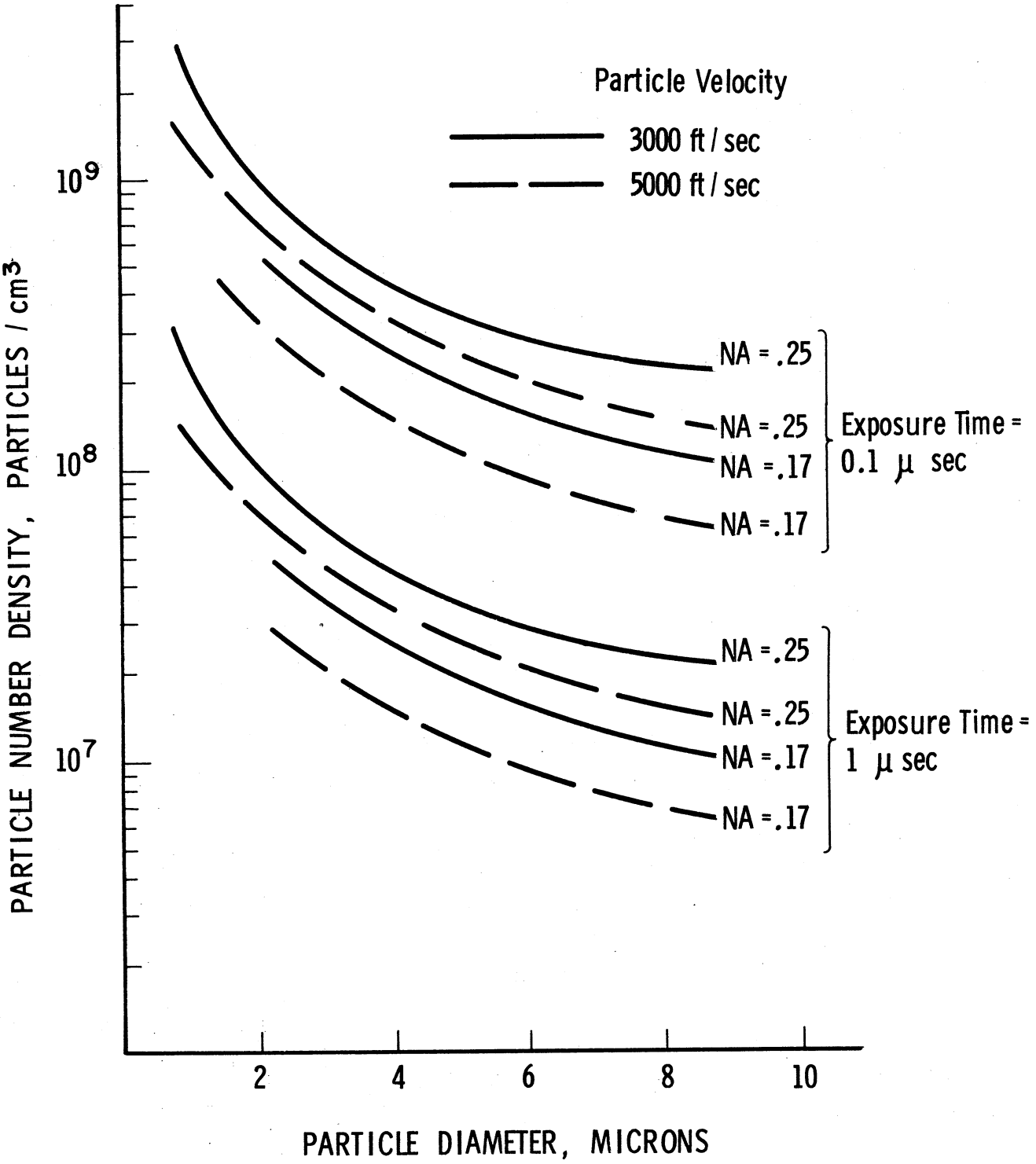


Figure F-4. Calculated Number Density of Particles the Photographic System Can Resolve

## APPENDIX G

## RELATIONSHIP OF PARTICLE SIZE TO PHOTOMICROGRAPHIC IMAGE

P. L. Lu

It is assumed that all the condensed particles are in the form of small spheres and that each of these spheres acts as a small convex mirror. The high light on each spherical particle is the image of the light source and it is this high light that produces images on the film. The diameter, d, of the high light can be calculated by using the regular convex mirror formula (Ref. G-1) in the following form

$$d = \frac{DH}{D + 4L} \tag{G-1}$$

where D is the diameter of the particle and dimensions H and L are shown in Fig. G-1. The width W of the streak image on the film can be related to the high light by the simple expression

$$W = Md \quad , \tag{G-2}$$

where M is the magnification of the camera. By equating the above two expressions, the diameter of the particle can be related to the width of the streak by

$$D = \frac{4LW}{HM - W} \tag{G-3}$$

This expression is derived on the basis of geometrical optics relationships only. Therefore the measured streak image width will not have the true geometric size, but will be larger than it, due to two factors that tend to "spread" the image width. One is the effect of Airy pattern. The other is the turbidity of the emulsion. Therefore, a correction factor is required to modify Eq. (G-3) whenever a particular optical system and film is selected; this factor should be found experimentally.

Reference G-1: Sears, F. W., Optics, Addison-Wesley Press, Inc., Cambridge, Mass., 1949.

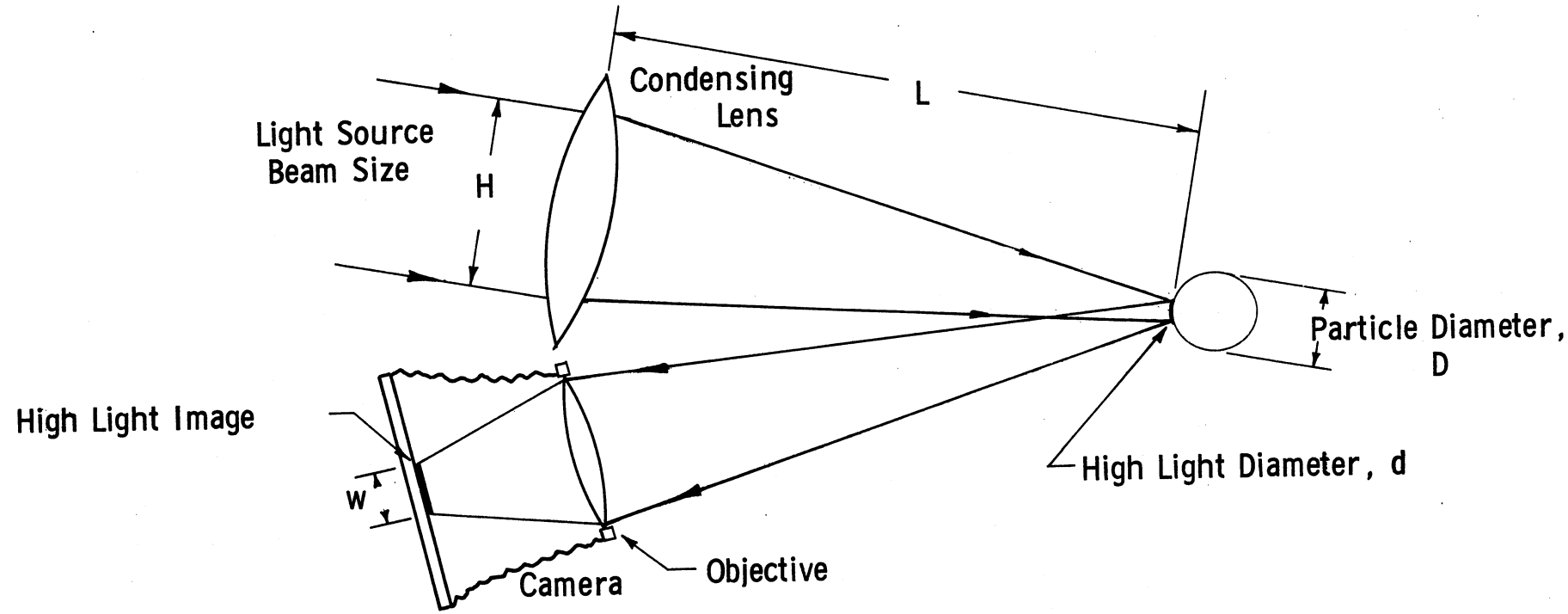


Figure G-1. Geometry of High Light Image Formation

# APPENDIX H

# PERFORMANCE OF A 24-JOULE SPARK LIGHT SOURCE

E. Oktay

## INTRODUCTION

An extremely bright, short time duration light source is required to take photomicrographs of small, high-speed particles. A spark light source with a maximum energy storage capability of 1 joule was available. Preliminary experiments with this light source indicated that the light output was insufficient for the photomicrographic studies. Therefore, a new spark light source, with a maximum energy storage capability of 24 joules, was assembled and experiments were conducted to obtain information about its light pulse duration and light output. Similar experiments were conducted on the 1 joule light source for comparison purposes.

## PRINCIPLE AND CIRCUIT ANALYSIS

A light of extreme brightness and of short time duration can be produced by discharging a capacitor through a spark gap. However, the design of the capacitor and of the discharge circuit is critical to the attainment of the desired brightness and short duration.

The construction and electrical circuitry of the 24-joule spark light source are shown in Fig. H-1. The capacitor $C_o$ is charged to voltage $V_o$, which is less than the breakdown voltage of the gap A-C. When switch S is closed, a 20 kv pulse from the ignition coil initiates a spark between the gap A-B. The ionized media due to this spark breaks down gap A-C, allowing the energy stored in capacitor $C_o$ to discharge into the spark gap.

The equivalent L-R-C circuit for the capacitor, leads, and gap is shown in Fig. H-2. The inductance L is the summation of the inductance of the leads, of the inherent inductance of the capacitor, and of the time varying

inductance of the spark gap. R is the time varying resistance of the spark gap. If L and R are assumed to be time averaged values for the discharge, the differential equation describing the time-wise current variation in a series L-R-C circuit is

$$\frac{d^2i}{dt^2} + 2\alpha\frac{di}{dt} + \omega_o^2 i = 0 \quad , \tag{H-1}$$

where

$$\alpha = \frac{R}{2L}$$

and

$$\omega_o^2 = \frac{1}{LC} \quad .$$

Two types of discharge of the capacitor can be considered:

(a) Underdamped discharge, $\alpha < \omega_o$: from the solution of Eq. (H-1), the form of the current response can be shown to be

$$i(t) = \frac{V_o}{L\omega_d} e^{-\alpha t} \sin \omega_d t \tag{H-2}$$

where

$$\omega_d^2 = \omega_o^2 - \alpha^2$$

(b) Overdamped discharge, $\alpha > \omega_o$: here, solution of Eq. (H-1) is

$$i(t) = -\frac{V_o}{L(p_2 - p_1)}\left(e^{p_1 t} - e^{p_2 t}\right) \tag{H-3}$$

where

$$p_1 = -\alpha\left[1 - \sqrt{1 - \frac{\omega_o^2}{\alpha}}\right]$$

and

$$p_2 = -\alpha\left[1 + \sqrt{1 - \frac{\omega_o^2}{\alpha}}\right]$$

A fast light source requires that i(t) decay to zero rapidly. This requires that the damping coefficient $\alpha$ be as large as possible. From the relation $\alpha = R/2L$, it is seen that L must be small. Hence, in designing a fast capacitor-discharge light source, L due to the construction of the capacitor, leads, and spark gap should be minimized.

## CAPACITOR DISCHARGE CHARACTERISTICS MEASUREMENTS

Three separate measurements were made to study the discharge characteristics of the 24-joule light source. These measurements were of the light pulse duration, the spark gap voltage variations, and the di/dt variations in the discharge circuit. The latter two measurements were made to obtain information on the discharge circuit characteristics to support the light pulse duration measurements. All data were recorded by a Tektronix 551 Dual Beam Oscilloscope. The spark-gap voltage, or the phototube output, was fed through a Type CA preamplifier to one of the oscilloscope beams and the di/dt signal was fed through a Type D high gain differential amplifier to the other beam.

### A. Light Pulse Duration Measurements

The light pulse duration measurements were made with a phototube for which the circuit diagram is shown in Fig. H-3. The load resistor, $R_L$, was kept to a minimum so that the time constant, $\tau = R_L C$, of the measuring circuit would be small compared to the expected duration of the light pulse. C

represents the capacitance of the leads, between the load resistor and the scope, and was approximately 200 $\mu\mu$f. To minimize erroneous signals due to the radiation field generated by the discharge of the capacitor, the phototube was placed about six feet from the light source and shielding was used where possible.

A typical phototube trace is shown in Fig. H-4. This trace represents the light pulse for the capacitor charged to 10 kv. Although the total light duration is about 15 $\mu$sec, the light intensity has dropped to less than one-half its maximum value in about 2 $\mu$sec.

B. Spark Gap Voltage Characteristics

The spark gap voltage characteristics were studied by use of a high impedance resistive voltage divider. The voltage divider was put across the points A and C shown in Fig. H-1, such that a voltage signal of $1.5 \times 10^{-5} \times V_o$ above ground was recorded on the scope. The bottom trace of Fig. H-5 represents the time varying spark gap voltage, and the upper trace of the same figure represents the light pulse, recorded simultaneously. Although a sinusoidal wave form was expected for the spark gap voltage, it appears that the wave form is being distorted by the voltage divider.

C. di/dt Characteristics of the Capacitor Discharge Circuit

Due to the construction of the light source, it was possible to study only the di/dt variations in the discharge circuit rather than the i(t) variations.

The magnetic field B(t) in the vicinity of a conductor is proportional to the current i(t)

$$B(t) = \frac{\mu_o \, i(t) \, \ell}{4\pi} \sim i(t) \quad , \qquad \text{(H-4)}$$

and the voltage e induced on a coil in a magnetic field B(t) is proportional to di/dt

$$e(t) \sim \frac{dB(t)}{dt} \sim \frac{di(t)}{dt} \quad . \tag{H-5}$$

A coil was wrapped around the conductor D-F shown in Fig. H-1. The inductance of this coil was found experimentally to be approximately 0.8 $\mu$hy, and the capacitance due to the leads was approximately 200 $\mu\mu$f; hence, the natural frequency of the equivalent parallel L-R-C circuit of the pickup coil was about $1.3 \times 10^7$ cps. This was higher than the expected frequency of the discharge and therefore, it was established that the output of the pickup coil indicated the di/dt variations in the discharge circuit with no distortions due to the pickup coil itself.

The upper trace of Fig. H-6 represents the output of the pickup coil described above; hence, it is proportional to the di/dt variation in the discharge circuit. The lower trace of the Fig. H-6 shows the light pulse output recorded simultaneously for comparison purposes.

The di/dt variation is sinusoidal as expected, and the zeros of this wave form represent the extremum points of the current in the discharge circuit. Note that these zeros correspond to the peaks of the light pulse trace.

In Fig. H-7, the upper trace represents the di/dt variation, and the lower trace represents the spark-gap voltage variations. These data were recorded to determine the relationship between the spark-gap voltage and the di/dt variation, and it is noted that voltage and di/dt waves are in phase.

From Figures (H-5), (H-6), and (H-7), it is observed that the total time duration of the light pulse is comparable to the time duration of the voltage and current oscillations in the circuit.

D. Inductance and Resistance Calculations for the 24 Joule Light Source

From the data trace of Fig. H-6, the parameters $\omega_d$ and $\alpha$ were measured to be:

$$\omega_d = 1.57 \times 10^6 \text{ sec}^{-1}$$

$$\alpha = 4 \times 10^4 \text{ sec}^{-1}$$

By use of the relations

$$\omega_o^2 = \frac{R}{2L} \quad , \quad \text{and} \quad \omega_d^2 = \omega_o^2 - \alpha^2 \quad ,$$

the values of L and R were calculated to be 3.39 $\mu$hy and 0.271 $\Omega$ respectively. The value of L is high, indicating the cause of the underdamped discharge and the 10-15 microsecond discharge time.

It is interesting to note also that initial current of the discharge, $I = V_o/L\omega_d$, was computed to be 1780 amps for the case where the charging voltage $V_o$ was 10 kv.

## ENERGY OUTPUT AND LIGHT INTENSITY OF THE 24-JOULE LIGHT SOURCE

The light beam used in the photomicrography studies contained, possibly, 1% of the total light output of the source. An attempt was made to use a thermopile to measure the energy contained in this light beam. Fig. H-8 shows the experimental arrangement.

Light energy focused into the cone of the thermopile heated the cone and the resulting change in the temperature of the cone was recorded by a thermocouple-microvoltmeter circuit. The thermopile was calibrated at the factory to have an output of 202 $\mu$volt/joule. The microvoltmeter had a reading sensitivity of 0.1 $\mu$volt enabling energies as low as 4.5 millijoules to be detected. To check the operation of the system, the cone was exposed to a continuous light source. Response of the thermopile to this energy input was detected by the microvoltmeter. However, no instrument response was obtained during the experiments with the 24-joule spark light source, suggesting that the energy of the light beam was less than the threshold of the system, i.e., less than 4.5 millijoules.

The light intensity of the spark column also was measured photographically. A sheet of Polaroid Type 52 film was exposed by placing it three feet from the light source. The density of the resulting negative was measured with a Kodak densitometer and found to be 0.84. The exposure, corresponding to this density is 5.5 lumen-sec/meter$^2$ as determined from the film's characteristic curve published by the Polaroid Company. Knowing the effective spark duration to be about 5 microseconds, the mean intensity of the light source was computed using the point source illumination formula and found to be about $8 \times 10^6$ candles/cm$^2$.

## ONE-JOULE SPARK LIGHT SOURCE

Using the measuring techniques described previously, experiments were conducted to study the light pulse duration, the spark-gap voltage, and the di/dt variation characteristics of the one-joule light source. Also, some limited experiments were conducted to study the effect of capacitor charging voltage $V_o$ on the light pulse duration.

Figure H-9 shows the one-joule spark light source which has a total capacitance of 5000 $\mu\mu$f. Figures H-10 through H-12 show the light pulse, the di/dt variation, and the spark gap voltage characteristics for this light source where charging voltage $V_o$ was 15 kv. Due to the compactness of the source, the inherent inductance of the system was very small, resulting in an overdamped discharge. The measured time duration of the light pulse was less than 0.5 $\mu$sec.

Figures H-13a through H-13d show the variations of the light pulse as the capacitor charging voltage was varied from 10 kv to 20 kv. All other parameters were held constant. It can be seen from these records that the light pulse duration was increased as the voltage $V_o$ was increased. Also since the area under the light pulse curve is proportional to the energy in the light beam at wavelengths corresponding to the spectral sensitivity of the photocathode of the phototube, these records show an increasing energy output with stored energy.

## CONCLUSIONS

The experiments on the 24 joule spark light source indicated that the inherent inductance of the system was high and, therefore, that the discharge of the capacitor bank was underdamped. The usable light pulse duration was found to be about 5 $\mu$sec while the light intensity dropped below 50% of its maximum intensity in about 2 $\mu$sec. The energy contained in the light beam from the spark was found to be less than 4.5 milijoules and the intensity of the spark was measured at about $8 \times 10^6$ candle-sec/meter$^2$.

The one-joule light source was more compact and, therefore, the discharge characteristic of this system was overdamped. The light pulse duration was less than 0.5 $\mu$sec and decreased with decreases in stored energy.

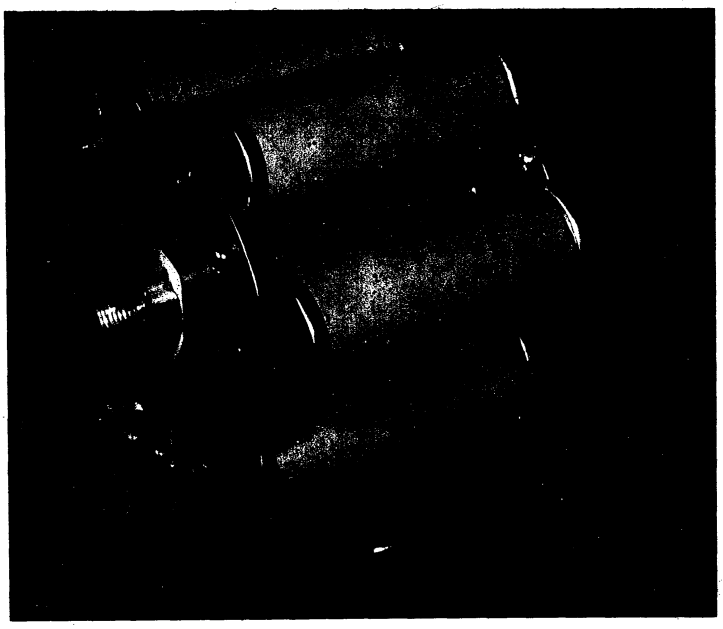

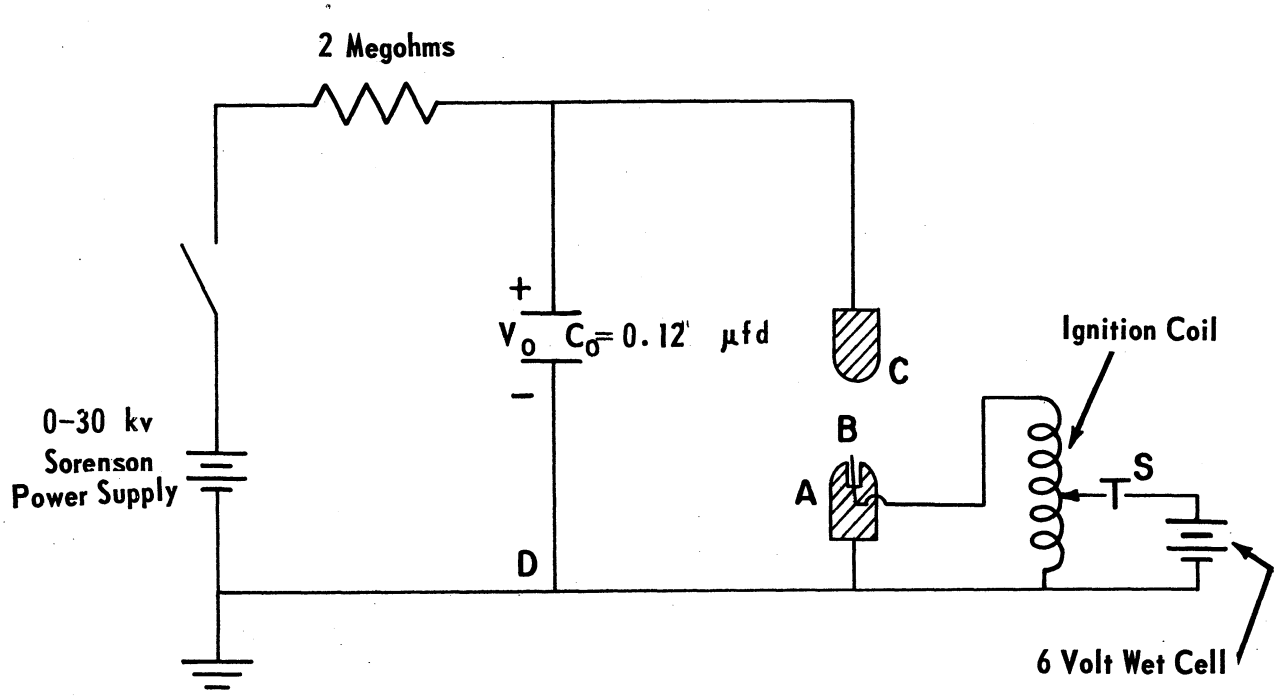


Figure H-1. 24-Joule Spark Light Source

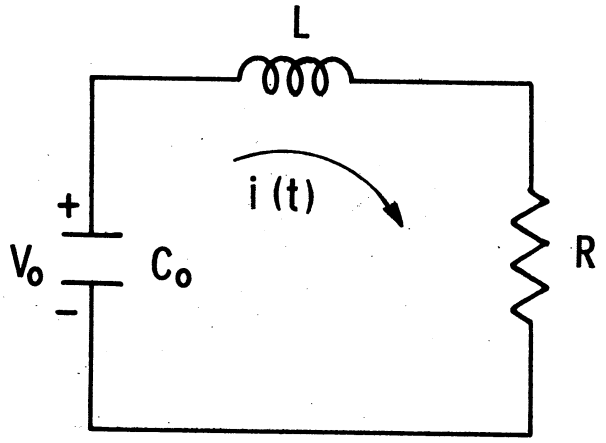


Figure H-2. Equivalent L-R-C Circuit for the Discharge of a Capacitor Through a Spark Gap

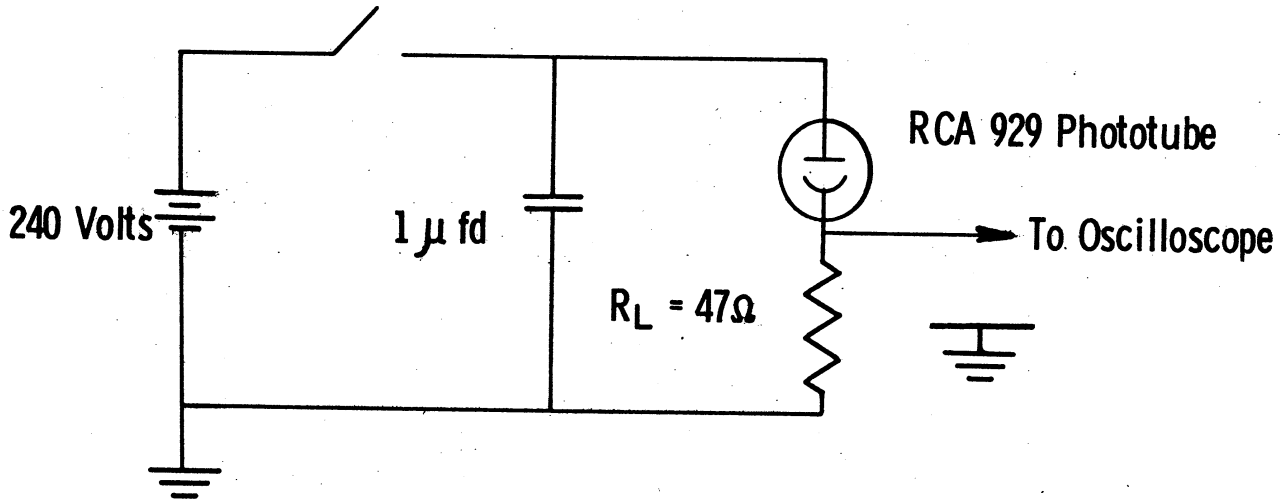


Figure H-3. Phototube Circuit

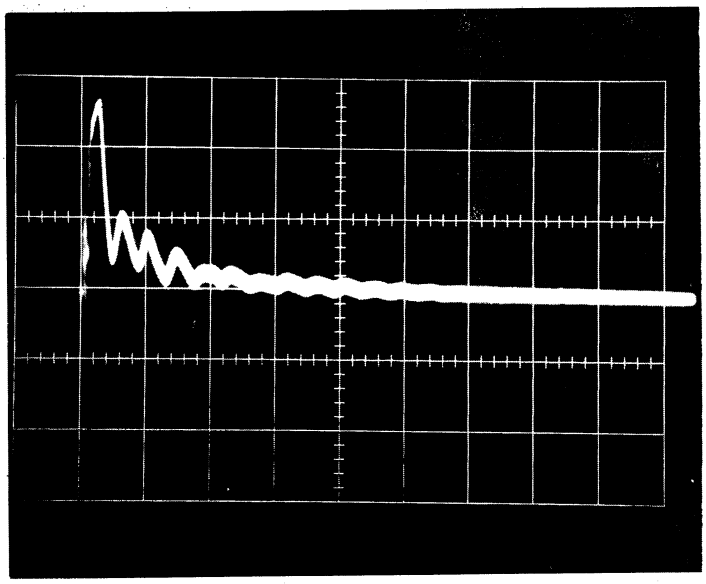

Horizontal Sweep Time = 5 μsec / cm

Figure H-4. Phototube Trace of Light Pulse from the 24-Joule Spark Source

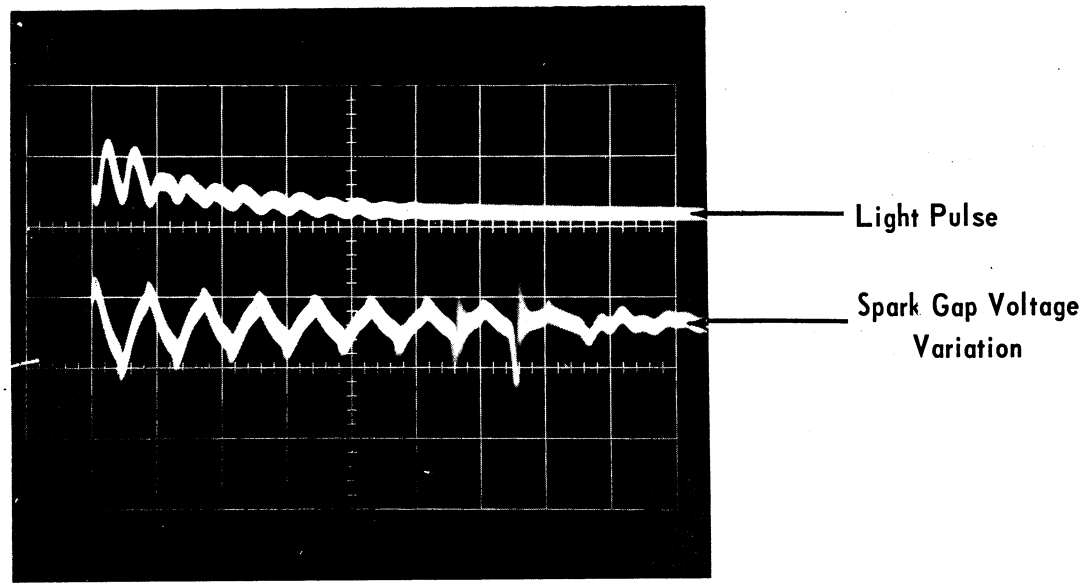


Horizontal Sweep Time = 5 μsec/cm

Figure H-5. Light Pulse and Spark Gap Voltage for the 24-Joule Spark Source

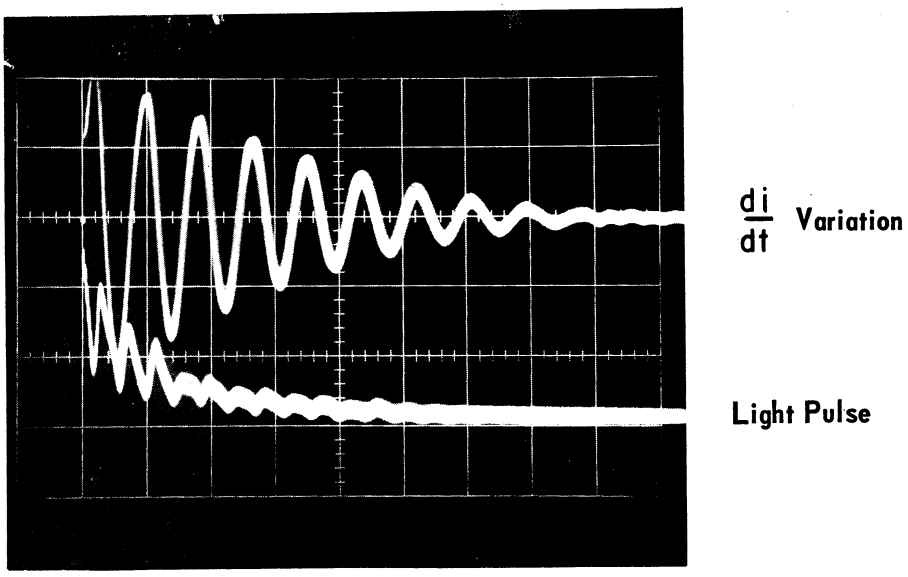


Figure H-6. di/dt Variation and Light Pulse for the 24-Joule Spark Source

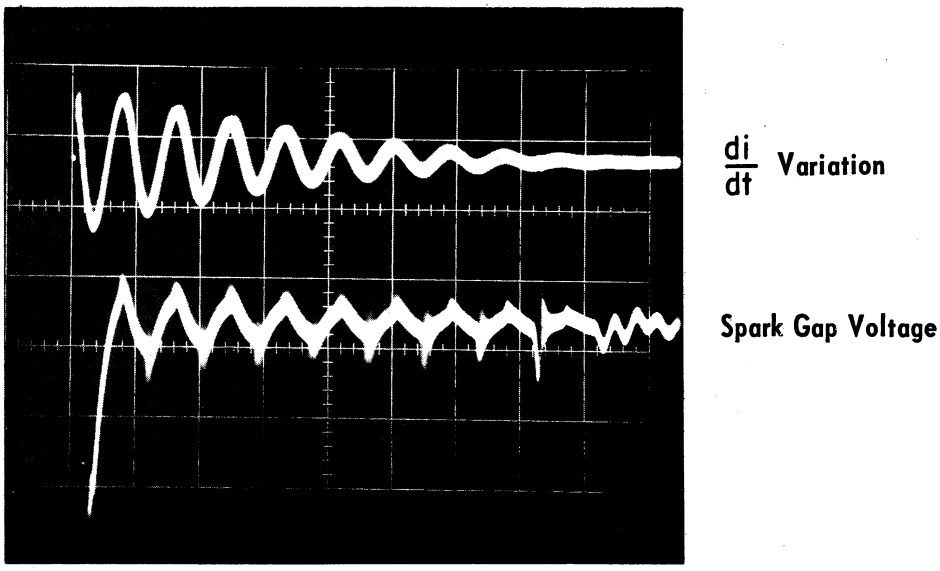


Figure H-7. di/dt Variation and Spark Gap Voltage for the 24-Joule Spark Source

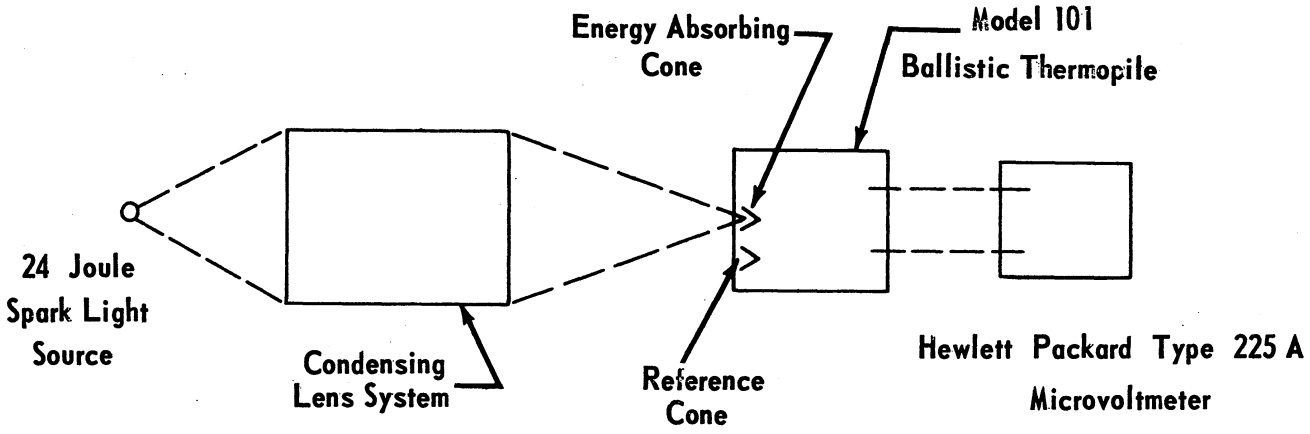


Figure H-8. Experimental Arrangement for Measuring Light Beam Energy

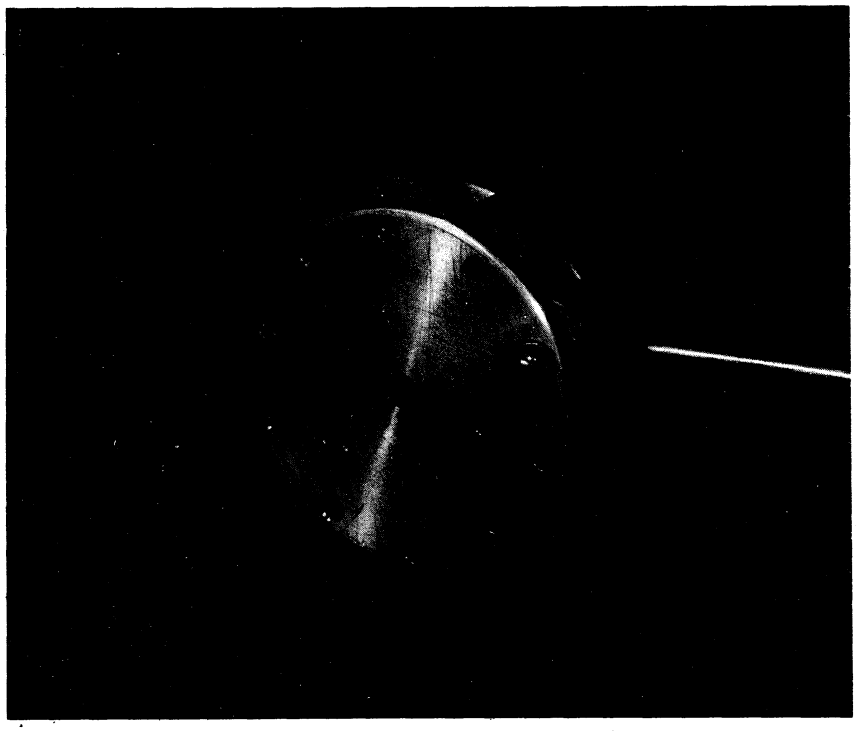

Figure H-9. One-Joule Spark Light Source

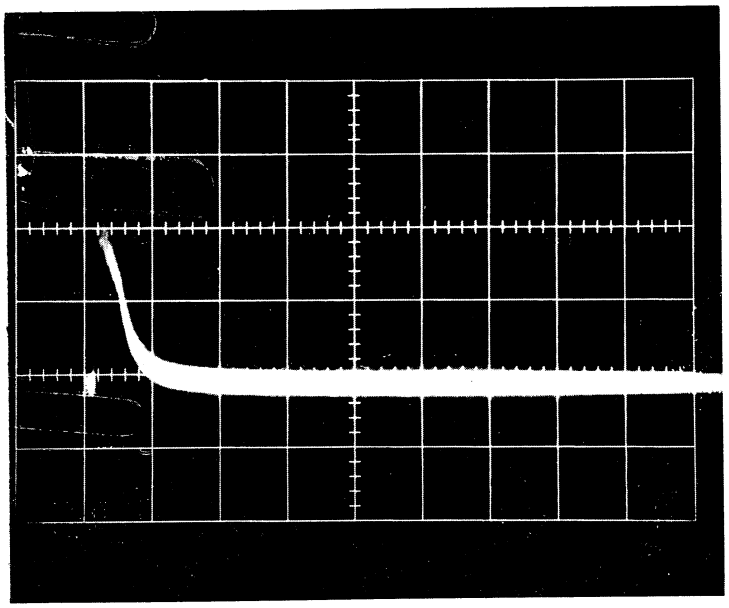

Horizontal Sweep Time = 1 μsec / cm

Figure H-10. Light Pulse from the One-Joule Spark Source

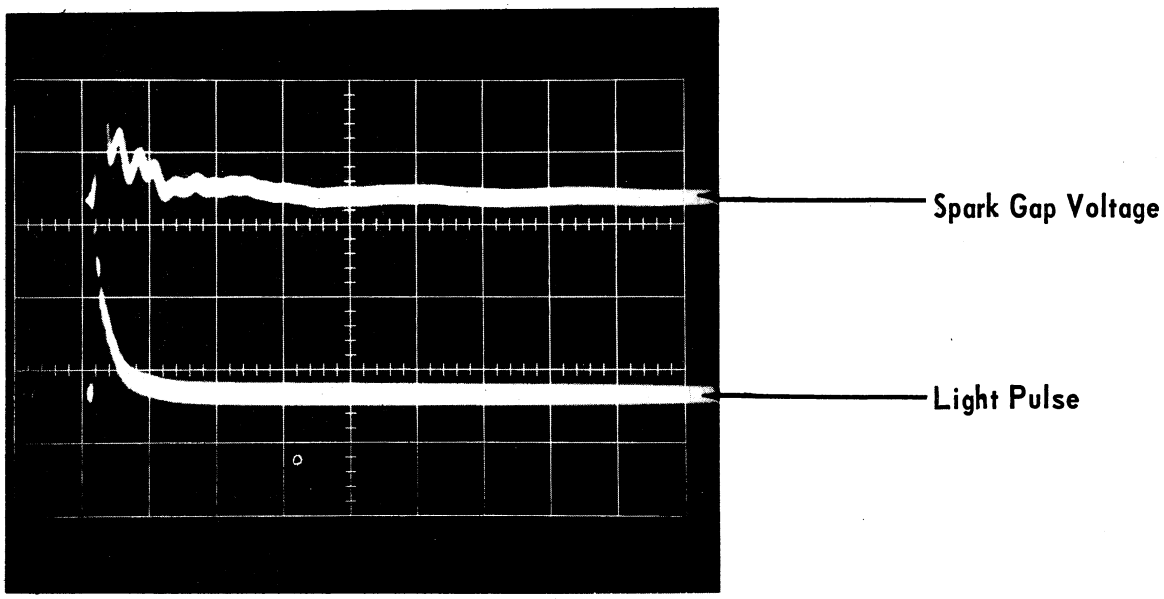


Figure H-11. Spark Gap Voltage and Light Pulse Record for the One-Joule Spark Source

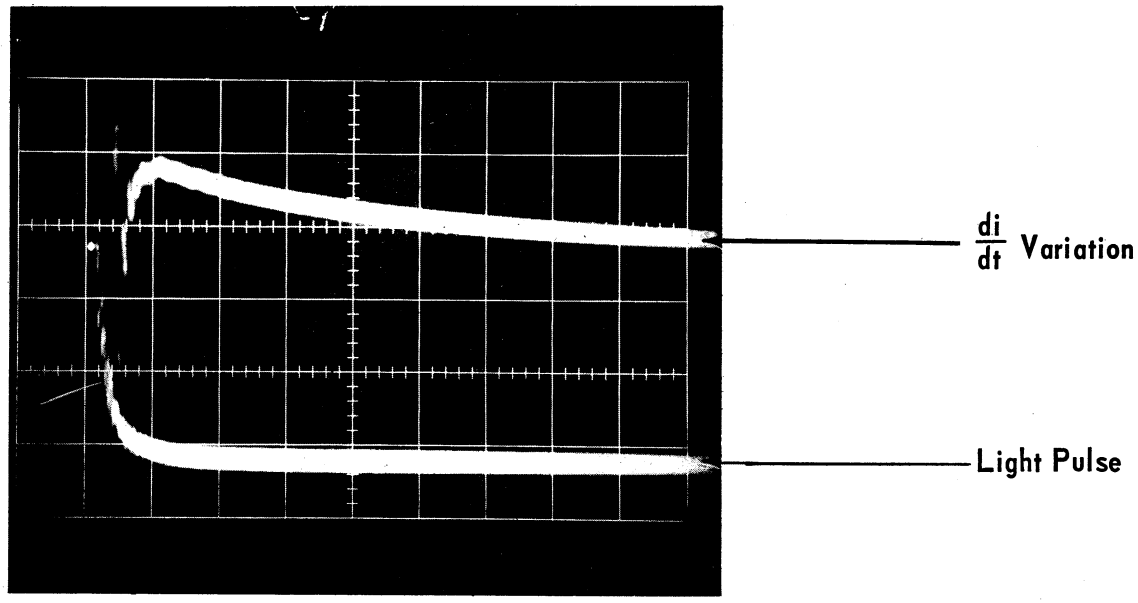


Figure H-12. di/dt Variation and Light Pulse Record for the One-Joule Spark Source

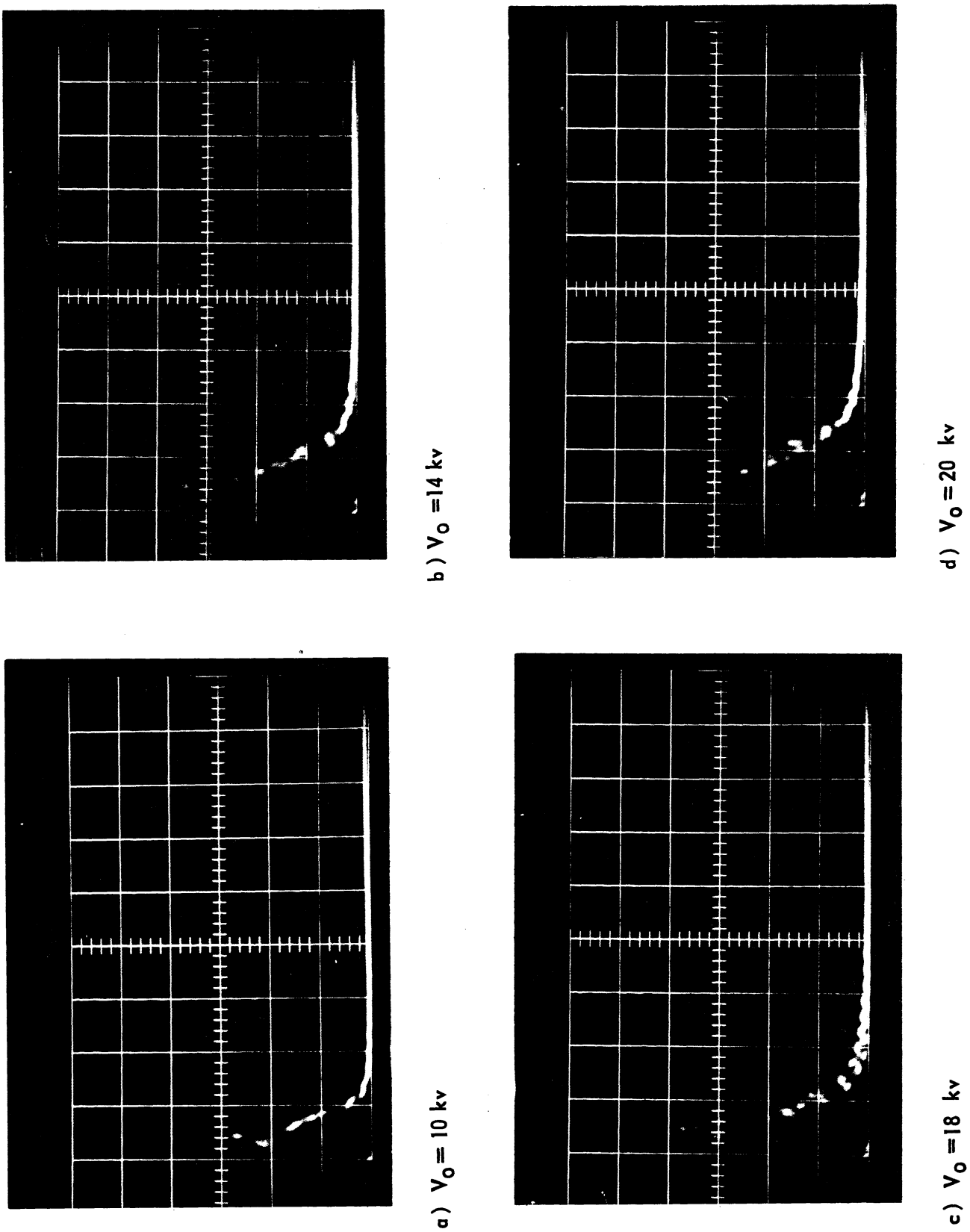


Figure H-13. Light Pulse Records for the One-Joule Spark Source for Capacitor Charging Voltages from 10 to 20 KV

Unclassified
Security Classification

**DOCUMENT CONTROL DATA - R&D**

*(Security classification of title, body of abstract and indexing annotation must be entered when the overall report is classified)*

1. ORIGINATING ACTIVITY *(Corporate author)*
Aerospace Research Laboratories
Thermomechanics Research Laboratory

2a. REPORT SECURITY CLASSIFICATION
Unclassified

2b. GROUP

3. REPORT TITLE
Initial Studies of Condensing Metal Vapors Carried by Expanding Inert Gases

4. DESCRIPTIVE NOTES *(Type of report and inclusive dates)*
TDR Final - closed out 1o March 1965

5. AUTHOR(S) *(Last name, first name, initial)*
K.R. Sivier, Pai-Lein Lu, D.D. McBride and E. Oktay

| 6. REPORT DATE | 7a. TOTAL NO. OF PAGES | 7b. NO. OF REFS |
|---|---|---|
| March 1965 | 131 | 23 |

| 8a. CONTRACT OR GRANT NO. | 9a. ORIGINATOR'S REPORT NUMBER(S) |
|---|---|
| AF 33(657)8867 | ARL 65-59 |
| b. PROJECT NO. 7116 | |
| c. Task No. 7116-01 | 9b. OTHER REPORT NO(S) *(Any other numbers that may be assigned this report)* |
| d. | |

10. AVAILABILITY/LIMITATION NOTICES
Qualified requesters may obtain copies from DDC.
Report is releasable to OTS.

| 11. SUPPLEMENTARY NOTES | 12. SPONSORING MILITARY ACTIVITY |
|---|---|
| | USAF |

13. ABSTRACT A report is presented on the progress of an experimental investigation of the condensation of metal vapors carried by an expanding inert gas initially at high pressure. This investigation has emphasized some initial experiments in the University of Michigan's Hotshot Wind Tunnel and a study of instrumentation techniques.

Three zinc-in-helium tests in the Hotshot tunnel have indicated that the metallic condensate occurs in the form of very small particles; most particles were found to have diameters of from 0.01 to 0.1 microns. These particles were collected on impact probes from the hypersonic nozzle flow and analysed by electronmicroscopy. A spectrographic analysis of the particle samples showed that roughly one percent by mass of contaminants (principally copper, iron and silicon) were added to the zinc in the hotshot arc chamber.

In addition to direct particle sampling, the techniques of light scattering and photomicrography (direct photography of the condensed particles) have been investigated. The study of light scattering has progressed to a bench set-up evaluation and calibration of a system that measures light attenuation by the scattering medium. Although indicating the possibility of the photography of one micron diameter particles traveling at high speed, the study of the photomicrography technique has been discontinued in view of the very small particle sizes indicated by the direct samples from the zinc-in-helium tests.

DD FORM 1 JAN 64 1473

Unclassified
Security Classification

| 14. KEY WORDS | LINK A | | LINK B | | LINK C | |
|---|---|---|---|---|---|---|
| | ROLE | WT | ROLE | WT | ROLE | WT |
| | | | | | | |

## INSTRUCTIONS

1. ORIGINATING ACTIVITY: Enter the name and address of the contractor, subcontractor, grantee, Department of Defense activity or other organization *(corporate author)* issuing the report.

2a. REPORT SECURITY CLASSIFICATION: Enter the overall security classification of the report. Indicate whether "Restricted Data" is included. Marking is to be in accordance with appropriate security regulations.

2b. GROUP: Automatic downgrading is specified in DoD Directive 5200.10 and Armed Forces Industrial Manual. Enter the group number. Also, when applicable, show that optional markings have been used for Group 3 and Group 4 as authorized.

3. REPORT TITLE: Enter the complete report title in all capital letters. Titles in all cases should be unclassified. If a meaningful title cannot be selected without classification, show title classification in all capitals in parenthesis immediately following the title.

4. DESCRIPTIVE NOTES: If appropriate, enter the type of report, e.g., interim, progress, summary, annual, or final. Give the inclusive dates when a specific reporting period is covered.

5. AUTHOR(S): Enter the name(s) of author(s) as shown on or in the report. Enter last name, first name, middle initial. If military, show rank and branch of service. The name of the principal author is an absolute minimum requirement.

6. REPORT DATE: Enter the date of the report as day, month, year; or month, year. If more than one date appears on the report, use date of publication.

7a. TOTAL NUMBER OF PAGES: The total page count should follow normal pagination procedures, i.e., enter the number of pages containing information.

7b. NUMBER OF REFERENCES: Enter the total number of references cited in the report.

8a. CONTRACT OR GRANT NUMBER: If appropriate, enter the applicable number of the contract or grant under which the report was written.

8b, 8c, & 8d. PROJECT NUMBER: Enter the appropriate military department identification, such as project number, subproject number, system numbers, task number, etc.

9a. ORIGINATOR'S REPORT NUMBER(S): Enter the official report number by which the document will be identified and controlled by the originating activity. This number must be unique to this report.

9b. OTHER REPORT NUMBER(S): If the report has been assigned any other report numbers *(either by the originator or by the sponsor)*, also enter this number(s).

10. AVAILABILITY/LIMITATION NOTICES: Enter any limitations on further dissemination of the report, other than those imposed by security classification, using standard statements such as:

(1) "Qualified requesters may obtain copies of this report from DDC."

(2) "Foreign announcement and dissemination of this report by DDC is not authorized."

(3) "U. S. Government agencies may obtain copies of this report directly from DDC. Other qualified DDC users shall request through _____."

(4) "U. S. military agencies may obtain copies of this report directly from DDC. Other qualified users shall request through _____."

(5) "All distribution of this report is controlled. Qualified DDC users shall request through _____."

If the report has been furnished to the Office of Technical Services, Department of Commerce, for sale to the public, indicate this fact and enter the price, if known.

11. SUPPLEMENTARY NOTES: Use for additional explanatory notes.

12. SPONSORING MILITARY ACTIVITY: Enter the name of the departmental project office or laboratory sponsoring *(paying for)* the research and development. Include address.

13. ABSTRACT: Enter an abstract giving a brief and factual summary of the document indicative of the report, even though it may also appear elsewhere in the body of the technical report. If additional space is required, a continuation sheet shall be attached.

It is highly desirable that the abstract of classified reports be unclassified. Each paragraph of the abstract shall end with an indication of the military security classification of the information in the paragraph, represented as *(TS), (S), (C), or (U)*

There is no limitation on the length of the abstract. However, the suggested length is from 150 to 225 words.

14. KEY WORDS: Key words are technically meaningful terms or short phrases that characterize a report and may be used as index entries for cataloging the report. Key words must be selected so that no security classification is required. Identifiers, such as equipment model designation, trade name, military project code name, geographic location, may be used as key words but will be followed by an indication of technical context. The assignment of links, rules, and weights is optional.